University of Southampton

Faculty of Environmental and Life Sciences

Ocean and Earth Science

National Oceanography Centre

Novel applications of GNSS-R data from TechDemoSat-1 to monitoring the cryosphere

Author:

Jessica Cartwright

Supervisors:

Meric Srokosz,

Christopher J. Banks,

& Ivan Haigh

Thesis for the degree of Doctor of Philosophy

17th June 2021

To;

Bobs,

Pippin, Chow,

Baxter, Fresco, Bumble,

and all the other beasts I met along the way.

Abstract

UNIVERSITY OF SOUTHAMPTON

FACULTY OF ENVIRONMENTAL AND LIFE SCIENCES

National Oceanography Centre

Doctor of Philosophy

Novel applications of GNSS-R data from TechDemoSat-1 to monitoring the cryosphere

by Jessica Cartwright

As conditions in the cryosphere are expected to change rapidly, it is important to understand the characteristics of these dynamic regions if we are to fully account for their current and future role in the physical systems of the planet. The monitoring of the cryosphere through satellite remote sensing ensures maximum coverage and reliability of measurements otherwise affected by temporal and spatial sampling biases.

Here I exploit signals of opportunity in the form of Global Navigation Satellite Systems-Reflectometry (GNSS-R) for this purpose. These signals allow low-cost observation of global systems, using only a receiver and existing navigation satellites in orbit. Data from the SGR-ReSI onboard TechDemoSat-1 (TDS-1) are exploited through the satellite's initial (November 2014 - July 2017) and extended (August 2017 - December 2018) missions. I use the Level 1B data to measure both sea ice and glacial ice in order to assess the potential of these signals for understanding these regions.

I produce Digital Elevation Models over the Antarctic and Greenland Ice Sheets. These results demonstrate that when compared with existing products, application of GNSS-R to glacial ice altimetry is possible, acquiring comparable measurements (within 40 cm median difference) to dedicated satellites (eg. CryoSat-2), despite having many fewer measurements, a shorter temporal span and fewer corrections applied. As a multi-static configuration, GNSS-R is in the unique position to be able to obtain measurements at the geographic South Pole itself where traditional altimeters cannot.

Use of GNSS-R for the detection of sea ice in both the Northern and Southern Hemispheres demonstrates the potential for future monitoring of sea ice extent using GNSS-R and shows the benefit of the small footprint of such measurements. Seasonal patterns are visible over the extent of the time series, and high agreement is found with four external products.

Overall, this thesis finds that GNSS-R holds great potential for use over the cryosphere, with the ability to increase spatial resolution of measurements over sea ice and provide data where current altimeters cannot. The use of a multi-platform system for GNSS-R in a constellation configuration would allow increased temporal resolution of measurements and frequency of sampling, and through this higher accuracies.

Acknowledgements

This doctoral project was funded in full by the Natural Environment Research Council through the SPITFIRE Doctoral Training Partnership. I am very grateful for the funding that has allowed me to complete this thesis.

There have also been lots of humans who have brought me to the stage I am now at, not least my wonderful supervisors past and present. Maria Paola Clarizia and Paolo Cipollini set me up to hit the ground running and were so generous with their time and knowledge. More big thanks to Meric Srokosz for taking the baton from them and continuing the kindness and seeing it through to the end. And of course to Chris Banks, the longest-standing supervisor who has put up with a lot of my nonsense and my seeming determination to use 'data' as singular.

I am so grateful for all the wonderful people I met at the National Oceanography Centre, from my first office-mates; Matt, Helen, Zoe and Sam who have had to witness this whole rollercoaster; to the later arrivals of Emma, Oana and Matt (the second).

I was so lucky to be able to do two placements both in research at ACE CRC in Hobart and in industry with Spire Global. Those do not feature in this thesis, but nevertheless shaped my doctoral experience. Biggest thanks here go to Alexander Fraser and Sue Cook for making me feel so welcome so very far from home, and Mick Snelders for fuelling my coding fingers with endless sourdough and croissants.

Finally; a super-big thank you to my family and friends outside of the NOC, for bearing with me while I drove myself to the outer reaches of sense and reason. I am hoping to make my way back as soon as I can - stick the kettle on, I'm coming for you.

And of course, where would an acknowledgements section be without a great big thank you to the TechDemoSat-1 team at SSTL who made this all possible. *[Data available at merrbys.co.uk]*

Academic Thesis: Declaration Of Authorship

I, Jessica Cartwright, declare that this thesis and the work presented in it are my own and has been generated by me as the result of my own original research.

I confirm that:

1. This work was done wholly or mainly while in candidature for a research degree at this University;

.

2. Where any part of this thesis has previously been submitted for a degree or any other qualification at this University or any other institution, this has been clearly stated;

3. Where I have consulted the published work of others, this is always clearly attributed;

4. Where I have quoted from the work of others, the source is always given. With the exception of such quotations, this thesis is entirely my own work;

5. I have acknowledged all main sources of help;

6. Where the thesis is based on work done by myself jointly with others, I have made clear exactly what was done by others and what I have contributed myself;

7. Parts of this work have been published as:

   (a) Cartwright, J., M. P. Clarizia, P. Cipollini, C. Banks, and M. Srokosz, Independent DEM of Antarctica using GNSS-R data from TechDemoSat-1, *Geophysical Research Letters*, *45*(12), 6117–6123, doi: 10.1029/2018gl077429, 2018

   (b) Cartwright, J., C. J. Banks, and M. Srokosz, Sea Ice Detection Using GNSS-R Data From TechDemoSat-1, *Journal of Geophysical Research: Oceans*, *124*(8), 5801–5810, doi: 10.1029/2019jc015327, 2019

   (c) Cartwright, J., C. J. Banks, and M. Srokosz, Improved GNSS-R bi-static altimetry and independent digital elevation models of Greenland and Antarctica from TechDemoSat-1, *The Cryosphere*, *14*(6), 1909–1917, doi: 10.5194/tc-14-1909-2020, 2020

Signed:_____

Date:_____

Contents

List of Figures

List of Tables

Chapter 1

Introduction

1.1 The Cryosphere and Climate

The cryosphere is a dynamic part of the Earth system and the source of many feedback effects between the ocean and atmosphere. With the climate system of the planet changing rapidly (*Pörtner et al.*, 2019), it is of vital importance to understand the role of the cryosphere by monitoring the changes thereof. The term "cryosphere" covers all frozen aspects of the planet, from permafrost tundra to sea ice and glaciers. In this thesis I focus solely on the polar ice component of the cryosphere - glacial ice (Chapters 3 and 4) and sea ice (Chapter 5).

Changes in the volume of water held in sea ice and glacial ice affects the distribution of energy and density of the oceans (*Comiso et al.*, 2003) through the removal and addition of water and/or energy in the form of heat. The net increase in fresh water through the melting of glacial or sea ice, lack of sea ice formation or a combination of the two reduces density of ocean water masses and impacts ocean circulation. This can be seen in the recent weakening of the Atlantic Merdional Overturning Circulation (*Smeed et al.*, 2018), in agreement with climate models forced with anthropogenic warming (*Pörtner et al.*, 2019). It must be noted that this too is a feedback, with basal melting due to increased ocean temperatures a large influence in loss of mass from the great ice sheets (*Adusumilli et al.*, 2018; *Dow et al.*, 2018; *Khazendar et al.*, 2016; *O'Leary and Christoffersen*, 2013).

Sea ice can act as a blanket reducing the exchange of heat and gases between

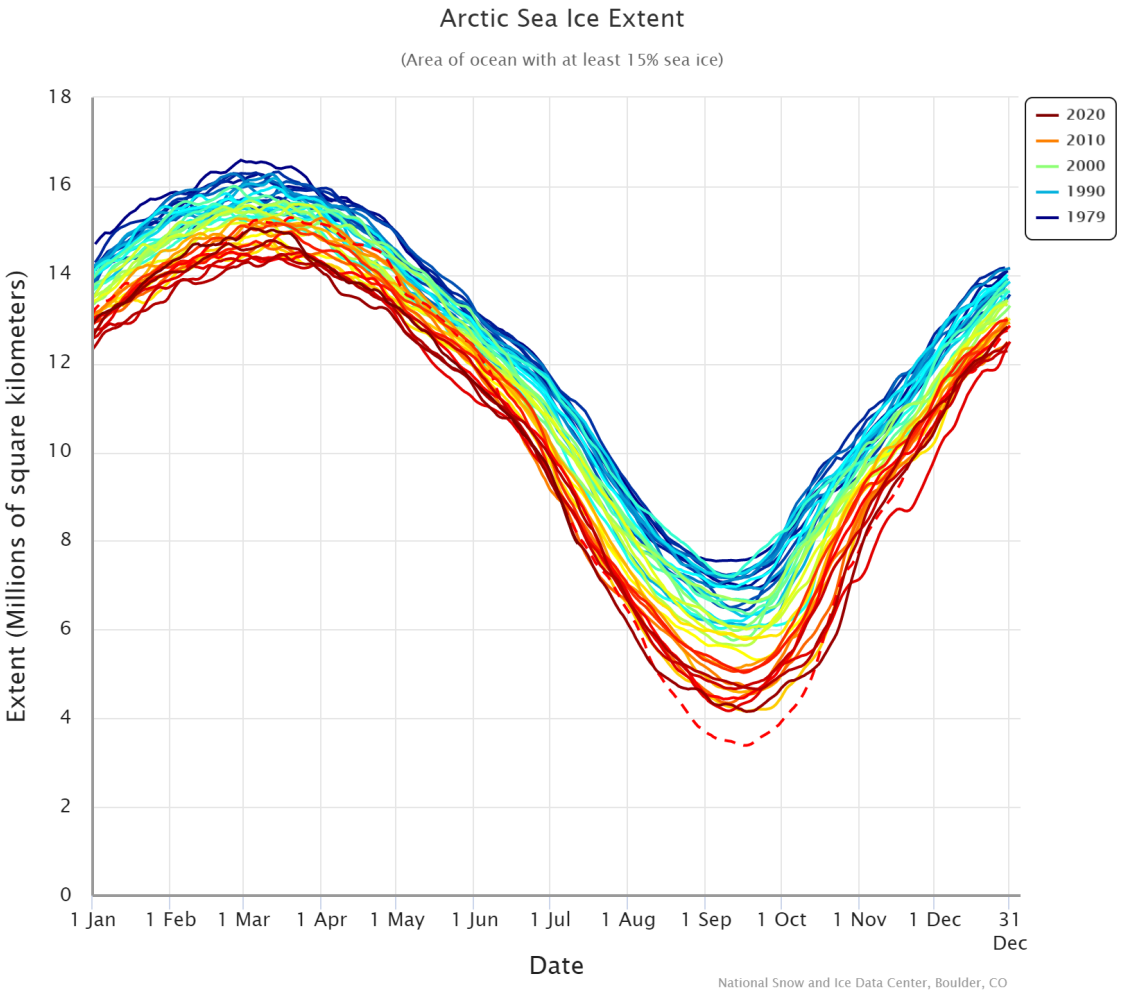

Figure 1.1: Annual sea ice extent in the Arctic from 1979 to July 2020. Lines represent individual years in different colours with red representing the most recent and dark blue the oldest data. Colour scale goes from dark blue (1979) through light blue (1990), green (2000) and orange (2010) to darkest red (2020, present). Dashed red line represents record minimum sea ice extent year 2012. Data from the National Snow and Ice Data Centre, Boulder, Colorado, accessed 13th July 2020.

the atmosphere and the ocean. This has a large impact on the polar air masses, and through this the atmospheric circulation of the Atlantic and Pacific (*Lee et al.*, 2015; *Sgubin et al.*, 2017). Ice cover also affects the solar budget, with open water absorbing ten times the solar radiation of a sea ice covered region the same size (*Stroeve et al.*, 2011). This reflection of solar energy leads to a feedback loop whereby a reduction in the coverage of ice leads to a lower albedo thus more heat absorbed, further reducing ice coverage. The drastic changes seen in the extent of sea ice cover in all seasons over the last few years (Figure 1.1) shows the extent to which this is changing at present and the importance for monitoring it into the

future.

Direct effects of ice on humans can also be seen, and this can often increase the financial viability of the monitoring of the ice itself. The Intergovernmental Panel on Climate Change (IPCC) Special Report on the Ocean and Cryosphere in a Changing Climate (*Pörtner et al.*, 2019) states that 11% of global population inhabits low-lying islands and coastal areas and that the dominant cause of global mean sea level rise is the melting of glaciers and ice sheets. While sea ice does not directly contribute to sea level change, it has significant human impacts, for example through the accessibility of vast oil deposits (*Bird et al.*, 2008), shipping routes (eg. North-West Passage) and changes for Arctic communities.

The scale and remote nature of the polar cryosphere mean that satellite remote sensing is the best tool for their synoptic monitoring and characterisation. The honing of these remote sensing techniques to obtain improved data quality is of the utmost importance if we are to develop a comprehensive understanding of these areas and monitor them effectively.

1.2 Glacial Ice

Glacial ice forms through the compression of snow from repeated precipitation and accumulation in the relief of land (*Lenaerts et al.*, 2019). Where accumulation exceeds ablation, this forms a glacier, which flows under its own weight. This flow deforms the bed over which it travels in addition to the ice itself (*Marshak and Repcheck*, 2016).

Loss of ice from glaciers generally occurs as calving or melting (*Meier*, 1973), with the water travelling under gravity through various parts of the glacial hydrological cycle into oceans or lakes. Where surface mass balance is negative due to these processes, the glacier shrinks, whilst the expansion of the glacier to cover the entire land mass (as seen in Antarctica and Greenland) forms an ice sheet. Such large masses of glacial ice are formed of multiple drainage basins. These are characterised by differing flow speeds and therefore differing degrees of deformation and thermal regimes at the base. Flow speed is highly complex, affected by friction at

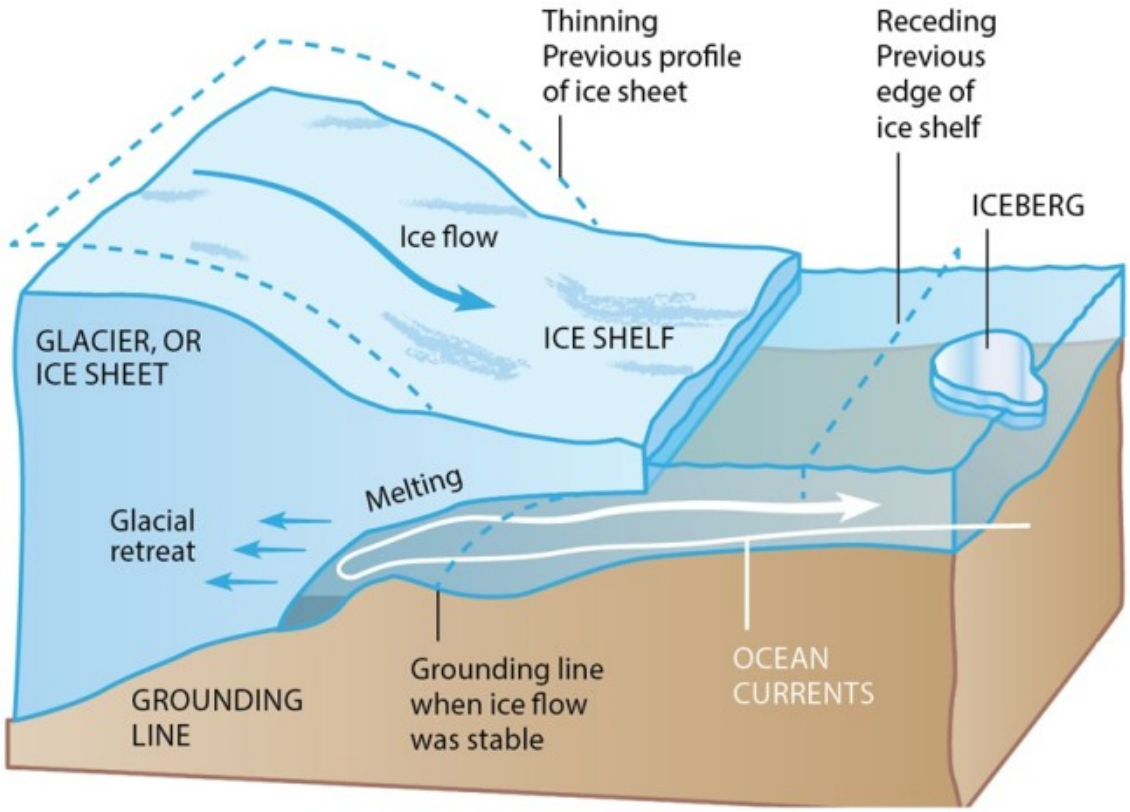

Figure 1.2: Schematic of the glacial mass balance at the terminus of a marine-terminating glacier. Snow accumulates at higher elevations, turning to firn and finally ice, adding to the glacial ice mass. The ablation zone here consists of mass loss through calving at the ice front, as well as basal melting, and the dynamic thinning caused by the increased speed of flow of the ice itself reducing the time available for accumulation at higher altitudes. Image from Jay Smith after National Snow and Ice Data Centre (NSIDC).

the base of the glacier, which is linked primarily to the thickness of the ice, the rate of meltwater production and the extent to which the glacier is confined. Surge glaciers are known to undergo periods of rapid advancement, which can be triggered by a tipping point of basal meltwater or relief of the bed causing an accumulation of mass to a critical point.

In marine-terminating glaciers (Figure 1.2), this is complicated by the physical effect of the water on the base of the glacier. The point where the glacier starts to float on the sea surface (grounding line) is very vulnerable to basal melting due to increased water temperatures (*DeConto and Pollard*, 2016; *Khazendar et al.*, 2016), which can cause "calving" events; through which a quantity of glacial ice breaks away from the ice shelf and floats on the water. This basal melting also increases the speed of the glacial flow, removing the extra support offered by the

calving front. This increase in speed results in a reduction of the time available for consolidation of accumulated snow and conversion into firn and glacial ice. This "dynamic thinning" results in a thinner glacier or ice sheet. Contributions from glaciers to sea level occur when the ice enters the ocean either as run-off from meltwater or floating of the ice in the form of ice shelves or icebergs.

Knowledge of ice sheet relief allows monitoring of the ice flow (*Brooks et al.*, 1978) and inference of the terrain on which it is based (*Lythe and Vaughan*, 2001). The calculation of the ice-sheet mass balance is a large unknown in many models, and any changes in such regions can be an important quantification of how the ice sheet is responding to climatic change. Volumetric approaches to the calculations require accurate data regarding the elevation of the ice sheet and can give an overview of the changing nature of the sheet itself - such as any notable accumulations or ablations of the glacial ice.

1.2.1 Snow on Glacial Ice

Due to the origin of glacial ice as snow, it is often hard to quantify the amount of snow on top of it, and therefore delineate the surface of the ice itself for the understanding of surface energy fluxes, quantification of surface mass balance change and hydrographic basin delineation. The transition from snow, to firn, to glacial ice involves a shift in density, water content and therefore in the dielectric properties of the ice itself. Fresh snow increases attenuation and complicates the reflected signal. Whilst laser altimeters are widely thought to measure the very top of the snowpack, this is more complicated for radar altimeters due to penetration of the signal into the surface layers. The degree to which the signal penetrates (and therefore the depth of the measured reflective surface) will be dependent on conditions in the snowpack including the temperature, density and moisture levels of the snow. With respect to the question of mass balance, it is often not the location of the ice surface below the snow that is of importance, but the knowledge of the water volume contained in it. Models of snowpack density can often be employed therefore in areas of known snowfall as it important to understand, not the location of the surface, but the volume of water held. In this thesis, the effect

of snowpack on the surface of the glacial ice is considered as a contributing factor to the uncertainty in height estimates, e.g., it is believed that for dry snow zones in Antarctica, penetration depths can be up to 300 m (*Cardellach et al.*, 2012). However, in order to account for this error or estimate the penetration depth, it is necessary to know the conditions of the snow and ice at the time of retrieval, which are usually unknown. This penetration into snowpack makes it harder to compare measurements using differing electromagnetic wavelengths (e.g., Global Navigation Satellite Systems-Reflectometry (GNSS-R) L-band 19 cm, Cryosat-2 Ku-band 2 cm), but where measurements are contemporaneous, this (in principle) allows the comparison to yield extra information about the surface and sub-surface properties (*Stroeve et al.*, 2020). This aspect of the problem is beyond the scope of this thesis.

1.3 Sea Ice

1.3.1 Formation of sea ice

Sea ice is formed when sea water is cooled below its freezing point (typically around -1.9°C for sea water), at which point, pure ice crystals form frazil ice and the brine is rejected. This brine is rejected both into the ice itself and into the water around, the latter process increases the density of the surrounding waters to create the deep-flowing bottom waters integral for the oceanic circulation and delivery of cold, nutrient-rich waters to the deepest parts of the ocean. Pockets of brine created between crystals result in the ice (known as frazil ice) being a combination of pure ice, brine, air and salt crystals (*Schwerdtfeger*, 1963). The conditions under which the ice forms affects the characteristics and therefore the properties of the ice itself. New ice will form as frazil initially before joining with other crystals. Figure 1.3 displays the dynamic development of ice primarily through ridging and rafting (whereby movement of floes into one another causes floes to buckle or pile on top of one another) into the various types and the associated thicknesses. Thermodynamics can also allow the growth of ice in the form of columnar ice (congelation ice) where the water freezes directly onto the ice, however this is a slower growth process often associated with calmer waters.

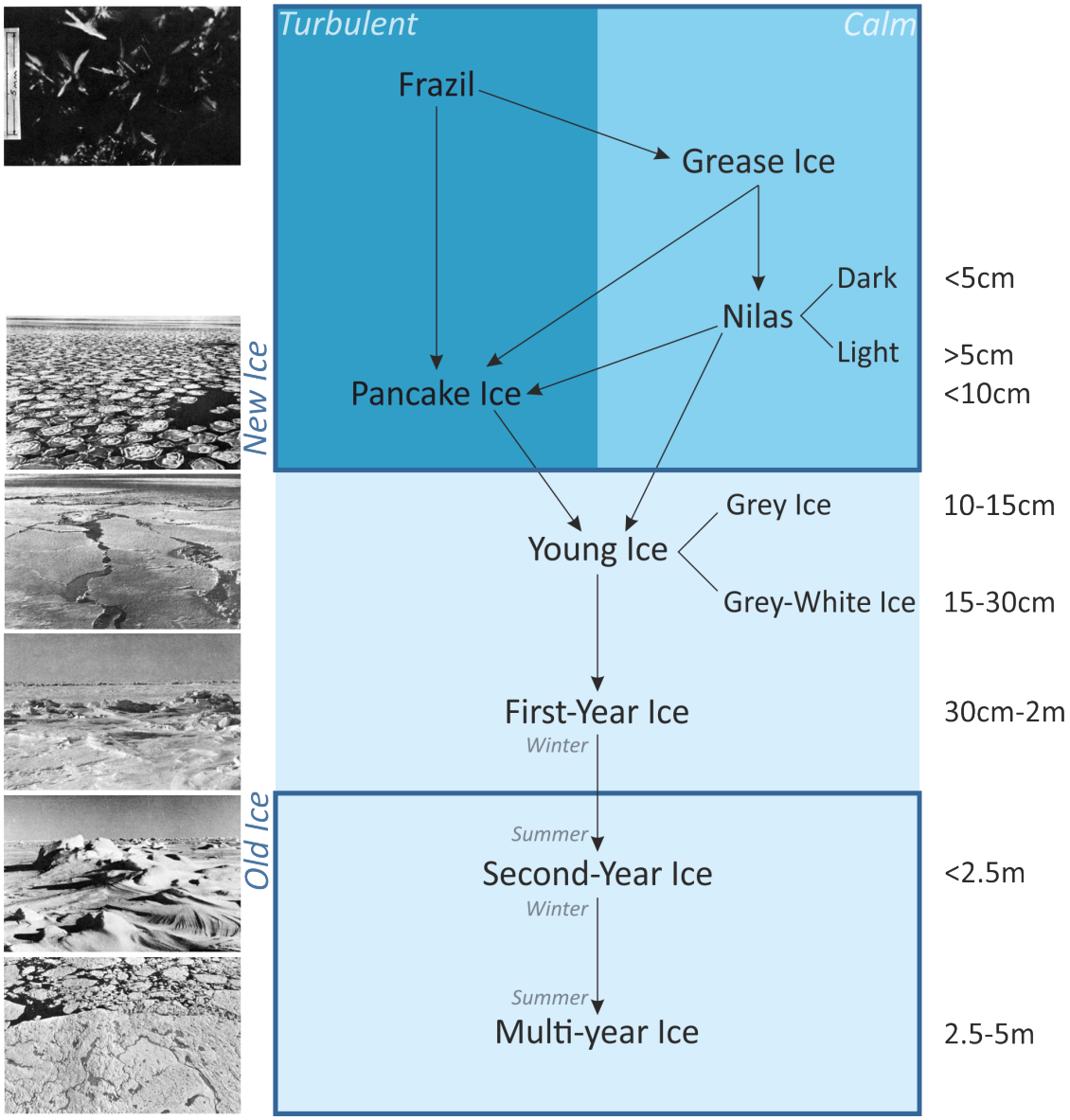

Figure 1.3: Development of ice and ice types with images (left) and thicknesses (right). Images (top to bottom): frazil ice, pancake ice, young ice, first-year ice, second-year ice and multi-year ice (*WMO*, 1970).

The term "frazil ice" covers ice crystals suspended in needle, spicule or platelet forms (Figure 1.3), as these aggregate in dynamic environments they enter the "pancake cycle" whereby pancake ice floes combine. These "pancake" floes are circular in form due to the aggregation of frazil particles on the outer edges. They usually have raised edges (Figure 1.3 and 1.4) due to their continual movement into one another. This rapidly forms large amounts of sea ice through rafting of floes atop one another (*Lange et al.*, 1989). In less dynamic environments, they continue to form ice crystals on the peripheries, giving grease ice and nilas. This is then termed "Young Ice" and continues growing in this way until it is 30 cm in

Figure 1.4: Pancake ice in a dynamic environment in Nordfjorden, Svalbard. Rafting can be seen in the foreground, with pancake floes pushed atop each other. These collisions form the raised edges that can be seen on individual floes. Image ©Susanne Landolt

thickness, when it is "First-Year-Ice" (*WMO*, 1970). Having lasted through one summer it is "Second-Year Ice" and after two it is "Multi-Year Ice".

1.3.2 Types and properties

In order to detect these different ice types remotely using electromagnetic waves, it is necessary to consider their differing physical and chemical properties and how they will interact with the chosen method through which they are to be monitored. The volume scattering, surface scattering and reflectivity (through the dielectric constant) are key properties in determining the signal received. The reflectivity of the ice and its surface scattering will be impacted largely by atmospheric and oceanographic dynamics, however the dielectric constant component depends largely on the physical and chemical properties of the surface itself and will be reliant upon the brine content of the ice (*MacGregor et al.*, 2007). This in turn is affected by the temperature regime of the ice at the time of monitoring (with faster freezes resulting in narrower plate spacing and more brine channels) and will generally

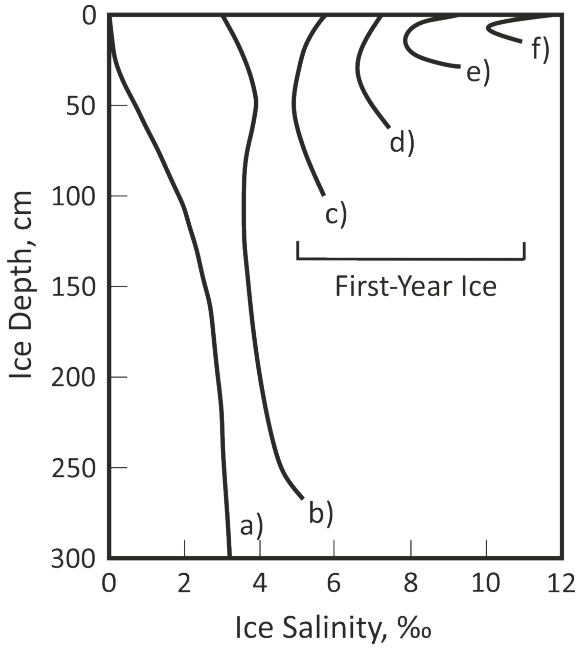

Figure 1.5: Idealised salinity profiles for various thicknesses of ice adapted from *Maykut* (1985). a) and b) represent multi-year ice, with a) showing the regions below elevated areas such as hummocks and b) typifying salinity profile of low ice where surface is very close to freeboard. Curves c)-f) represent first year ice.

decrease with the age of the ice.

As the rate of freezing is fastest at the air-ice interface, this gives a 'C' profile (Figure 1.5, curves c)-f)), with highest salinities at the surface. As the ice thickens and ages, desalination occurs due to gravity drainage and increases throughout the melt season as brine channels coalesce and are 'flushed' with melt water before undergoing pressure-forcing of brine out of the cavities during the refreeze (*Bi et al.*, 2013; *Lomax et al.*, 1995). This leads to the changing brine inclusions with age and depth as seen in Figure 1.5. These changing properties affect the attenuation of microwaves which depends largely on ice conductivity (*Eicken*, 1992; *Schwerdtfeger*, 1963; *Zirizzotti et al.*, 2016).

The ice crystals are re-textured over time, with rounder boundaries and removal of brine platelet layers. This, combined with the desalination results in the formation of a surface layer which is often much lower in density and salinity than the ice below. Ponds from surface melt, ridging and rafting exacerbate this surface effect, giving a hummocky and higher relief surface and allowing the multi-year ice to be easily identified. Snow cover will impact electromagnetic wave attenuation

from the surface of the ice due to its much lower density (*Timco and Frederking*, 1996) as well as smoothing ice relief. This complicates the measurement of both the height and classification of the ice surface through the masking of surface relief features and reduction in scattering from the ice itself, with much energy lost to volume scattering in penetration of the snow layer.

The dominance of different processes at the two poles results in a visible difference in the types and textures of ice seen. For example, most Antarctic ice is much younger than Arctic ice due to the efficient seasonal ice export (dropping to 15% of its area in the summer months in contrast with 40% in the Arctic, (*Cavalieri et al.*, 1996)). This results in thinner ice in the Southern Hemisphere and the dominance of young ice (*Lange et al.*, 1989), whilst the continued production of ice caused by this export gives a higher salinity. As granular ice dominates over columnar (congelation) ice in the more turbulent environment of Antarctica, it is thought that the crystals may also impede the desalination of the ice due to a lack of efficient brine channels (*Carnat et al.*, 2013).

1.3.3 Snow on Sea Ice

As this research focusses only on the detection of sea ice, the presence of snow does not affect our water / ice classification. Therefore, this aspect is not pursued in this thesis beyond the below explanation of its importance in the cryosphere, and difficulty associated with its characterisation. For more details on snow on sea ice see *Massom et al.* (2001).

Snow plays a key role in atmosphere-cryosphere interactions through its alteration of radiative fluxes and albedo as well as changing the density of the ice, concealing the location of the surface of the sea ice and affecting the dielectric properties of the surface itself (*Maykut and Untersteiner*, 1971). It is also due to these factors that snow can drastically affect the retrieved signal of both active and passive remote sensing techniques.. This difficulty in determining the snow's characteristics means that this can lead to significant uncertainties in many models of the climate and hydrological systems, and more difficulty in accounting for snow effects in sea ice analysis. In addition to the alteration of signal scattering off the

surface, the presence of snow on the sea ice affects the physical relief of the landscape, collecting in hummocks and reducing perceived roughness, obscuring ridges seen on older ice and making it harder to classify ice type from backscatter alone (*Drinkwater et al.*, 1995). Snow also has a large effect on our ability to measure the thickness (and therefore volume) of sea ice (*Giles et al.*, 2007), through the complication of the position of the reflective surface. Whilst laser altimeters are widely believed to reflect off the snow-air interface, the reflecting surface for radar altimeters is varies due to the differing density of the snow on the sea ice and the possibility of negative freeboard – whereby the surface of the ice is below the surface of the water due to the presence of snow (and possibly snow ice). These conditions are more commonly associated with the Antarctic (where the younger, thinner ice may have a deep snow cover). However, with the thinning of Arctic ice, these conditions are now widely seen in the Northern Hemisphere too (*Rösel et al.*, 2018).

1.4 Satellite Remote Sensing of the Cryosphere

Satellite remote sensing allows a wide array of data to be collected on a large scale, as necessary for the broad coverage and dynamic nature of cryosphere data. This generally falls into the categories of "active" or "passive" remote sensing. The former indicates that the surface is being sensed with signals transmitted by an associated platform, either co-located (monostatic) or on a separate platform (bi-static or multi-static), whilst the latter refers to the use of ambient radiation, often referred to as "radiometers". Global Navigation Satellite Systems-Reflectometry (GNSS-R) falls between these two categories, using signals transmitted by Global Navigation Satellite Systems (GNSS) satellites. It therefore has the higher signal power of active sensing techniques, but without control of the wavelengths, powers and geometry of the sensing medium.

1.4.1 Active sensing

Active sensing methods use a transmitter and receiver to send a signal out and receive the signal back. Often the transmitter and receiver are co-located on the same platform, in a monostatic configuration, although occasionally bistatic (two platforms) or multi-static (more than two) is used. Active techniques are much higher energy than passive techniques and are highly effective in measuring many properties of ice, most notably the height or freeboard (and therefore thickness) of both glacial and sea ice and can be performed using radar or laser.

The deformation of the glacial ice throughout the transport to the terminus leads to varying physical characteristics due to the large amount of deformation and freeze-thaw cycles it undergoes associated with its transport. These changes make it difficult to assess the interaction of electromagnetic waves with the surface of the ice, as it is highly temperature dependent. Many satellite remote sensing techniques (especially those reliant on microwave frequencies) are highly sensitive to the presence of water, impacting attenuation of the waves within the ice sheet, and therefore the extent to which the signal penetrates the surface. This increases uncertainty in measurements, as it is not always possible to accurately determine the surface from which the reflection has been received. Knowledge of sensing conditions can greatly aid in the estimation of factors such as penetration depth, however for similar reasons, this is also difficult to accurately predict over less stable areas (*Shepherd et al.*, 2019). A benefit of laser altimetry such as Airborne Topographic Mapper (ATM) from Operation IceBridge (airborne altimetry mission) and IceSat-2 (spaceborne laser altimetry) is that the penetration into ice and snow is negligible, such that it is assumed to be measuring the height of the surface itself. This is in contrast to radar altimetry that may be measuring the ice under the snow or the firn, depending on the conditions of the surface at the time (*Lenaerts et al.*, 2019).

Owing to the need to power a transmitter in addition to a receiver, active sensing techniques have greater power demands in addition to being higher in mass and therefore cost than passive techniques. However, often they can provide higher resolution and greater detail, as they are not limited to ambient frequencies. An

extreme case of this is Synthetic Aperture Radar (SAR), in which the antenna is effectively lengthened through the travel of the satellite between transmitting and receiving the pulses, allowing up to 100 m of horizontal resolution, sufficient for textural analysis and classification of sea ice (*Soh et al.*, 2004). However, the high data load and associated downlink and computing costs mean that SAR data often has limited coverage, operating in narrow swaths. Sensors such as Synthetic Interferometric Radar Altimeter (SIRAL) seen on board European Space Agency (ESA)'s satellite CryoSat-2 have now been developed specifically for the monitoring of the ice sheets and sea ice freeboard (*Phalippou et al.*, 2001), combining synthetic aperture with radar altimetry to provide high resolution height estimates.

Satellite altimetry of ice is usually performed using radar or laser in a monostatic configuration as heights are conventionally measured at nadir (measurement perpendicular to satellite velocity), requiring the transmitter and receiver to be present on the same platform. Missions currently in orbit for this purpose include CryoSat-2; launched by the ESA in 2010; and IceSat-2; launched by the National Aeronautics and Space Administration (NASA) in 2018. These work in radar and visible frequencies respectively and open up the possibility of a combination product to enable the benefits of the two frequencies to be exploited for understanding of snow cover. The orbit of CryoSat-2 was recently changed to facilitate this work, moved almost 1 km higher in its orbit in order to achieve a better phase with the IceSat-2 orbit. The use of these monostatic techniques for glacial ice altimetry combined with the necessary tilt of the satellite's orbit result in a compromise between coverage at the geographic pole and coverage elsewhere. The result is usually that polar orbiting satellites are put into orbit at a high inclination (92° for both IceSat-2 and CryoSat-2), allowing them to attain almost complete coverage of the polar areas, but unable to capture the 2° of latitude surrounding the geographic poles. This gives a 'polar hole' in the majority of Digital Elevation Models of the Antarctic Ice Sheet, where no satellite altimeters can measure.

Active sensing allows full control of the power of the signal as well as the angles of transmission and receipt, an element that is exploited by scatterometers. These sensors measure the reflection of microwaves off a surface usually at a variety of

incidence angles (angle between incoming radiation and the normal of the reference surface, eg. ellipsoid) and azimuth angles (direction of signal with respect to the velocity of the satellite). This allows analysis of the scattering for surface characteristics, often utilising a wide range of frequencies, polarisations and incidence angles. This is in contrast with SAR, which is usually normalised to one solitary incidence angle for consistency across the swath. Scatterometers therefore allow effects due to viewing angle (incidence and often azimuth) to be accounted for and parameterised. These parameterisations often reveal characteristics of the surface itself such as relief and moisture content. Sensors such as Advanced Scatterometer (ASCAT) (C-Band) have therefore been explored extensively for their use in characterisation of the cryosphere, a summary of such parameterisations can be seen in *Fraser et al.* (2014) and application of these techniques in *Fraser et al.* (2016).

1.4.2 Radiometers

Radiometers comprise only a receiver, using ambient radiation to sense targets rather than emitting the signals themselves. Due to the use of ambient radiation, these 'passive' remote sensing techniques are often much less expensive than their active counterparts. These are usually used to assess surface characteristics of ice and are thus usually applied to sea ice concentration and surface melt analysis, with their resolution limited by the frequency at which they operate.

Among the highest resolution radiometers available are those of infrared and visible radiometry (3 - 750 THz). These are able to attain resolutions of 250 metres (and even 1 metre (*Kwok*, 2014)) as seen in the MODIS satellite products (Figure 1.6), however the prevalence of clouds over the areas of interest leave this technique at a disadvantage for monitoring of the cryosphere (*Lomax et al.*, 1995). It is possible to differentiate between water vapour cloud and ice (or ice clouds) where visible radiometers are combined with infrared (such as from Advanced Very High Resolution Radiometer (AVHRR)), however removal of cloud cover is not possible with these alone. Where cloud-free, the high resolution allows ice forms to be clearly seen and classified (Figure 1.6), however the use of infrared alone for sea ice classification is limited due to the regional variability of temperatures at the

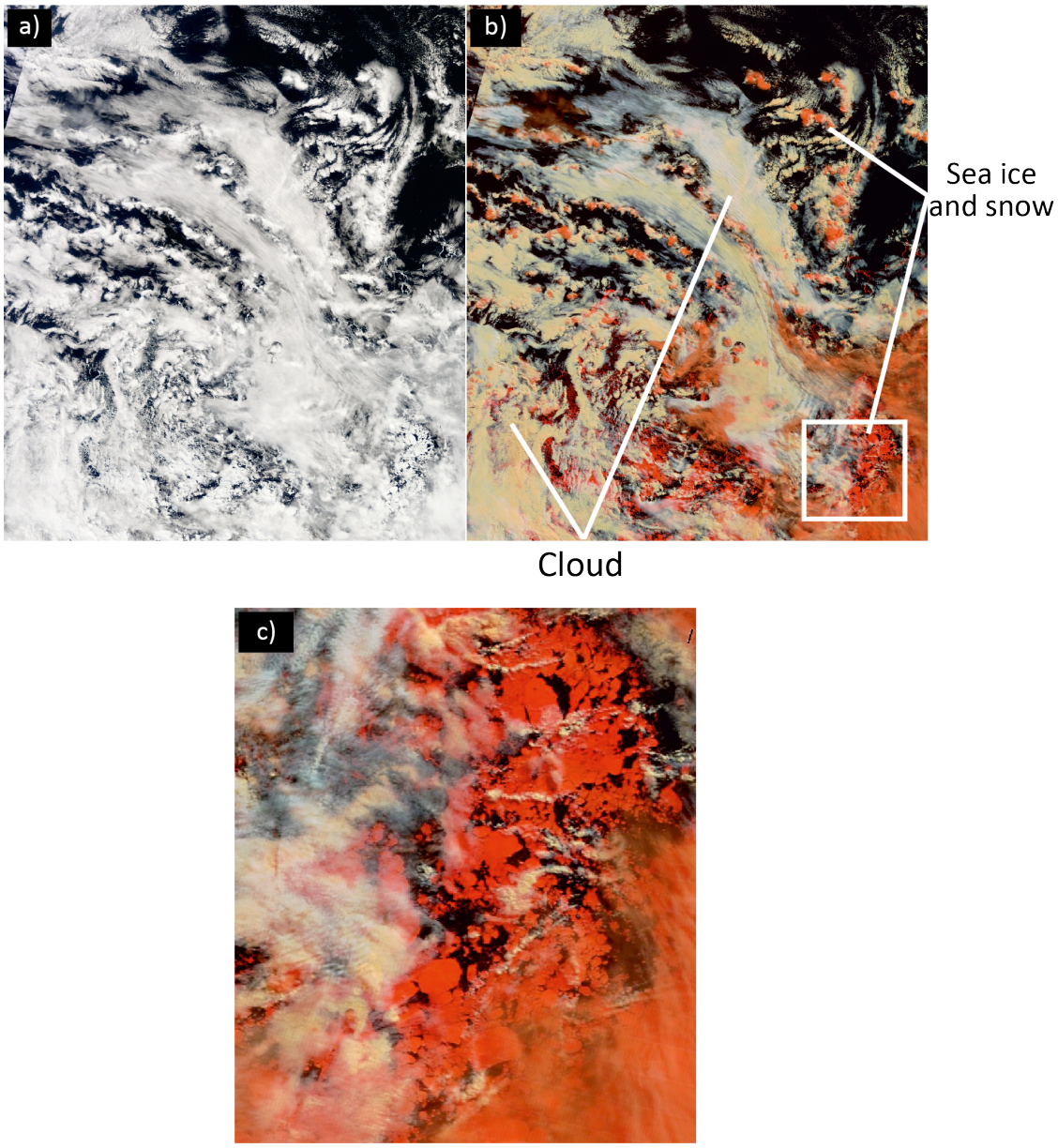

Figure 1.6: Moderate Resolution Imaging Spectroradiometer (MODIS) Terra satellite data (250m resolution) for the South Sandwich Islands in bands a)1, 4 and 3 and b) 3, 6 and 7 for Red, Green and Blue respectively. Bands 6 and 7 contain infrared data, whilst 1, 3 and 4 detect frequencies in the visible spectrum. The white box in b) outlines area seen in c) visible ice floes (red). *NASA/GSFC, Rapid Response.*

ice-air interface which prevents the application of simple thresholds for sea ice types or even open water (*Markus and Cavalieri*, 2000). In addition, ice clouds can be prevalent over the areas of interest for polar data, which are often indistinguishable in infra-red imagery from sea ice itself.

The first passive microwave (1-100GHz) sensor for sea ice was the Scanning Multichannel Microwave Radiometer (SMMR) in 1978, before this was developed into

SSM/I (1987) and finally Special Sensor Microwave Imager / Sounder (SSMIS) in 2005, continuing to provide sea ice concentration data to NSIDC. The latter two can function at higher frequencies than SMMR and measure both horizontal and vertical polarisation, allowing high resolution data acquisition and less atmospheric influence (*Lomax et al.*, 1995). The algorithms used to interpret these signals are often limited in their application to the frequencies offering the coarsest spatial resolution such as 19 GHz channels (*Bi et al.*, 2013; *Markus and Cavalieri*, 2000) and in some studies differences amongst algorithms can be equivalent to a decade or two's sea ice decline (*Ivanova et al.*, 2014). Areas with the lowest sea ice concentrations are most heavily affected by these inter-algorithm differences as atmospheric effects dominate the signals. Advanced Microwave Scanning Radiometer-2 (AMSR2) is less affected by this due to the use of two extra channels (50.3 and 52.8 GHz) allowing the removal of atmospheric effects. The larger range of the frequency channels (extending to 89 GHz) also allows the detection of small features such as small polynyas and leads (*Comiso et al.*, 2003). Many remote sensing techniques including AMSR2 have difficulties in determining sea ice classification in melt season due to the presence of water atop the ice. This limits their use to mainly winter measurements (*Bi et al.*, 2013; *Hong*, 2010).

ESA's Soil Moisture and Ocean Salinity (SMOS) mission estimates sea ice thickness using microwave radiation of a much lower frequency, comparable to that used in GNSS-R (as discussed below) at around 1.4 GHz. The penetration depth of this frequency allows the thickness of particularly young ice (less than 0.5 m) to be accurately estimated at around 35 km in horizontal resolution (*Kaleschke et al.*, 2012; *Mecklenburg et al.*, 2016).

1.5 GNSS-R

Global Navigation Satellite Systems-Reflectometry was first proposed in 1988 (*Hall and Cordey*, 1988) and uses reflected L-Band radiation from GNSS signals such as those of Global Positioning System (GPS) to characterise the Earth's surface. At present this is predominantly used for monitoring winds (*Clarizia and Ruf*, 2016; *Foti et al.*, 2015, 2017; *Ruf and Balasubramaniam*, 2019) and significant wave

height, however it is also being explored extensively for other Earth observation purposes such as soil moisture measurement (*Chew et al.*, 2016), sea surface height (*Clarizia et al.*, 2016) and sea ice monitoring (*Gleason*, 2006; *Rivas et al.*, 2010).

The use of GNSS-R for altimetry purposes was first proposed by *Martín-Neira* (1993) through a PARIS (Passive Reflectometry and Interferometry) System, and has been very successful over a wide range of studies including fixed, airborne and spaceborne experiments in both phase-delay (phase of signal at receipt) and code-delay (time of signal receipt) configurations. Its use to detect sea ice is a growing field, first investigated by (*Komjathy et al.*, 2000). GNSS-R gives the benefits in resolution and power of active remote sensing through the use of a strong reflected signal, whilst retaining the advantages of passive remote sensing through the need only for a receiver. This means that it offers an inexpensive solution for studies of the cryosphere, with many successes, not only in sea ice detection (*Alonso-Arroyo et al.*, 2017; *Yan and Huang*, 2016) and characterisation (*Rodriguez-Alvarez et al.*, 2019), but also sea ice altimetry (*Hu et al.*, 2017; *Li et al.*, 2017) and glacial ice altimetry (*Rius et al.*, 2017). The previous studies in these areas have focussed on select tracks, seasons or locations, rather than the broad multi-annual, multi-hemisphere approach to be presented here.

Much of the difficulty in using the reflected GPS signal to characterise sea ice stems from the unknown interaction of the L-band waves with the snow or ice surface, and the variation in the size of the area from which information is received covering tens of kilometres. Figure 1.7 shows the bistatic arrangement, with the receiver (for example TechDemoSat-1 (TDS-1)) looking at an area on the Earth's surface. TDS-1 chooses which satellites' signals to track depending on which yield the highest antenna gain, and are thus of the highest quality (usually at least one, but up to 4). The point of reflection (specular point) is calculated based on orbit simulations of the receiver and transmitter positions and projected onto the ellipsoid (Figure 1.7). At the point of reflection, the GPS signal will be affected not only by the surface at the specular point, but also the surface around it (glistening zone), depending on the relief of the surface. The signal is therefore highly susceptible to surface roughness and it is for this reason that it lends itself well to

monitoring and characterising sea ice, with roughness varying considerably with sea ice maturity (Section 1.3).

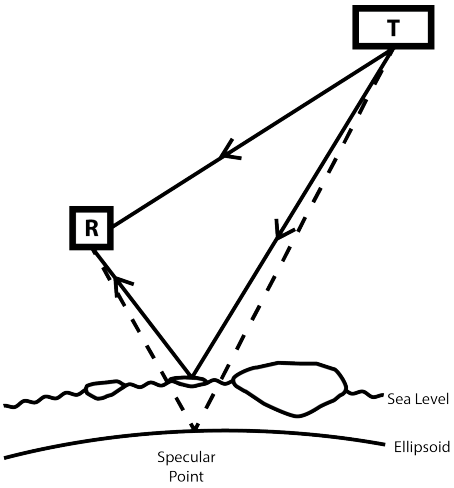

Figure 1.7: Bistatic arrangement of GPS satellite (T - altitude $\sim$ 20,180 km), GNSS-R satellite (R - altitude $\sim$ 635 km) and specular point, with modelled incidence angle to ellipsoid (dashed line) and signals to receiver and incident on surface (solid line).

GNSS-R data are usually received as a series of delay-Doppler Maps (DDMs). These can be seen as a map of the scattered power in delay and Doppler and imagined on the reflective surface as iso-Doppler lines and iso-delay contours (Figure 1.8). Reflections within these zones map to their respective point on the DDM - note that one bin in the DDM may represent up to two zones on the surface (for example blue or purple regions in Figure 1.8). A smooth reflecting surface produces a strong, coherent reflection in GNSS-R. This means that the scattered power comes almost entirely from the specular point, and the glistening zone is very small. This is visible where the specular point can be seen to move from open ocean to over ice (Figure 1.9) where the DDM changes from a spread, horseshoe-shaped DDM (T_1) to a high-amplitude DDM, focussed in both delay and Doppler space (T_2). The corresponding DDMs will have a pronounced peak and a limited spreading of the power distribution. Ice is considered smooth compared to open water at the scale of GPS L-band wavelength (19 cm), giving particularly strong reflections in the DDMs and making them ideal for the extraction of height information. An example of a more specular DDM can be seen in Figure 1.9 (T_2). These signals were first shown to be sensitive to sub-metre ice elevation changes in 2004 (*Cardellach et al.*, 2004), and more recently have been proven to distinguish sea, transition zone

and glacial ice (*Rius et al.*, 2017).

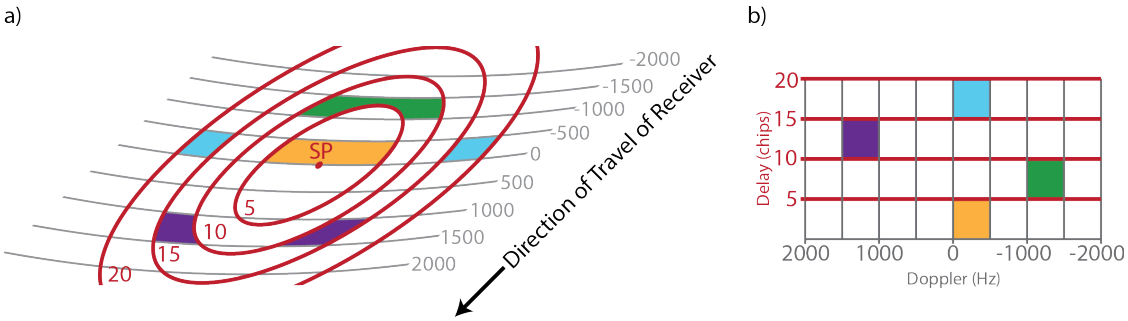

Figure 1.8: Schematic of DDM creation from the specular point with glistening zone (a) to DDM (b). Iso-Doppler and iso-delay lines are shown in grey and red respectively in both. Example regions are colour-coded to match the region on the surface (a) and how it maps to the simplified, low resolution DDM (b).

Owing to the use of signals of opportunity and the lightweight nature of the receiver, the harnessing of GNSS-R for the monitoring of the cryosphere would provide an inexpensive yet highly effective solution. The recent launch of the Cyclone GNSS (CYGNSS) constellation in 2016 for the application of GNSS-R to wind measurements brings up the possibility of a polar mission of a similar format. Reflections over sea ice are much more coherent, and therefore stronger than those over oceans. This would give high temporal resolution (average 4 hour revisit time for CYGNSS satellites (*Ruf et al.*, 2013)), monitoring all aspects of dynamic systems. It is unfortunate that the tropical orbit of the CYGNSS constellations (35°inclination), designed for the monitoring of ocean winds and hurricanes, means that it is has no coverage over the polar regions. However, the potential benefits of similar constellations for sea ice interactions are clear.

Table 1.1 below compares a number of satellites routinely used for the sensing of the cryosphere and their respective footprints, expected coverage and design life in addition to estimates of their mission costs, including launch and ground-processing operations for the lifetime of the satellite. Although estimates of costs vary greatly for the missions, it is immediately obvious that GNSS-R is at least an order of magnitude lower in costs, even if we assume the use of tens of satellites in a constellation. Though there are minor compromises in terms of footprint size when compared with tailor-made, short term "pathfinder" missions, such as CryoSat-2 or ICESat-2, it must be considered that the lower cost to build and maintain such systems as GNSS-R offers a better, long term solution to monitoring the cryo-

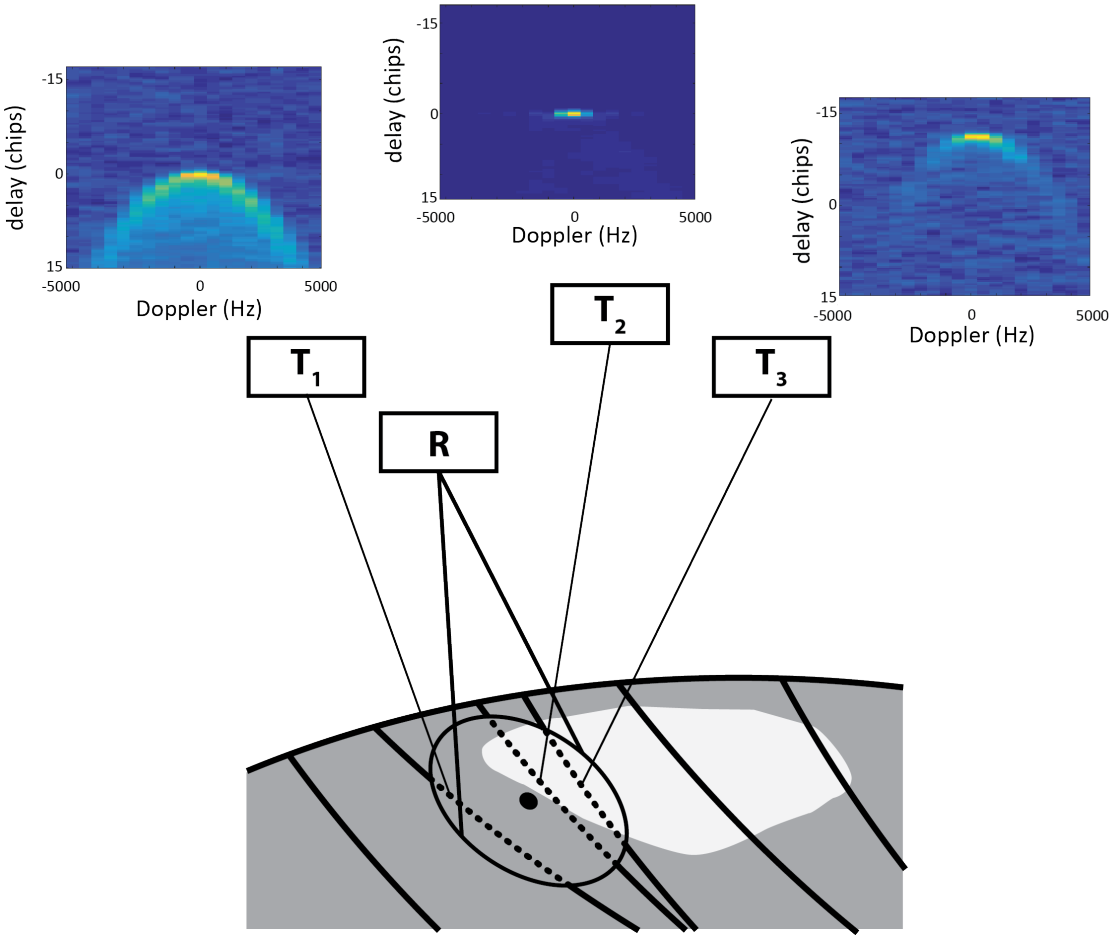

Figure 1.9: GNSS-R footprint and reflection retrieval - GNSS-R footprint and reflection retrieval. Tracks from GNSS satellites (T) are shown (solid lines), and are tracked (dotted lines) where they lie within the footprint of the GNSS-R receiver (R). Changes in the information received (in the format of DDMs) are seen where these are over open water (T_1), sea ice (T_2) and glacial ice (T_3).

sphere and the ability to build up climate records, as well as a smaller footprint than other passive techniques. In addition, as recently stated in an open letter from the cryosphere research community (*Fleury*, 2020), ICESat-2 and CryoSat-2 are due to reach their end-of-life a matter of years prior to the launch of their replacement (CRISTAL). It is critical, therefore, that observations over the polar regions continue. With the capability to build GNSS-R sensors (such as the Space GNSS Receiver - Remote Sensing Instrument (SGR-ReSI) used here) from off the shelf components, the speed of implementation of a GNSS-R constellation is comparatively fast. In combination with the possibility of piggybacking such small, low mass and low power sensors onto other mission launches, such an approach could potentially reduce the gap in measurements. The techniques described in Chapter

5 (sea ice detection), have, since publication, been made operational onboard commercial satellites in orbit, designed for Radio Occultation (RO) purposes. The flexibility of GNSS-R afforded by its low-cost and low-power nature allows it to fill the measurement gap and make a significant contribution to remote sensing of the cryosphere.

Table 1.1: Comparison of satellites routinely used for measurements over the cryosphere. Mission cost is given over the entire lifetime of the satellite, and due to the operational status of these missions, is in all cases a best-guess estimate.

Mission/ Program	Primary Payload	Sensor Type	Footprint	Coverage	Magnitude Cost/ satellite	Design Life (years)
GNSS-R 3U cubesat	-	GNSS-R	3 km^2 (0.5 km x 6 km)	Global; Varying web of points	1 M €	5
ICESat-2	ATLAS	Laser Altimeter	230 m^2 (17 m diameter)	Up to 82 degrees; Points along track	0.75-1 B €	3
CryoSat-2	SIRAL	Radar Altimeter	3.75 km^2 (250 m x 15 km)	Up to 82 degrees; Points along track	100s M €	3
DSMP-F18	SSMIS	Passive Microwave Radiometer	625 km^2 (25 x 25 km)	Global; Wide Swath	0.5 B €	5
SMOS	MIRAS	Passive Microwave Radiometer	2,500 km^2 (50 x 50 km)	Global Wide Swath	100s M €	5
MetOp-A/B/C	ASCAT	Scatterometer	300 km^2 (30 x 10 km)	Up to 82 degrees; Wide swath	0.5 B €	5
Radarsat-2	-	Synthetic Aperture Radar	Down to 3 m^2	Global; Narrow Swath	0.5 B €	7

1.6 Research Problems

As a pivotal interface for heat and energy exchange between atmospheric and oceanic sinks, sea ice is known to be one of the most important parameters affecting the global climate system (*Budd*, 1991; *Budikova*, 2009; *McCartney and Talley*, 1984). The interaction of the ice with these factors depends largely upon the presence or not and quantity of ice, types of ice and their characteristics, and as such the monitoring of these characteristics is vital in order to understand both the dynamic and thermodynamic ocean-atmosphere energy exchange (*Sansiviero et al.*, 2017) and through this the ice's responses and feedbacks. Due to the large scale and remote nature of this environment, and the resulting sample bias of in-situ measurements, the harnessing of satellite remote sensing for this task is essential. GNSS-R has proved reliable in measuring sea level and wind speed alongside other ocean variables (*Clarizia and Ruf*, 2016; *Foti et al.*, 2015). Owing to the reliance of the technique on signals of opportunity and the lightweight nature of the receiver, harnessing it for the monitoring of the cryosphere would provide an inexpensive solution. Were a constellation similar to that of CYGNSS to be developed for monitoring of the cryosphere, it would enable this dynamic system to be monitored at a much higher temporal resolution.

The application of GNSS-R to sea ice was first investigated by *Komjathy et al.* (2000) and has returned very promising results in the detection of sea ice concentration of both younger and older ice (*Gleason*, 2006; *Rivas et al.*, 2010). The expansion of these investigations to give additional quantitative links over longer time periods to physical aspects of the sea ice would allow the analysis of GNSS-R data already collected as well as raise the possibility of its use in future missions and application to active monitoring.

A strength of GNSS-R for applications such as these lies in the receipt of data from multiple specular points at any one time by the receiver. This, in addition to the asynchronism of the TDS-1 cycle with that of the GPS satellites, allows a varying web of specular points to be built up over time and therefore a high spatial resolution to be attained, as well as access to some points such as the poles, which

due to necessary satellite inclination, have thus far not been possible to measure using active techniques. This can be seen in Figure 1.10.

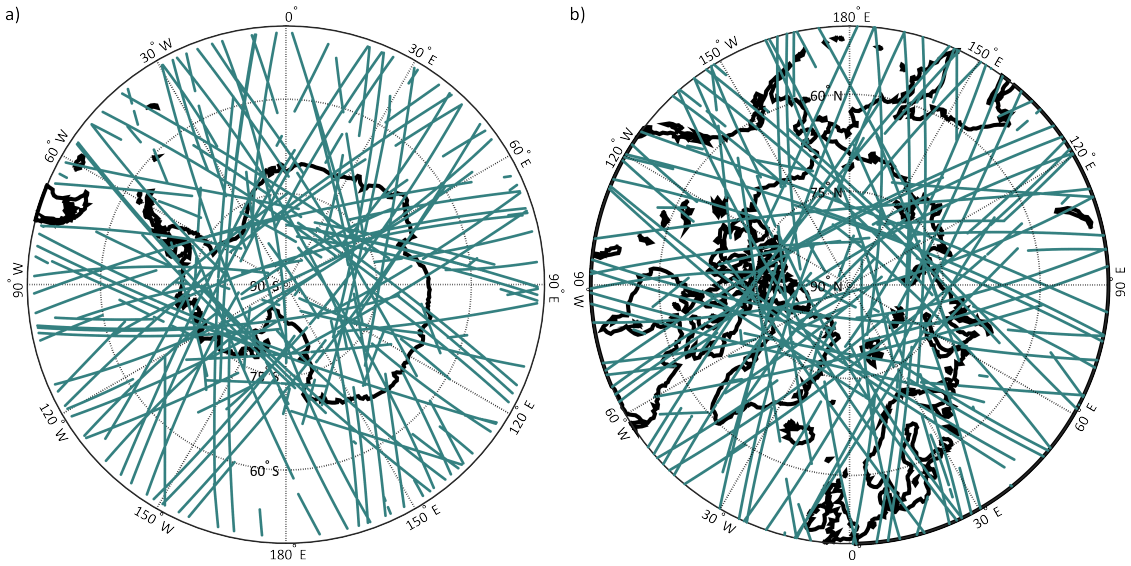

Figure 1.10: Maximum data received over one day in the Antarctic (a) and Arctic (b) by TDS-1, receiving a maximum of four GPS reflections at any one time with the single sensor. Date shown is 12th June, 2015 in Antarctica and 1st April, 2015 in the Arctic.

Difficulties in the use of GNSS signals stem from the unknown scattering of the signals from the sea ice surface as well as the extent of their attenuation within the ice. Sea ice roughness varies predominately due to the ice type and history but is also strongly affected by the presence of snow atop the ice surface which may even out the roughness of the ice itself, accumulating in dips and on windward sides of ridges (*Manninen*, 1997). All of these factors will impact the extent to which the reflected signal can be used to detect the sea ice or measure the glacial ice. It is essential that the performance of these data is assessed in relation to traditional techniques described in Section 1.4 if GNSS-R is to be a feasible complement to these established remote sensing techniques.

1.6.1 Thesis Aims

The aims of this thesis are to characterise the cryosphere with regard to sea ice physical attributes and glacial ice altimetry through use of GNSS-R observations from the TDS-1 platform. This will be achieved through the following aims.

Aim 1 Application of existing algorithm (*Clarizia et al.*, 2016) to glacial ice on the Antarctic continent in order to acquire a digital elevation model.

Aim 2 Extension of and improvement of glacial height calculations to assess expected accuracy of code-delay altimetry over the great ice sheets (including application over the Greenland Ice Sheet).

Aim 3 Demonstrate the potential for this dataset to allow novel sea ice detection to provide and assess the first multi-annual time series of ice extent using GNSS-R.

Aim 4 Connect derived parameters from TDS-1 data to external, co-located datasets to provide a comprehensive overview of the advantages and disadvantages of the use of GNSS-R over the cryosphere in relation to existing methods and products.

1.7 Project Structure

These aims will be addressed in three science chapters as follows. The first science chapter (Chapter 3) will outline the application of a sea surface height algorithm over the extent of the Antarctic Ice Sheet for the creation of an independent Antarctic Digital Elevation Model (DEM) using data from TDS-1, to fulfill Aim 1. These techniques will be revisited and improved upon in Chapter 4, with the inclusion of extra datasets, adjusted filters and enhanced processing of the waveforms in order to present an improved DEM of Antarctica and application across Greenland, as necessary for Aim 2. Chapter 5 will satisfy Aim 3 by describing the use of GNSS-R parameters for the detection of sea ice in both the Northern and Southern Hemispheres along with seasonal trends visible in the dataset.

All three science chapters compare to multiple external datasets (a minimum of 3 datasets independent of GNSS-R) in order to discuss the benefits of the technique and the potential for complementing traditional sensors (to meet Aim 4). These datasets and that of TDS-1 are detailed in Chapter 2, and allow a full discussion of Aim 4 within each science chapter as pertains to the particular application of

the technique. Conclusions of the thesis and potential for future work to improve the technique are given in Chapter 6.

Chapter 2

Data and Methods

2.1 GNSS-R data - TechDemoSat-1

TechDemoSat-1 (TDS-1); designed as a satellite technology demonstration platform by Surrey Satellite Technology Ltd (SSTL), ran eight experimental payloads, of which one was the Space GNSS Receiver - Remote Sensing Instrument (SGR-ReSI) from which the data in this project were obtained. Of these payloads, the SGR-ReSI along with an altitmeter make up the Sea State Payload. In addition to this, TDS-1 carried the Space Environment Suite (Micro Radiation Environment Monitor, Charged Particle Spectrometer, Highly Miniaturised Radiation Monitor and Micro Radiation Environment Monitor) to provide measurements of Space itself, the Air and Land Monitoring Suite (Compact Modular Sounder) and the Platform Technology Suite (CubeSat Altitude Determination and Control Subsystem, De-Orbit Sail and Hollow Cathode Thruster demonstration module).

The SGR-ReSI instrument is extremely low in mass (1.5 kg) and power consumption (consuming approximately 10 W) and is constructed from off-the-shelf components, the full details can be found in *Jales and Unwin* (2015). TDS-1 was launched in 2014 into a quasi-sun-synchronous orbit of 98.4 degrees inclination at an altitude of 635 km. The orbit is quasi-sun-synchronous due to a drift of 1.42 hours per year of the Local Time Ascending Node (*Foti et al.*, 2015). Due to the use of a shared platform, the SGR-ReSI was active 2 days in every 8 day cycle over the initial mission phase (November 2014 - July 2017).

However TDS-1 was then re-commissioned and the SGR-ReSI began continuous operation in 2018 to focus on the production of the Level 2 wind speed product. Only data acquired before the mission extension will be considered in the majority of this thesis, as data of antenna gain less than 0 dB was not downlinked during the 24-hour operational phase, unfortunately eliminating much of the data at high latitudes. In Chapter 4, data from the extended mission are included (August 2017 - December 2018) in order to increase the sample size.

2.1.1 TechDemoSat-1 data

Data from the SGR-ReSI are supplied in 6-hour bundles as NetCDF files from a publicly accessible database (merrbys.co.uk). These are provided as three separate files containing the metadata, delay-Doppler Maps (DDMs; synchronised by track numbers) and the power and noise of the direct signal (synchronised by nearest timestamp and Global Positioning System (GPS) satellite pseudo-random noise code). In order to reduce computation time and data volume, the data points around each geographic pole and their corresponding metadata were extracted, and these files used for all further analysis. The information from the direct (unreflected) signal, although explored was not used for any of the work in this project.

The delay-Doppler Maps (DDMs) are provided as 1-second incoherent averages made up of 128 delay pixels by 20 Doppler pixels, with a resolution of 0.252 chips ($\sim$0.246 µseconds) and 500 Hz respectively. Where reflections are coherent (such as over sea ice), these data are believed to correspond to a footprint of 0.4 km by 6 km in the across- and along- track directions respectively (*Alonso-Arroyo et al.*, 2017; *Hu et al.*, 2017).

2.1.2 Data Filtering

Filters have been applied to the raw data in order to eliminate and/or reduce noise and unsuitable data. Three principal filters are used to ensure basic data quality (seen in Figure 2.1), with a fourth, optional incidence angle filter applied due to overestimation of height measurements, which was used in Chapter 3.

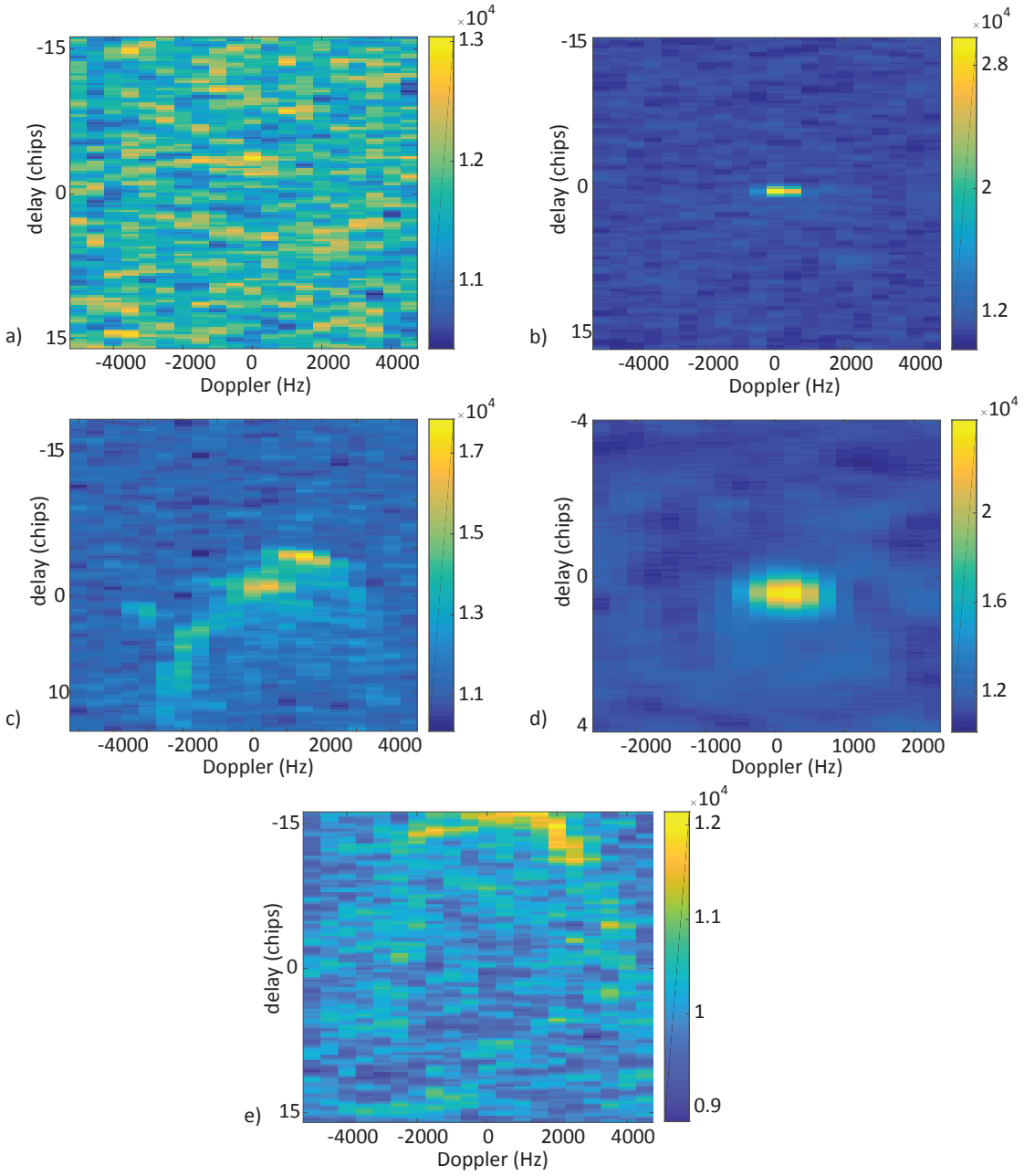

Figure 2.1: Illustration of filters applied, DDMs of scattered power a) DDM with a kurtosis of 3 (Gaussian), b) DDM with a kurtosis of 250, c) DDM flagged as containing the direct component of the signal, d) DDM in Collection Period 12, e) DDM showing signal outside of the tracking window.

1. *Kurtosis (κ) filter* - This filter is designed to remove the data which were majority noise. This is achieved by excluding points where the power distribution of the DDM is similar in coherence to a normal distribution. The threshold for this was placed at a kurtosis of 3.5 across the DDM. This threshold was chosen so as to ensure the removal of all noisy points below the threshold, and to account for the random nature of noise which causes some noise to have higher kurtosis than 3 (value for a Gaussian distribution as seen in Figure 2.1a). Different thresholds were explored with little improvement found at higher thresholds. In order to maximise both data quantity and quality, 3.5 was chosen.

2. *Quality flag filters* - Data that are flagged as containing the Direct Signal in the DDM are discounted due to disruption of the tracking of the reflected signal (Figure 2.1c), and those in Collection Period 12 (September 2016) are also filtered due to changes in DDM processor settings that made these DDMs inconsistent with the others considered (Figure 2.1d).

3. *Doppler filter* - As a technology demonstration mission, the sensor onboard TDS-1 is not optimised for applications far above the ellipsoid. As such, the window for tracking received signals is tied to the ellipsoid, which causes loss of signal at high elevations such as those over the Antarctic Ice Sheet (Figure 2.2). These data points have been identified by the maximum amplitude of the DDM straying from the central four bins of the DDM (as the central peak is not within the tracking window with respect to the ellipsoid). These have been filtered out where the Doppler value at the maximum amplitude (dop_{ma}) is outside the range:

$$\frac{dop_{min}}{10} < dop_{ma} < \frac{dop_{max}}{10} \tag{2.1}$$

where dop_{min} is the minimum of the Doppler axis and dop_{max} the maximum. These criteria remove all data points where the signal has left the tracking window (Figure 2.1e) and prevent saturation at the top of the tracking window. Further data removed are those where the maximum amplitude is in the first row of the DDM, as the entirety of the signal is not received.

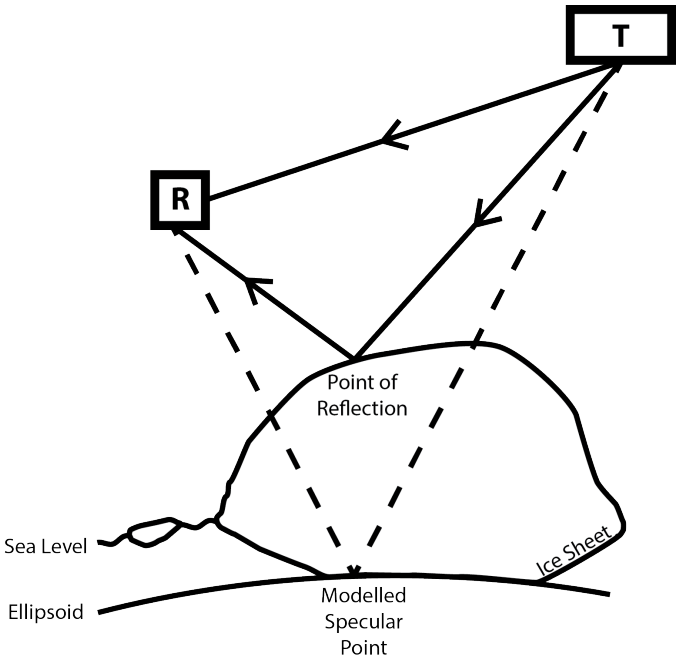

Figure 2.2: Illustration of reflections over ice sheet with transmitter (T) and receiver (R). Modelled specular point and incidence angle calculated from geometry of satellite locations (dashed line) and actual reflection point above (solid line). Orbital height of satellites not to scale.

4. *Incidence Angle filter* - An optional filter was applied to the data when estimating heights in Chapter 3, whereby data received at an incidence angle of 55° or greater were removed. This is due to observed overestimates of height at these incidence angles. As these overestimations are unconstrained and not fully understood the data were removed. Chapter 4 includes these data, using an additional processing step to account for these points.

In April 2015, the gain control of TDS-1 was changed from Automatic Gain Control Mode to Fixed Gain Mode. The data used in this project spans that acquired in both modes, as the overall power of the signal is not used in any of these studies. It was decided not to calibrate DDMs with respect to this nor to the power of the transmitted signal, as this calibration is not required for the analysis carried out here. The large number of parameters used in this project can be found in Appendix C. These require only the relative power within the DDM and its distribution along Doppler and delay.

The primary parameters used are described below. These use the delay waveform which corresponds to the column of the DDM through its maximum power, giving

the change in power through delay space. This is illustrated in Figure 2.3.

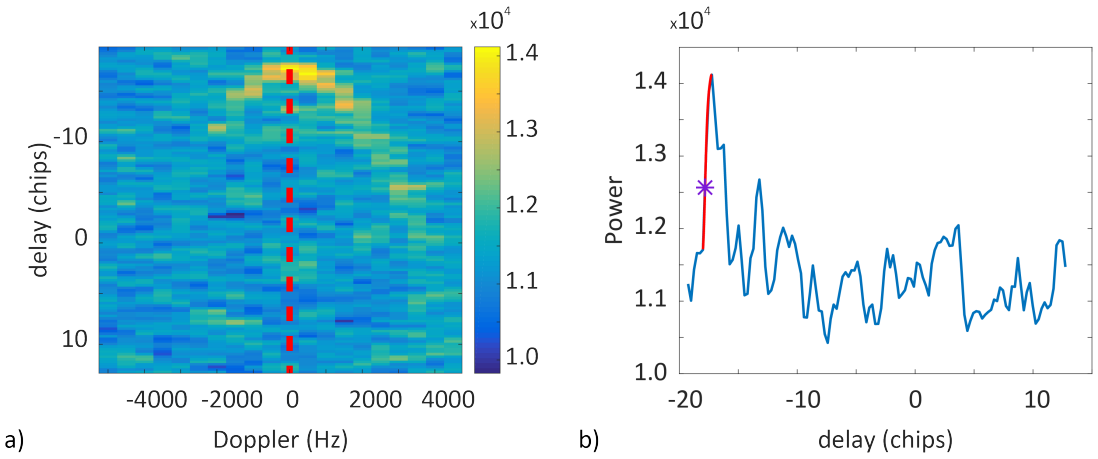

Figure 2.3: Method used to acquire delay waveform from DDM. The waveform in the delay domain is found at the maximum power (red dashed line, a)). b) Waveform in delay space. For parameter 1 below, the leading edge is then found (red) and the delay selected at its maximum first-order derivative (star).

1. *Delay at the maximum derivative of the leading edge of the waveform (chips).* This is the point of highest gradient on the leading edge of the waveform. Used for height estimates in Chapter 3, and illustrated in Figure 2.3b).

2. *Delay at p_{70} (chips)* - similar to the Maximum derivative of the leading edge, this is the delay at the point where the power is at 70% of the maximum on the leading edge. This parameter is used in Chapter 4 to improve height estimates from Chapter 3.

3. *Offset Centre of Gravity (OCOG) (chips)* - The difference between the delay at maximum power, and the centre of gravity of the waveform. Used in Chapter 5 to categorise waveforms with less scattered signal in order to detect sea ice.

4. $dy_{down}(85\%)$ *(chips)* - This is the difference between the delay at maximum power, and at 85% of the maximum power on the trailing edge of the waveform ('down' the DDM). Used in conjunction with OCOG in Chapter 5 to categorise waveforms with less scattered signal in order to detect sea ice.

2.2 Antarctic Ice Sheet Elevation Data

Four comparison Digital Elevation Models (DEMs) are used in Chapters 3 and 4 for the validation of the Global Navigation Satellite Systems-Reflectometry (GNSS-R) altimetry measurements over Antarctica. These use predominately satellite radar and laser altimetry with some input from airborne and ground measurements. They cover large periods of time and therefore do not show temporal changes.

The DEM used as a principal comparison for glacial ice altimetry over Antarctica (Chapters 3 and 4) is the CryoSat-2 1 km DEM v1.0 detailed in Section 2.2.1. This DEM was chosen as it was the most recent update to the Antarctic DEM, with a fine grid spacing at 1 km of resolution. It allows a simpler comparison to the GNSS-R data, through its use of only one sensor (Ku-band radar). This makes it easier to understand the differences between the techniques, their advantages and disadvantages as well as the possible sources of discrepancies. Additional DEMs (Sections 2.2.2 and 2.2.3) were compared to in order to give a perspective as to the DEMs available and the level of agreement expected between DEM products (Section 2.5). Reference information regarding these datasets' sources and formats are given below.

2.2.1 CryoSat-2 1 km DEM v1.0

This is the primary comparison DEM for the Antarctic study. It uses 250 million measurements from the CryoSat-2 radar altimeter (Ku-band) between July 2010 and July 2016, gridded at 1 km resolution using ordinary kriging where no measurements are available (*Slater et al.*, 2018). South of 88°S there are no data due to orbital constraints. Full details can be found in *Slater et al.* (2018) and the DEM itself is available at http://www.cpom.ucl.ac.uk/csopr/icesheets2/dems.html as a NetCDF file.

2.2.2 ERS-1 and ICESat

An earlier DEM from over 150 million measurements from ERS-1 in 1994 and 1995 and ICESat between March 2003 and March 2008 (*Bamber et al.*, 2009). The former uses radar altimetry at Ku-Band and the latter, laser. These measurements were weighted and combined, before being gridded using ordinary kriging. South of 86 °S cartographic data is merged to ensure coverage at the pole. Full details of calculation can be found in *Bamber et al.* (2009) and the DEM can be downloaded from http://nsidc.org/data/NSIDC-0422 as a binary file.

2.2.3 Bedmap2 Surface DEM

A large composite of DEMs as used for the production of the subsurface map of the Antarctic land surface (*Fretwell et al.*, 2013). Three maps were produced as part of this product - the map of the Antarctic bedrock, a map of the thickness of the Antarctic Ice Sheet and a Surface DEM (used here). In order to calculate this DEM, 4 different laser and radar altimetry DEMs were used in conjunction with ASTER and SPIRIT data (visual imagery) along with vector data sourced from cartographic data in the form of the Ohio State University DEM. Full details of calculation can be found at *Fretwell et al.* (2013) and the DEM can be downloaded from https://www.bas.ac.uk/project/bedmap-2 as a binary file.

2.2.4 Operation IceBridge (Dataset ID ILATM1B)

An airborne laser altimetry survey using the Airborne Topographic Mapper. This study only uses data collected within the time span of the TDS-1 mission, but is available from March 2013 to 2019 on an annual basis over both Antarctica and the Arctic / Greenland. Data are given along-track and can be acquired at https://nsidc.org/data/ILATM1B/. Due to the constraints of the platform, the spatial coverage is considerably lower, with a footprint of around 10 m^2 at 500 m of altitude.

2.3 Greenland Ice Sheet Elevation Data

In conjunction with the above elevation datasets of Antarctica, four comparison datasets over Greenland are used in Chapter 4 for the validation of the GNSS-R altimetry measurements. These comprise three DEMs and one airborne dataset and are largely based on measurements from photogrammetry, optical and radar altimetry. Many of the same instruments are used where satellite altimetry and airborne surveys are concerned. These do not show changes in elevation with time, as they are generally averaged over long periods.

The primary comparison used for the glacial ice altimetry over Greenland is the European Space Agency (ESA) Climate Change Initiative (CCI) Ice Sheet Product. The rocky peripheries and steep slopes of the Greenland Ice Sheet mean that all DEMs considered utilise a variety of techniques over different time scales and geographic regions. This lack of a single-sensor product over the region meant that it was necessary to choose the best combination of measurements. The ESA CCI aims to produce the highest quality data observations of the Essential Climate Variables, leveraging all Earth Observation sources to their full potential. The datasets are therefore carefully processed, with outliers removed, through a large investment of time and resources. Other datasets used for comparison here (Section 2.3.2 and 2.3.3) were chosen due to ease of access and availability of analysis of the datasets, so allowing for a complete understanding of their sources, advantages and disadvantages. The source and format of these datasets are described below for reference.

2.3.1 ESA CCI Greenland Ice Sheet product

This Digital Elevation Model was created by the Greenland Ice Sheet Climate Change Initiative by European Space Agency. Other products from the CCI include ice velocities, surface elevation changes and the mapping of calving fronts and ground lines. It is a composite of CryoSat-2 elevation measurements and the ArcticDEM (largely photogrammetry from WorldView-1, -2 and -3.) Full details can be found at http://esa-icesheets-greenland-cci.org/.

2.3.2 ERS-1 and Geosat DEM

An earlier DEM comprised of a variety of measurements across multiple missions (*Bamber*, 2001). Data are based on satellite (ERS-1 and Geosat) measurements from radar altimetry and aerial photogrammetry in conjunction with airborne (University of Kansas Ice-penetrating Radar, Airborne Topographic Mapper (ATM), Technical University of Denmark echo sounder) data. Full details of calculations can be found in *Bamber* (2001) and the dataset can be downloaded from https://nsidc.org/data/NSIDC-0092/ as a text file.

2.3.3 GIMP DEM

From the Greenland Ice-Sheet Mapping Project, this DEM was calculated by , *Howat et al.* (2014) joining the Bamber DEM described above with photogrammetric topography (periphery of Ice Sheet) and ICESat/GLAS laser altimetry data from 2003-2009. Data included in this DEM therefore spans almost two decades in order to approximate a mean surface. Full details of calculation can be found at *Howat et al.* (2014) and it can be downloaded at https://nsidc.org/data/nsidc-0645 as a TIFF file.

2.4 Sea Ice Data

The following comparison datasets are used in Chapter 5 to show the edge of the sea ice on a daily basis derived from different satellite remote sensing techniques. The variety of techniques in these products was essential for comparisons to assess the likely causes of discrepancies and the performance of the GNSS-R sea ice detection algorithm. Where sea ice concentration measurements are used from radiometers, any concentration above 0% was deemed to be sea ice and 0%, water. This threshold was used, rather than the conventional 15% concentration for sea ice coverage due to the sensitivity of the GNSS-R to the presence of sea ice. This choice was found to give the best agreement with derived parameters from the TDS-1 data and the largest separation of the two surface types. For more details,

see Chapter 5.

Similarly to the use of the ESA CCI product for the elevation of the Greenland Ice Sheet, the ESA CCI Sea Ice concentration product was used as the principal training and comparison data for the sea ice detection algorithm (Chapter 5). This was directly resulting from the "historical" nature of the data, as Near-Real-time data were not required, and therefore the product did not need to be an operational product. The use of historical data enabled the use of the carefully processed, ESA CCI product. This reduces extra outliers on the part of the "truth" product in order to ensure the cleanest possible comparison and training data, making it preferable to the National Snow and Ice Data Centre (NSIDC) sea ice concentration product. The use of only one type of sensor (passive radiometer) also made this dataset a better choice than other products such as the Ocean Sea Ice Satellite Application Facility (OSI SAF) (scatterometer and passive microwave) and Multi-Sensor Analyzed Sea Ice Extent - Northern Hemisphere (MASIE-NH) (all available satellite data at time of analysis), as this simplifies the comparisons for understanding outliers and differences amongst the datasets. As the algorithm was trained on the ESA CCI product, however it was essential to compare to a wider variety of datasets in order to fully understand the potential of the technique and to avoid overfitting to the training data. These datasets are described below for reference.

2.4.1 ESA CCI Sea Ice Concentration

Here we use the sea ice product from the The European Space Agency's Climate Change Initiative (ESA CCI) programme. This (*Toudal Pedersen et al.*, 2017) is derived from passive microwave measurements over both the North and South Poles at daily resolution. The passive radiometer used for the production of the data used in this study is the Advanced Microwave Scanning Radiometer-2 (AMSR2) on board GCOM-W1 and the processing of the data uses all 7 frequency channels (6.9 GHz, 7.3 GHz, 10.7 GHz, 18.7 GHz, 23.8 GHz, 36.5 GHz, 89.0 GHz). The 25 km version of this product was used as the 12.5 km product falls below the resolution of the sensor for most frequencies; with only 36.5 GHz and 89 GHz

channels within this scale (footprints 12 km x 7 km and 5 x 3 km respectively for along- and across-track). This product is provided in NetCDF format and linearly interpolated to the location of the TDS-1 sample points in order to provide co-located sea ice concentration data. These can be accessed in a variety of ways from http://cci.esa.int/data .

2.4.2 NSIDC Sea Ice Concentration

Sea Ice Concentration data were retrieved from the National Snow and Ice Data Centre (*Cavalieri et al.*, 1996). These are processed from Defence Meteorological Satellite Program (DMSP)-F17 Special Sensor Microwave Imager / Sounder (SSMIS) and are provided at daily resolution. There is a real-time version of this product, however due to the time period required, the higher processing level was available and used for comparisons. These are provided as binary files, on the 25 km x 25 km NSIDC polar stereographic grid for both Northern and Southern Hemispheres. These data are then linearly interpolated to the location of the TDS-1 sample points in order to provide co-located data. These can be downloaded from https://nsidc.org/data/NSIDC-0051/ .

2.4.3 OSI SAF Ice Edge

The OSI SAF ice edge product (*OSI SAF*, 2019a) is calculated from a combination of scatterometer and passive microwave sources. The active data comes from the Advanced Scatterometer (ASCAT) on Metop-A and Metop-B while the passive data are received by SSMIS onboard DMSP-F17 and -F18 as well as AMSR2, as with the ESA CCI data. These data are processed using Bayesian techniques to ascertain thresholds primarily in the scatterometer data to take advantage of the finer resolution, before further filtering using the passive microwave measurements. This product is provided in NetCDF at daily resolution, on a 25 km x 25 km grid in both hemispheres. The data provides surface classification (Unclassed, Closed Ice, Open Ice, Open Water). For this study, both closed ice and open ice are assigned "ice" and open water "sea". These data are interpolated through nearest neighbour to the location of the TDS-1 data points. These can be downloaded from http://

www.osi-saf.org/?q=content/global-sea-ice-edge-c .

2.4.4 MASIE Operational Ice Product

The MASIE-NH product is provided by the NSIDC in collaboration with the U.S. National Ice Service. This is an operational product, provided on a daily basis using the most recent satellite data obtained. As such it is calculated only in the Northern Hemisphere, and as it is designed to be used on the day of production, it is largely not reprocessed. It is provided as GeoTIFF or shapefiles either over the whole Arctic or by region. Here we use the entire Northern Hemisphere product on all days available, interpolated linearly to the location of the TDS-1 specular point locations. These can be downloaded from https://nsidc.org/data/masie/ .

2.5 Dataset agreement

The datasets detailed here for all chapters represent different sensors and wavelengths, and therefore represent different characteristics of the surfaces. Although they agree on large scale patterns and magnitudes, the measurements themselves differ according to the sensor, collection time period and algorithms applied. These allow the complementary techniques to inform on the data contained in the GNSS-R signal through its comparisons with these external sources in the following chapters. An overview of how these datasets compare to one another can be found below, when compared as interpolated to the locations of the TDS-1 specular points.

Table 2.1: Comparison of height measurements of the three Antarctic DEMs above at the locations of the TDS-1 specular points. Differences calculated as the top product minus the bottom product with heights in metres.

	CryoSat-2 - ERS-1 and ICESat	CryoSat-2 - Bedmap2	ERS-1 and ICESat - Bedmap2
Median difference (m)	0.67	1.70	0.83
Mean difference (m)	8.37	7.18	-1.31
RMS difference (m)	75.66	67.91	48.87

Table 2.2: Comparison of height measurements of the three Greenland DEMs above at the locations of the TDS-1 specular points. Heights in metres.

	ESA CCI - ERS-1 and GeoSat	ESA CCI - GIMP	ERS-1 and GeoSat - GIMP
Median difference (m)	1.52	0.19	-7.46
Mean difference (m)	0.67	1.61	-12.73
RMS difference (m)	83.92	43.66	73.32

Table 2.3: Comparison of ice extent agreement of the four products above at the locations of the TDS-1 specular points. Shown as percentage of points where datasets are in agreement.

	ESA CCI & NSIDC	ESA CCI & OSI SAF	NSIDC & OSI SAF	ESA CCI & MASIE	NSIDC & MASIE	OSI SAF & MASIE
Arctic	95.51%	97.41%	95.82%	95.63%	95.38%	97.35%
Antarctic	98.67%	97.71%	97.55%	-	-	-

Chapter 3

Independent DEM of Antarctica using GNSS-R data from TechDemoSat-1

Published as:

Cartwright, J., Clarizia, M. P., Cipollini, P., Banks, C. J., & Srokosz, M. (2018). Independent DEM of Antarctica using GNSS-R data from TechDemoSat-1. Geophysical Research Letters, 45, 6117– 6123. https://doi.org/10.1029/2018GL077429

Supporting information and typeset paper in Appendix A

Abstract

The first Digital Elevation Model (DEM) of the Antarctic Ice Sheet derived from Global Navigation Satellite Systems-Reflectometry (GNSS-R) data from the UK TechDemoSat-1 (TDS-1) satellite is presented. This is obtained using 32 months of data from the mission. This opportunistic and inexpensive method is shown to produce encouraging results from the technology demonstration platform of TechDemoSat-1 (TDS-1), with median bias under 18 metres and Root Mean Square Difference under 91 metres when compared to the CryoSat-2 1 km v1.0 Digital Elevation Model. Discrepancies between the two datasets are explored along with possible causes of such differences and potential improvements to further optimise this technique for future Global Navigation Satellite Systems-Reflectometry (GNSS-R) missions.

Plain Language Summary

Obtaining measurements of the Antarctic ice sheet is critical for understanding the effects that climate change might be having on it, and its potential future contribution to rising sea levels. The only practical way to do this is by using satellite data and this has been done successfully previously from the CryoSat-2 satellite, which carries a radar altimeter. However, due to its orbit it cannot measure an area near the South Pole. Here we demonstrate that measurements of the Antarctic ice sheet, including the vicinity of the South Pole, can be made by taking advantage of GPS signals that bounce of the ice sheet surface. The data are obtained from the UK's TechDemoSat-1 mission which carries a simple low-cost receiver to pick up the reflected GPS signals. The results from this demonstration mission (which was not designed to survey ice sheets) are promising, showing the potential of this approach for measuring the ice sheet in the future with a dedicated satellite mission.

3.1 Introduction and Rationale

Global Navigation Satellite Systems-Reflectometry (GNSS-R) was first proposed in 1988 (*Hall and Cordey*, 1988) and uses reflected L-Band radiation from Global Navigation Satellite Systems (GNSS) signals such as those of glsgps to characterise the Earth's surface. At present this is predominantly used for monitoring winds (*Clarizia and Ruf*, 2016; *Foti et al.*, 2015, 2017) and sea state (*Marchan-Hernandez et al.*, 2010). It is also being explored extensively for other Earth observation purposes such as soil moisture detection (*Masters et al.*, 2000), sea surface height (*Clarizia et al.*, 2016) and sea ice monitoring (*Gleason*, 2006; *Rivas et al.*, 2010).

Specific cryospheric applications of GNSS-R include the detection of sea ice (*Alonso-Arroyo et al.*, 2017; *Yan and Huang*, 2016), ice sheet altimetry (*Rius et al.*, 2017) and altimetry of sea ice through both the delay of the reflected echo (*Hu et al.*, 2017) and through its carrier phase delay (*Li et al.*, 2017). The use of GNSS-R for altimetry purposes was first proposed by Martín-Neira through a Passive Reflectometry and Interferometry System (*Martín-Neira*, 1993), and has been very

successful over a wide range of studies including fixed, air- and space-borne experiments. Initial airborne precisions measured include three metres over the sea (*Ruffini et al.*, 2004) and up to 5 cm over inland water bodies (*Lowe et al.*, 2002). Recently accuracies of 10-90 cm have been attained (*Semmling et al.*, 2013), and as such it can be seen as a very promising technique for the altimetry field. Due to the specular nature of reflections from ice and the necessity of satellite techniques to monitor these areas, it is a natural step to apply these methods to land-based ice sheets. As noted by *Slater et al.* (2018), accurate Digital Elevation Models (DEMs) can contribute to: the delineation of drainage basins; the estimation of grounding line ice thickness; mass balance calculations; boundary conditions for models of ice dynamics; as well as potential sea level rise.

L-Band signals were first shown to be sensitive to sub-metre ice elevation changes in 2004 (*Cardellach et al.*, 2004), but this level of accuracy depends on using the phase delay of a coherent signal (*Li et al.*, 2017) that is not applicable when the scattering is more diffuse. More recently GNSS-R signals have been proven to distinguish ocean, transition zone and glacial ice (*Rius et al.*, 2017). In their study, *Rius et al.* (2017) identified factors affecting the reflected signal and this study builds on that through the application of an algorithm previously used to measure sea surface height (*Clarizia et al.*, 2016). This algorithm is applied over the extent of the Antarctic Ice Sheet using all available data from the Low-Earth Orbiter TDS-1 and compared primarily with a DEM from ESA's CryoSat-2 (*Slater et al.*, 2018), as it is the most recent of the Antarctic DEM releases. Two earlier DEMs (*Bamber et al.*, 2009; *Fretwell et al.*, 2013) independent of the CryoSat-2 data are also used for a comparison.

This paper presents elevation estimates of the Antarctic Ice Sheet, the first application of GNSS-R to obtatin a DEM of Antarctica, by applying *Clarizia et al.* (2016)'s algorithm to TDS-1 data. Section 2 discusses the data used and the satellite platform, Section 3 summarises the methods used and results. Validation of the results against the CryoSat-2 1 km v1.0 DEM (*Slater et al.*, 2018) and other independent datasets is performed in Section 4, as well as discussing the necessary further investigations to improve the accuracy of this technique. The conclusions

of the study are given in Section 5.

3.2 TechDemoSat-1 and GNSS-R - Data

Data from GNSS-R sensors is provided in the form of delay-Doppler Maps (DDMs). A DDM can be seen as a map of the scattered power in the delay and Doppler domains. A smooth reflecting surface produces a strong, coherent reflection in GNSS-R. This means that the scattered power comes almost entirely from the specular point, and the glistening zone is very small. The corresponding DDMs will have a pronounced peak and a limited spreading of the power distribution. Ice is considered smooth compared to the sea surface at the scale of GPS L-Band wavelength (19 cm), giving particularly strong reflections in the DDMs and making them ideal for the extraction of height information, though land ice may give more diffuse reflections than sea ice. A strength of GNSS-R for applications such as these lies in the receipt of reflections from up to four different GPS satellites at any one time by the receiver. This, in addition to the asynchronism of the TDS-1 cycle with that of the GPS satellites, allows a varying web of specular points to be built up over time and therefore a high spatial resolution to be attained, as well as access to some points such as the poles, which due to necessary satellite inclination, have thus far not been possible to measure using satellite altimetry. However, this does introduce difficulties into the verification of measurements made at the highest latitudes, due to lack of independent validation data.

TDS-1 was designed as a satellite technology demonstration platform by Surrey Satellite Systems Ltd., carrying eight experimental payloads, of which one was the Space GNSS Receiver - Remote Sensing Instrument (SGR-ReSI) from which the data in this study were obtained. This instrument is extremely low-power and -mass and is constructed from commercial components. Full details can be found in *Jales and Unwin* (2015). TDS-1 was placed into a quasi-sun-synchronous orbit of 98.4 degrees inclination at an altitude of 635 km. Due to the use of a shared platform, the SGR-ReSI was active two days in an eight-day cycle. These data are provided as 1-second DDMs and metadata in 6-hour windows in a publicly accessible database (merrbys.co.uk). Each DDM is made up of 128 delay pixels by

20 Doppler pixels, with a resolution of 0.252 chips (0.246 microseconds) and 500 Hz respectively. The vertical resolution that results from this depends largely on the geometries of the satellites at the time (*Cardellach et al.*, 2014).

The data used in this study have been taken from 3 years of service from TDS-1 (November 2014 - July 2017) with specular points South of 60°S and filtered in order to eliminate noise. This has been achieved by excluding points where the power distribution of the DDM is less coherent than a normal distribution using the kurtosis of the DDM. DDMs with a kurtosis much greater than 3 (the value for a Gaussian distribution) display a clear signal. The threshold for discarding DDMs was fixed to be a kurtosis of 3.5. This threshold was chosen so as to ensure the removal of all noisy points below the threshold, and to account for the uncertainty in the noise estimation. Increasing the threshold to 4 made little difference to the results and therefore the lower threshold was used in order to return more data. Further points were removed according to quality flags provided with the data.

Being a technology demonstration mission, the sensor on-board TDS-1 is not optimised for altimetric applications. As such, the tracking window for received signals is tied to the ellipsoid, which causes loss of signal where high elevations such as those of the Antarctic Ice Sheet are concerned. These data points have been identified by the maximum amplitude of the DDM straying from the central four Doppler bins of the DDM (as the central peak is out of the tracking window). These have been filtered out where the Doppler value at the maximum amplitude (dop_{ma}) is outside the range:

$$\frac{dop_{min}}{10} < dop_{ma} < \frac{dop_{max}}{10} \tag{3.1}$$

where dop_{min} is the minimum of the Doppler axis and dop_{max} the maximum. These criteria were chosen as they remove all data points where the signal has left the tracking window and prevents saturation at the top of the tracking window (often above about 2400 metres elevation). Further data omitted are those where the maximum amplitude is in the first delay row of the DDM, as no leading edge is visible in the waveform. Data that are flagged as containing the Direct Signal in the DDM are removed due to disruption of the tracking of the reflected signal, and

those in Collection Period 12 (September 2016) are also filtered due to changes in the DDM processor settings that made these DDMs inconsistent.

The data used include both modes of gain control, as the power of the signal itself is not used in the height estimation. Contrary to previous studies, samples were not filtered by antenna gain, but an incidence angle filter was applied to remove points where reflections were at an incidence angle of 55° or greater. The data collected at larger angles were seen to overestimate heights by up to 200 metres near the pole. The inclusion of these data yields an almost gap-free DEM, though this is not presented in this paper due to the largely unconstrained overestimations. The extended DEM and comparisons with CryoSat-2 data are provided in Appendix A.

The most recent release (May 2018) of the CryoSat-2 DEM (*Slater et al.*, 2018) is used as a comparison to ensure the highest accuracy of control variable for comparison.

3.3 GNSS-R Altimetry of Antarctic continental ice - Methods and Results

The elevation algorithm of *Clarizia et al.* (2016) uses the locations of both the transmitter and receiver satellites from the TDS-1 metadata to estimate height through the time delay between the expected receipt of the signal (were it to reflect off the ellipsoid) and the actual time of receipt. The geometry then allows the calculation of the reflective surface above the ellipsoid. In order to extract this delay from the TDS-1 DDMs, the maximum power is tracked in the Doppler domain to identify the waveform as it varies in delay space (the column of the DDM that corresponds to the maximum power). The sampling is increased in the delay domain through Fourier Transform Interpolation of this waveform, at an interpolation factor of 1000 (*Clarizia et al.*, 2016) before the maximum first-order derivative of the leading edge is identified. This interpolation method is used in order to preserve the spectrum in the frequency domain throughout the interpolation process and has been seen to reduce the errors. The method to identify the leading edge derivative follows the process outlined in *Hajj and Zuffada*

(2003), whereby the first order derivative is calculated for the leading edge of the waveform and the maximum of this is used to represent the delay between the direct and reflected signal. This delay value is then used for elevation calculations based on the geometry of the bistatic arrangement (as found in *Clarizia et al.* (2016)). Details of the measurement geometry and delay estimation can be found in Appendix A, as can a discussion of tracking maximum power instead of the leading edge to obtain height estimates.

After filtering, a significant number of samples were found to have values less than zero relative to the ellipsoid and were simply discarded. The remaining data are averaged over a 50 x 50 km grid for comparison to the CryoSat-2 DEM 1 km v1.0 (*Slater et al.*, 2018) as reference. For these comparisons, the CryoSat-2 DEM was filtered for negative samples and gridded in the same manner to ensure comparability of measurements (Figures 3.1 and 3.2). This resolution was chosen so as to maximise both coverage and accuracy of the final product. Varying this resolution between 20 km and 100 km gave no obvious improvement to the results (see Appendix A). For calculation of Root Mean Square and median differences quoted below, co-located ungridded data were used through linear interpolation of the CryoSat-2 DEM to the locations of the TDS-1 specular points. This gives the noisier appearance seen in the CryoSat-2 data in Figure 3.3.

3.4 Comparison with CryoSat-2 Data - Discussion

The DEM presented in Figure 3.1 suggests that the use of GNSS-R for altimetry over land ice is feasible and increases the potential for height measurements over the pole which is currently not estimated with any existing satellite (see Appendix A). The comparison of this with the CryoSat-2 DEM 1 km v1.0 (Figures 3.2 and 3.3) gives an insight into the accuracy of this technique, yielding median error of 17.9 metres and an RMS error of 90.7 metres over the extent of the ice sheet. This error is fairly consistent with other available DEMs for comparison, as detailed in Table 3.1. The slope of the ice surface, derived from the CryoSat-2 DEM, results in changes in the error with a median and RMS error respectively of 13.8 m and

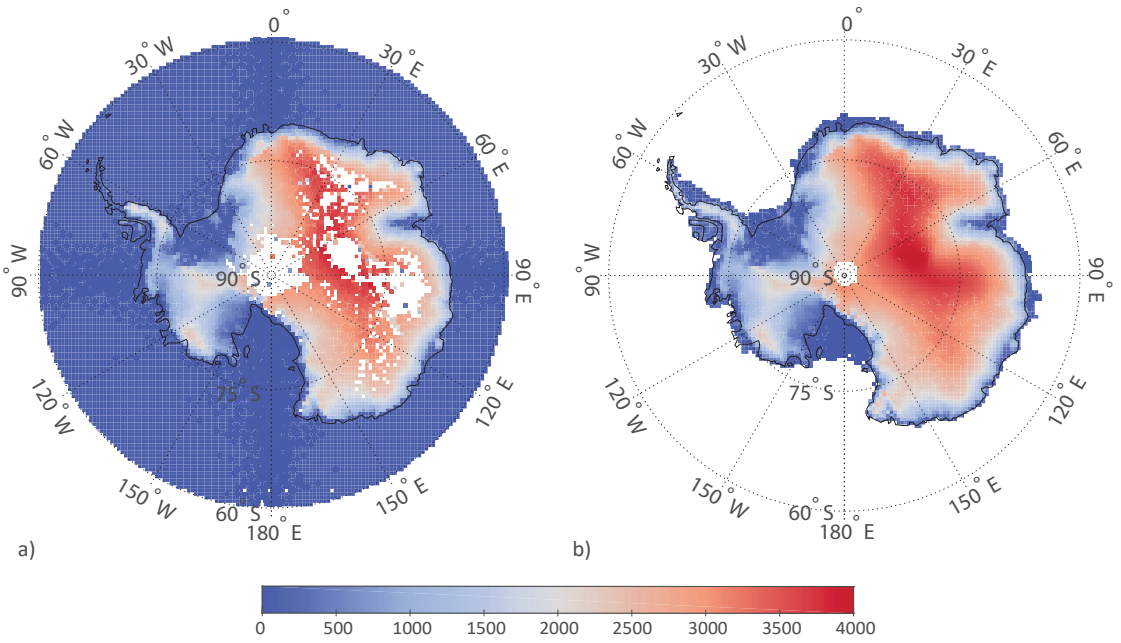

Figure 3.1: Digital Elevation Models from a) TDS-1 data and b) CryoSat-2 (*Slater et al.*, 2018). Elevations are shown in metres above the ellipsoid with white denoting no available data.

68.1 m for slopes below 0.25° to 37.9 m and 96.8 m for slopes between 0.75° and 1°. Further error estimates due to the slope of the ice surface and comparisons with the Bedmap2 and *Bamber et al.* (2009) DEMs can be found in Appendix A.

Rius et al. (2017) in their study of Greenland along two tracks quote 8.5 m as the 'expected uncertainty in the delay measurements', but this is not an actual error estimate obtained by comparing GNSS-R measurements with independent observations. More comparable are the results of *Slater et al.* (2018), *Griggs and Bamber* (2009) and *Fretwell et al.* (2013) who quote overall RMS errors of 13.5 m, 5.0 m and 30.0 m respectively for their Antarctic DEMs. However, in areas where the DEM has been interpolated, *Slater et al.* (2018) state that there are median and RMS differences of 19.62 m and 117.77 m respectively, as compared to airborne data. The latter figures are not dissimilar to the ones obtained here.

Due to the nature of the platform as a demonstrator and the operating cycle of the SGR-ReSi, the DEM (Figure 3.1) is not complete, with many holes resulting from areas without suitable data within the period of TDS-1 data used here. Where data acquired at higher incidence angles are included, the majority of these gaps

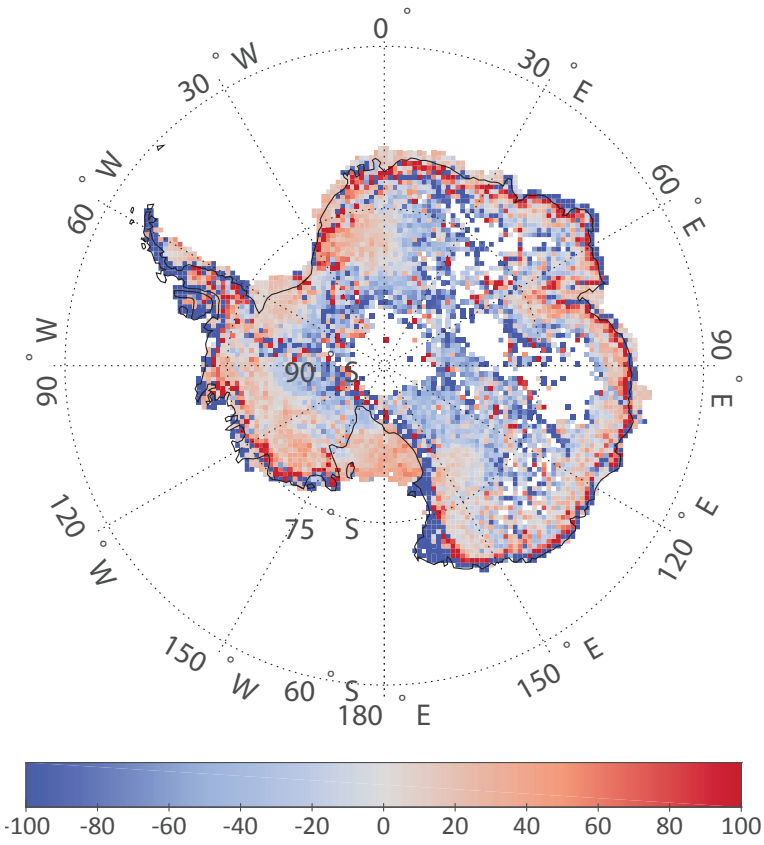

Figure 3.2: Comparison of TDS-1 heights in metres over Antarctica and those from CryoSat-2 data (*Slater et al.*, 2018). (TDS-1 minus CryoSat-2)

Table 3.1: Comparison with other available DEMs. *Bamber et al.* (2009) and Bedmap2 (*Fretwell et al.*, 2013) are independent from the CryoSat-2 DEM, the former based on data from ERS-1 and ICESat, and the latter a compilation of many DEMs (including that of *Bamber et al.* (2009)). The DEMs used in this comparison all use kriging or other interpolation technique and where this has been used to fill in the area around the pole where there is no data those estimates have been omitted from this comparison.

DEM	Reference	Median difference (m)	RMS difference (m)
CryoSat-2 1 km	*Slater et al.* (2018)	17.9445	90.6924
ERS-1 and ICESat	*Bamber et al.* (2009)	18.7009	79.8821
Bedmap2 Surface DEM	*Fretwell et al.* (2013)	19.2476	83.0065

disappear, but some points are overestimated (see Appendix A). The density plot (Figure 3.4) also displays a large number of points underestimated at around the origin within the TDS-1 dataset in relation to CryoSat-2. These correspond to data retrieved from the edge of the ice shelf (values of -100 m in Figure 3.2) and may

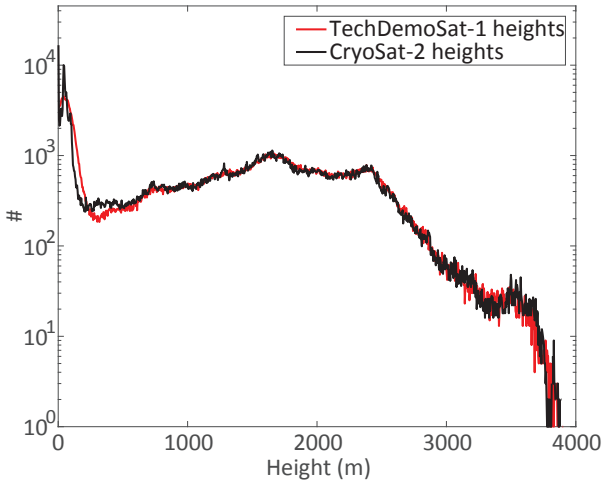

Figure 3.3: Histogram of co-located height data over Antarctica from CryoSat-2 (black) (*Slater et al.*, 2018) and TDS-1 (red).

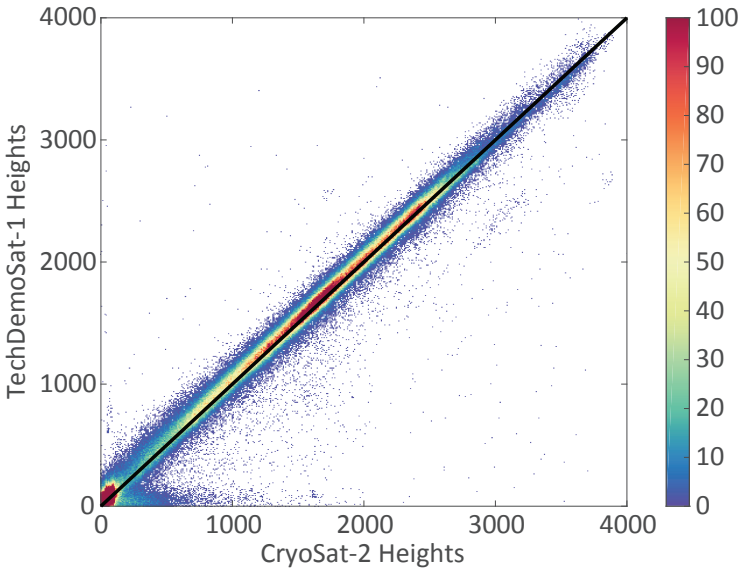

Figure 3.4: Density plot comparing height estimations from TDS-1 over Antarctica and co-located data from CryoSat-2 DEM (*Slater et al.*, 2018) with 1:1 reference line (black).

be due to corner effects giving multiple DDM peaks or misplaced specular points.

Known issues in the TDS-1 dataset are covered in detail in *Clarizia et al.* (2016) and include uncertainty of the satellite attitude and orbit (and thus the specular point), as well as experimental changes in settings given its use as a technology demonstration platform. Attitude is provided by both the sun sensors and the magnetometers, with the latter in use when the satellite is in eclipse. The uncertainty in the magnetometer readings is larger than those of the sun sensors (up to 10 degrees (*Foti et al.*, 2017)). Sudden large corrections can also occur when switching between the two sensors, though no correlation has been seen between these changes and error patterns seen here. One important change in the sensor settings through the mission is that of the switch from Automatic Gain Mode to Fixed Gain Mode (April 2015), resulting in a change in the absolute power seen in the DDM. This is also affected by antenna effects which (despite much progress (*Gleason et al.*, 2016; *Voronovich and Zavorotny*, 2018)) are not yet definitively quantified for this sensor. A strength of this elevation estimation algorithm is that the absolute power of the DDM cells is not considered, making it possible to use data from both modes without calibration of the two or normalisation of the DDMs.

A large unknown in L-Band altimetry is the penetration depth of the signal into materials such as snow and ice. This can vary in magnitude from 10s of centimetres to 100s of metres (*Li et al.*, 2017; *Mätzler*, 2001) and is due to the large range of physical properties of these materials with changing densities and precipitation regime. For example, *Rignot et al.* (2001) measured penetration depths of 3m to 120m over the Greenland ice sheet, depending on the terrain. A further consideration is the atmospheric uncertainties associated with the ionosphere and troposphere above the polar ice cap. These are largely unknown at these high latitudes but are thought to be much smaller than our magnitude of error (maximum of 10 metres at the equator) (*Hoque and Jakowski*, 2012).

Errors are also associated with the averaging period used for both the TDS-1 data and that of the CryoSat-2 DEM. Due to the temporal extent involved in the calculations, smaller scale effects such as seasonality were explored but no correlation was found with discrepancies from the CryoSat-2 DEM. As such, these seasonal

effects and their associated changes in penetration depth have been ignored.

3.5 Conclusions

We have demonstrated through this study that altimetry of land ice is possible with GNSS-R to an accuracy of approximately 18 metres, if CryoSat-2 is assumed to be truth. This is the first time that GNSS-R has been used to create an independent DEM over land ice, and has potential significance as data collected covers the pole area which until now was not possible to map with satellite altimetry.

The use of the technology demonstration platform to produce these results reveal great potential for the future of this technique, as further increases in accuracy and understanding may be achieved using a sensor and platform optimised for such measurements. In future studies it will be necessary to understand and mitigate errors such as those causing the over-estimation of points at high incidence angles. This will enable this technique to produce a full DEM of the Antarctic Ice Sheet with improved accuracy and coverage, including the South Pole. It will also be necessary to optimise any platform and sensor for such measurements, and to improve processing strategies, such as centering the delay-Doppler window around the true specular point on the Earth surface to ensure all data is received within the tracking window. In order to improve the estimation of the surface elevation, modelling of the signal scattering and penetration through the ice will be necessary, with the objective of quantifying the penetration depth under different conditions, and its variations due to seasons and climate.

Owing to the reliance of the technique on signals of opportunity and the light-weight nature of the receiver, the harnessing of this technology for the monitoring of the cryosphere would provide an inexpensive yet highly effective solution. The recent launch of the CYGNSS constellation in 2016 for the application of GNSS-R to tropical wind measurements brings up the possibility of a polar mission of a similar format. Reflections over ice are much more coherent, and therefore stronger than those over oceans. The application of this technology to such a mission would therefore provide much higher spatio-temporal resolution of measurements in polar

regions (average 4 hour revisit time for CYGNSS satellites (*Ruf et al.*, 2013)), allowing improved monitoring of all aspects of this dynamic system, including sea-ice interactions (which have not been considered here). To determine the feasibility of such a mission would require a careful consideration of the error budget to determine the accuracy of the height measurements possible, but this is beyond the scope of this paper. In addition, further improvements to measurement accuracy may be possible using interferometric techniques (*Martin-Neira et al.*, 2011) or phase delay information (*Cardellach et al.*, 2004; *Li et al.*, 2017), but the latter depends on having a coherent return from the surface.

In terms of the future applications of GNSS-R to monitoring the Antarctic ice sheet, it may be possible to deduce properties of Antarctic snow and ice by combining these observations with those from passive L-band instruments, such as Soil Moisture and Ocean Salinity (SMOS) (e.g. *Macelloni et al.* (2016)), and at other microwave frequencies, such as K_u-band from Cryosat-2.

Chapter Summary

This chapter has demonstrated the application of algorithms, previously used for the determination of the sea surface height, to the GNSS-R data south of 60°S in order to estimate the height of the glacial ice in Antarctica. This fulfils Aim 1 and shows the potential to utilise these signals to understand the surface mass balance of the Antarctic Ice Sheet. Comparisons with multiple 'truth' DEM products allows the discussion of unknowns in the application of the technique, such as the penetration depth of the signal into snow and glacial ice, and atmospheric uncertainties affecting the signal. Chapter 4 will improve upon this technique and extend its application to Greenland.

Chapter 4

Improved GNSS-R bi-static altimetry and independent DEMs of Greenland and Antarctica from TechDemoSat-1

Published as:

Cartwright, J., Banks, C. J., & Srokosz, M.: Improved GNSS-R bi-static altimetry and independent digital elevation models of Greenland and Antarctica from TechDemoSat-1, The Cryosphere, 14, 1909–1917, https://doi.org/10.5194/tc-14-1909-2020, 2020.

Supporting information and typeset paper in Appendix B

Abstract

Digital Elevation Models (DEMs) of the Antarctic and Greenland Ice Sheets are presented, derived from Global Navigation Satellite Systems-Reflectometry (GNSS-R). This builds on a previous study (Cartwright et al., 2018) using Global Navigation Satellite Systems-Reflectometry (GNSS-R) to derive an Antarctic DEM but uses improved processing and an additional 13 months of measurements, totalling 46 months of data from the UK TechDemoSat-1 satellite. A median bias of under 10 m and root-mean-square (RMS) errors of under 53 m for the Antarctic and 166 m for Greenland are obtained, as compared to existing DEMs. The results represent, compared to the earlier study, a halving of the median bias to 9 m, an improvement in coverage of 18%, and a four times higher spatial resolution (now

gridded at 25 km). In addition, these are the first published satellite altimetry measurements of the region surrounding the South Pole. Comparisons south of 88°S yield RMS errors of less than 33 m when compared to NASA's Operation IceBridge measurements. Differences between DEMs are explored, the limitations of the technique noted and the future potential of GNSS-R for glacial ice studies discussed.

Short Summary

This study uses reflected GPS signals to measure ice at the South Pole itself for the first time. These measurements are essential to understand the interaction of the ice with the Earth's physical systems. Orbital constraints mean that satellites are usually unable to measure in the vicinity of the South Pole itself. This is overcome here by using data obtained by UK TechDemoSat-1. Data are processed to obtain the height of glacial ice across the Greenland and Antarctic ice sheets.

4.1 Introduction

The use of reflected L-Band signals from Global Navigation Satellite Systems (GNSS) for Earth observational purposes was first proposed in 1988 (*Hall and Cordey*, 1988). GNSS-R is now applied to the characterisation of the Earth's surface predominately for the monitoring of ocean surface winds (*Clarizia and Ruf*, 2016; *Foti et al.*, 2015, 2017; *Ruf and Balasubramaniam*, 2019). It has been investigated for other applications such as altimetry of the ice sheets and oceans (eg. *Cardellach et al.* (2004); *Cartwright et al.* (2018); *Clarizia et al.* (2016), soil moisture (*Chew et al.*, 2016) and monitoring of the cryosphere (eg. *Cartwright et al.* (2019); *Fabra et al.* (2012); *Rivas et al.* (2010)). GNSS-R has been found to be effective when applied to the cryosphere not only for sea ice detection (*Alonso-Arroyo et al.*, 2017; *Cartwright et al.*, 2019; *Yan and Huang*, 2016) and characterisation (*Rodriguez-Alvarez et al.*, 2019) but also for sea ice altimetry (*Hu et al.*, 2017; *Li et al.*, 2017) and glacial ice altimetry (*Cartwright et al.*, 2018; *Rius et al.*, 2017).

The application of GNSS-R to altimetry was originally proposed by (*Martín-Neira*, 1993) and has been successfully demonstrated from fixed, airborne and spaceborne platforms. Due to the highly specular nature of reflections from ice-covered surfaces, it is a natural step to apply these techniques to the cryosphere. In these cases, spaceborne platforms have been able to achieve root-mean-square (RMS) errors of below 5 m when applied to limited tracks using the group delay (*Hu et al.*, 2017) and below 5 cm where phase delay is available (*Li et al.*, 2017). As more GNSS-R data have become available from the Low Earth Orbiter TechDemoSat-1 (TDS-1), it has been possible to use a larger collection of reflections for the construction of DEMs of the larger ice sheets, such as Antarctica (*Cartwright et al.*, 2018). The use of GNSS-R offers a unique opportunity to measure the elevation of ice over the South Pole due to the wide variety of incidence angles available through bi-static altimetry enabling this technique to be unrestricted by the orbital constraints of traditional mono-static radar altimetry.

The use of signals of opportunity results in GNSS-R requiring only very low-mass, low-power receiver only systems and is therefore a low-cost method of remote sensing. The approach therefore lends itself to applications in constellation missions in order to increase spatial and temporal resolutions. Cyclone GNSS (CYGNSS) was launched in 2016 by NASA for the monitoring of winds inside tropical cyclones, and has an average revisit time of 4 hours (*Ruf et al.*, 2013), however, the low inclination of these satellites (35°) means that their data have little application to the cryosphere. A system similar to that of CYGNSS, but optimised for cryosphere applications, has been proposed (*Cardellach et al.*, 2018). Currently available spaceborne data over the poles is limited to that of satellite TDS-1, which was placed in a high-inclination orbit (98.4°) and active for a total of 46 months between November 2014 and December 2018. It is these data on which this study is based.

As stated by *Slater et al.* (2018), DEMs can help in the understanding of ice sheet hydrology through mass balance calculations, grounding line thickness, and delineation of drainage basins. These further improve understanding of ice dynamics and potential sea level rise associated with ice sheets. This paper builds upon earlier

work done by Cartwright et al. (2018), using an algorithm developed by *Clarizia et al.* (2016) for the estimation of sea surface height. Here we use improved retracking combined with expansion of the GNSS-R dataset and enhanced processing to yield higher accuracies over the Antarctic Ice Sheet. This is then applied to the Greenland Ice Sheet, demonstrating the flexibility of the technique and potential for high resolution observations over these areas. These new DEMs are primarily compared with two high resolution DEMs, exclusively from CryoSat-2 in the case of the Antarctic Ice Sheet (*Slater et al.*, 2018) and from the European Space Agency Climate Change Initiative's (ESA CCI) composite of CryoSat-2 (*Simonsen and Sørensen*, 2017) and ArcticDEM (`https://www.pgc.umn.edu/data/arcticdem`) in the case of Greenland. Brief comparisons are given to two additional DEMs for each ice sheet; these are those by *Howat et al.* (2014) and *Bamber* (2001) over Greenland and the Bedmap2 Elevation Data (*Fretwell et al.*, 2013) and *Bamber et al.* (2009) over Antarctica. Further comparisons are performed over the area south of 88° using the Operation IceBridge elevation dataset.

Cartwright et al. (2018) found this approach gave consistent DEM overestimations in data at higher incidence angles, therefore high incidence angle data (>55°) were discarded. In this study, we remove the incidence angle filter to increase the sample size and add an intermediate processing step, a spatial mean of all points within a certain radius of the point in question. This accounts for the overestimations of the higher incidence angle data, leading to an overall reduction in error and increase in resolution due to the larger dataset.

This paper will first describe the dataset used and the satellite platform TDS-1 in section 2. Then section 3 will detail the improved methods for height estimation and application over both Antarctica and Greenland. Comparison of the new DEMs against the CryoSat-2 and European Space Agency (ESA) Climate Change Initiative (CCI) DEMs are reported in section 4, along with investigations into the areas in which they differ, possible causes of these differences and brief comparisons with other DEMs. Section 5 details the benefits and limitations of this technique. Finally, section 6 concludes the study.

4.2 TechDemoSat-1 and Datasets used

TDS-1 was launched in 2014 as a technology demonstration platform by Surrey Satellite Technology Ltd. into a quasi sun-synchoronous orbit of 98.4°inclination at an altitude of 635 km. TDS-1 carried eight experimental payloads, one of which was the Space GNSS Receiver - Remote Sensing Instrument (SGR-ReSI). It is this sensor from which the data used in this study were acquired. SGR-ReSI is extremely low-mass and -power and constructed from commercial off-the-shelf components. Full details of the SGR-ReSI can be found in *Jales and Unwin* (2015). Due to the use of the shared platform in the demonstration operation period (November 2014-July 2017) the SGR-ReSI was only active 2 days in every 8-day cycle whereas it was operating 24-hours in the final phase of the mission (August 2017–December 2018). The instrument could receive up to 4 GPS (Global Positioning System) reflections at any one time. This, combined with the asynchronism of the cycle of TDS-1 with that of the GPS satellites, creates a varying web of specular points over time, increasing the spatial coverage, as well as providing data over the poles, which has thus far not been possible with standard satellite altimetry due to orbital constraints.

Data from TDS-1 are provided as delay-Doppler maps (DDMs) which are maps of the scattered power in the delay and Doppler domains. A smooth reflecting surface results in a strong, coherent signal due to the majority of the power originating from the specular point, with a relatively small glistening zone *Zavorotny and Voronovich* (2000). Such DDMs have a distinct peak in power and very little spreading of the power in the delay or Doppler domain. This is in contrast to rougher reflections (for example, over the ocean surface) where a pronounced horse-shoe shape is visible due to the spread of the signal in both delay and Doppler caused by signal scatter both in front and behind the specular point. At the wavelength of the GPS signals used (L1-Band, $\sim$ 19 cm), ice is much smoother than the ocean surface. The strength of this return from ice is ideal for the extraction of height information. DDMs were collected every millisecond and subject to onboard incoherent averaging, producing 1-second DDMs and metadata in 6-hour windows. These data are provided in a publicly accessible database (`www.merrbys.co.uk`).

Each DDM is composed of 128 delay pixels by 20 Doppler pixels, with respective resolutions of 0.252 chips (0.246 µs) and 500 Hz, offering a vertical resolution of 37 m prior to increases in precision through waveform interpolation to 1000 times the resolution. The vertical resolution that this produces varies largely depending on the geometries of the GPS satellites and TDS-1 at the time of transmission and receipt.

The data used in this study were taken from the entirety of the TDS-1 mission (November 2014 to December 2018). This incorporates the initial demonstration mission period (until July 2017) and the extension period (October 2017 to end of 2018). During the extension period, although the SGR-ReSI was in constant operation, it downlinked only data over 0 dB in gain. This results in a lack of data over the highest latitudes, and produces a bias in sample number over Greenland when compared to Antarctica. Data South of 60°is selected for the Antarctic DEM, and for Greenland data North of 58°N and between -10°to -75°E. The data were filtered following *Cartwright et al.* (2018), with the exception of the incidence angle filter, as previously detailed. This ensured the elimination of noise, as well as the removal of DDMs where the return lies out of the tracking window, and those data affected by instrument setting changes.

The most recent version of the CryoSat-2 DEM (*Slater et al.*, 2018) was used as a primary comparison for the Antarctic data, whilst the ESA CCI Greenland Ice Sheet product (hereafter referred to as GL-CCI) was used for validation of the Greenland product. GL-CCI is a composite of ArcticDEM (`https://www.pgc.umn.edu/data/arcticdem`) and CryoSat-2 measurements (*Simonsen and Sørensen*, 2017). Two other DEMs for each region have been used for brief comparison, and for full details of these, readers should see the referenced work. In order to allow comparison of the Antarctic DEM south of 88° S, data from Operation IceBridge have been employed, downloaded from the National Snow and Ice Data Centre (Dataset ID ILATM1B, `https://nsidc.org/data/ILATM1B/`).

4.3 Improved GNSS-R bi-static altimetry

The algorithm of *Clarizia et al.* (2016) uses the geometry of the receiver and transmitter satellite locations to estimate the height of the surface above the reference ellipsoid using the time delay between when the reflected signal is expected (modelled as reflecting off the ellipsoid) and the time of receipt by TDS-1. This delay is estimated from the delay waveform obtained from the DDM at the value of the Doppler that corresponds to the maximum power in the DDM. The waveform is then Fourier transform interpolated such that the sample rate is increased by a factor of 1,000 whilst retaining the original spectrum of the waveform. Previous studies (*Cartwright et al.*, 2018; *Clarizia et al.*, 2016) have used the maximum derivative of the leading edge of the waveform as outlined by *Hajj and Zuffada* (2003), however, more recent studies have determined that the leading edge at 70% of the maximum power more directly corresponds to the specular point on the surface (*Cardellach et al.*, 2014; *Mashburn et al.*, 2016). As such it is this delay used in this study ("p70" algorithm), leading to a decrease in error over Antarctica as compared to the original study by *Cartwright et al.* (2018).

A spatial averaging is applied in order to incorporate higher incidence angle points previously discarded due to the application of an incidence angle filter. This maintains the quality of the data whilst providing data over the region around the South Pole by taking a mean of all heights within 25 km of each specular point. A mean was used as the simplest approach, with weighted means and median explored, but providing no improvement in accuracy. These spatial averages comprise the scattered data for gridding and comparison of interpolated DEM data. The data were then averaged onto a regular 25 km x 25 km grid. This grid is four times finer (higher resolution) than that used by Cartwright et al. (2018) due to the increase in the number of observations from incorporating higher incidence angle data and the additional observations from the mission extension of TDS-1. Grid resolutions of 5 km, 10 km and 50 km were also investigated, however 25 km was chosen so as to maximise both the resolution of the DEM and coverage in both hemispheres. This was also used as the radius for the spatial mean described above in order to ensure consistency. These same methods were then applied to

the data over the Greenland study area in order to obtain a DEM of the Greenland Ice Sheet.

Differences were calculated from both the gridded products and the scattered points. For the former, the comparison DEMs are re-gridded to the same grid, before subtracting the comparison data from the TDS-1 estimates. In order to compare the scattered data, the comparison DEMs are interpolated linearly to the locations of the TDS-1 specular points before subtraction from the TDS-1 estimates. Antarctic data is also compared through the use of the IceBridge dataset, whereby the TDS-1 DEM is linearly interpolated to the location of the IceBridge data points.

Table 4.1: Comparison of sample numbers and total DEM data coverage (as percentage of glacial ice area with elevation estimates) with different filters and datasets for both Greenland and Antarctica. Heights are calculated using the p70 algorithm and gridded at 25 km.

	Antarctica		Greenland	
	n	% coverage	n	% coverage
Filters: *Cartwright et al.* (2018)				
Dataset: Oct 2014 - July 2017	1,735,766	74.8	455,746	99.5
Filters: This study				
Dataset: Oct 2014- July 2017	1,954,909	90.9	540,080	99.7
Filters: This study				
Dataset: Oct 2014- December 2018	4,223,821	92.8	1,050,486	99.9

Over Antarctica, the methods used here give coverage of an additional 18% of Antarctica's glacial ice area (Table 4.1) and a decrease of 45% (9 m) in interpolated median error to 10.4 m, as shown in Table 2, when compared to *Cartwright et al.* (2018). The RMS error of the DEM (gridded error) shows a decrease of 115 m, as shown in Table 3. This recalculated DEM can be seen in Figure 4.1. Comparisons of data south of 88°S with available Operation IceBridge (*Studinger*, 2013) data yields RMS errors of less than 33 m (Table 4.4).

Table 4.2: Comparison of interpolated error using method of *Cartwright et al.* (2018) and those presented in this study, both for Antarctica and Greenland, applied across the entire dataset of TDS-1, data between October 2014 and December 2018. The TDS-1 Antarctic DEM (top) is compared with CryoSat-2 v1 1 km DEM (*Slater et al.*, 2018), DEM by *Bamber et al.* (2009) and the surface elevation data from Bedmap-2 (*Fretwell et al.*, 2013). The Greenland DEM (bottom) is compared with the GL-CCI, *Bamber* (2001); *Howat et al.* (2014).

	Antarctica			
	Cartwright et al. (2018) method	This Study		
	CryoSat-2	CryoSat-2	Bamber	Bedmap-2
Median difference (m)	19.01	10.40	10.95	10.40
Mean difference (m)	15.23	11.63	11.55	11.63
RMS difference (m)	91.00	52.39	56.56	52.39
	Greenland			
	Cartwright et al. (2018) method	This Study		
	GL-CCI	GL-CCI	Bamber	Howat
Median difference (m)	17.35	9.62	48.84	26.91
Mean difference (m)	-15.26	-19.85	23.46	9.03
RMS difference (m)	210.15	165.73	124.24	128.88

4.4 Comparison against CryoSat-2 and GL-CCI

As presented in Figure 4.1, altimetry using GNSS-R is feasible over glacial ice and is capable of giving measurements over the South Pole itself, which is as yet unavailable for measurement with existing satellite altimetry techniques. Interpolated and gridded errors when compared to other DEMs are presented in Table 4.2 and Table 4.3 respectively. The DEM product results in a median difference over Antarctica of 40 cm in comparison to the most recent version of the CryoSat-2 DEM and under 6 m over Greenland when compared to GL-CCI (Table 4.3). This higher error over Greenland is to be expected considering the higher ratio of steep coastline to inland ice sheet as higher inclinations have been found to be associated with increased error, in agreement with (*Cartwright et al.*, 2018). Data on slope effects can be found in Appendix B. This is in part due to corner reflection effects giving multiple DDM peaks and to error in the estimation of the specular point location, with surface slope not accounted for in the location calculation, as it is largely dependent of the roughness of the reflecting surface and its alignment with

Table 4.3: Comparison of gridded error using method of *Cartwright et al.* (2018) and those presented in this study, both for Antarctica and Greenland, applied across the entire dataset of TDS-1, data between October 2014 and December 2018. The TDS-1 Antarctic DEM (top) is compared with CryoSat-2 v1 1 km DEM (*Slater et al.*, 2018), DEM by *Bamber et al.* (2009) and the surface elevation data from Bedmap-2 (*Fretwell et al.*, 2013). The Greenland DEM (bottom) is compared with the GL-CCI, *Bamber* (2001); *Howat et al.* (2014)

.

	Antarctica			
	Cartwright et al. (2018) method	This Study		
	CryoSat-2	CryoSat-2	Bamber	Bedmap-2
Median difference (m)	-1.20	0.40	1.05	2.98
Mean difference (m)	-67.26	-24.39	-13.20	-13.34
RMS difference (m)	273.42	158.62	123.57	132.39
	Greenland			
	Cartwright et al. (2018) method	This Study		
	GL-CCI	GL-CCI	Bamber	Howat
Median difference (m)	-6.18	-5.77	52.73	16.90
Mean difference (m)	-128.39	-95.88	-2.31	-18.96
RMS difference (m)	322.35	274.38	215.29	205.57

Table 4.4: Comparison of error with Operation IceBridge elevation estimates, (*Studinger*, 2013). N=2,841,200,289 and N=3,889,345 respectively for continent-wide comparisons and those greater than 88°S

	Antarctica	
	whole	>88°S
Median difference (m)	29.27	-19.55
Mean difference (m)	15.33	-15.85
RMS difference (m)	135.70	32.89

the look angle of the satellite. In addition, in Greenland the higher error in these regions may be due to the high slopes of the coastal terrain resulting in rocky outcrops, rather than glacial ice. In this respect it may be considered similar to the Antarctic Peninsula, and the errors are comparable. These patterns can be seen in Figure 4.2 with higher errors around the coastlines and in the more mountainous regions of the ice sheet interiors. These points account for the majority of the underestimations appearing near the origin in Figure 4.3 and are a source of discrepancies between the comparison DEMs themselves, especially where Greenland

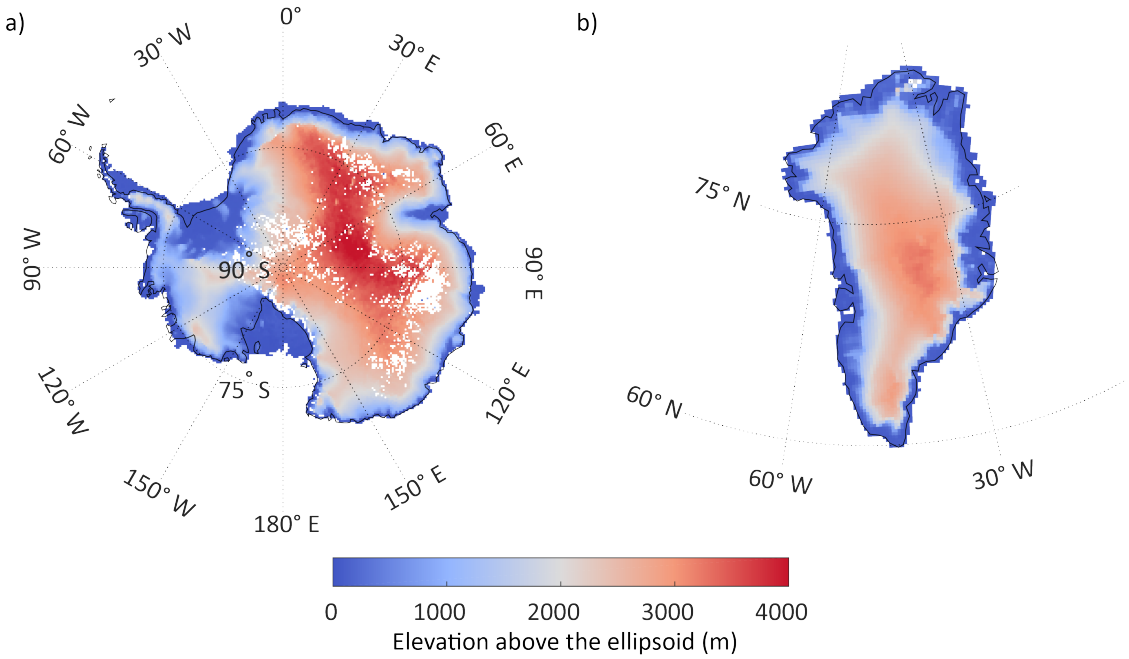

Figure 4.1: Digital Elevation models for a) Antarctic and b) Greenland Ice Sheets. Elevations shown are meters above the ellipsoid with white denoting no available data. Gridding in 25 km cells, coastlines black.

is concerned. It is these areas that give the large error ranges seen in Figure 4.2 and 4.3.

Comparisons with IceBridge data south of 88°were somewhat limited due to the remoteness of the location for surveying. However, the results show RMS errors of less than 33 m. When compared across the full extent of the Antarctic ice sheet, this increases to 136 m, primarily due to the inclusion of steeply sloping ice sheet margins (Table 4.4).

When gridded at finer resolutions, accuracy of the resultant DEM increases, however this results in a reduction in the spatial coverage. This suggests that reflections are from a small area and are in agreement with theory that states that the footprint of the SGR-ReSI should be small, at approximately 6 km along-track by 0.4 km across track over sea ice (*Alonso-Arroyo et al.*, 2017). Whilst reflections from glacial ice are expected to be less coherent and therefore produce a larger footprint, it is still expected to be less than the grid cell size used. Due to the nature of the platform as a demonstration mission, and the design of the system for other measurements, it is necessary to grid the DEMs at this low resolution so as to avoid too many gaps in the data. However, it is promising for future

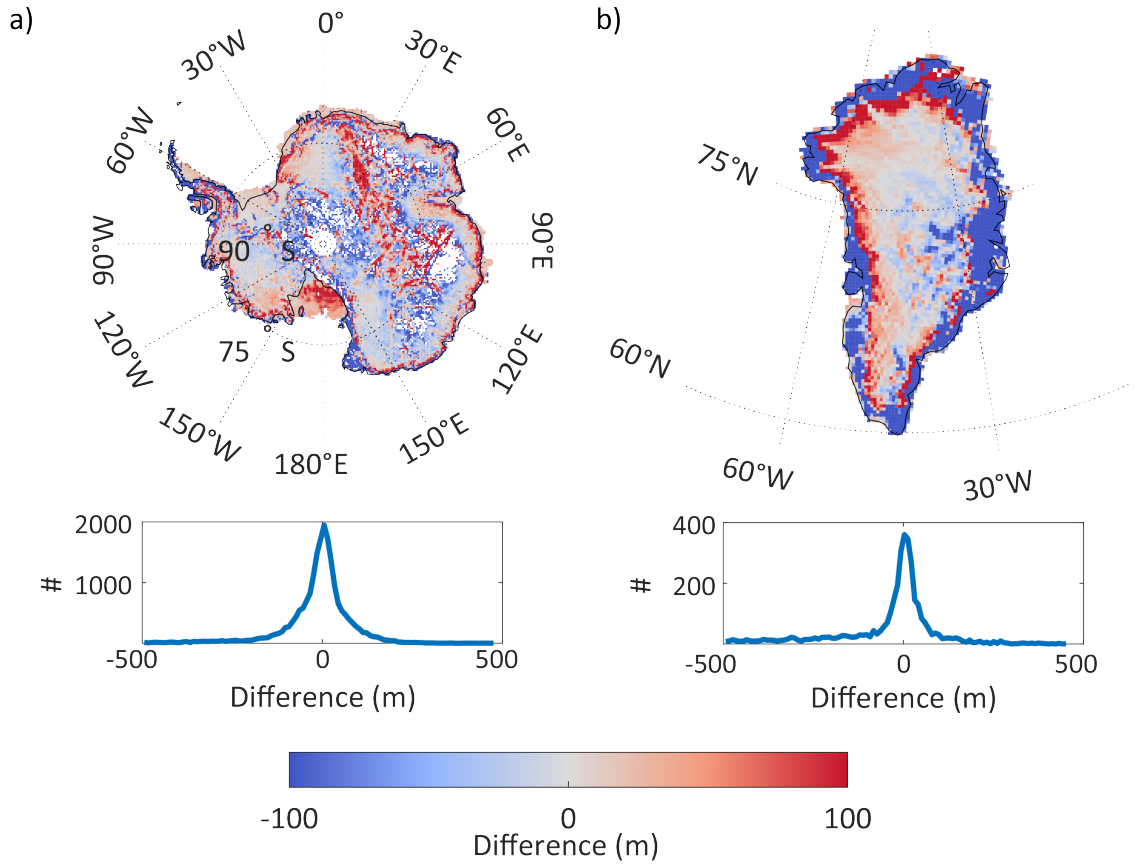

Figure 4.2: Error maps over a) Antarctica and b) Greenland with respective histograms (bottom). Error shown is comparison DEM subtracted from TDS-1 DEM .Comparison DEMs are CryoSat-2 v1 1 km DEM (Slater et al., 2018) and GL-CCI for a) and b) respectively.

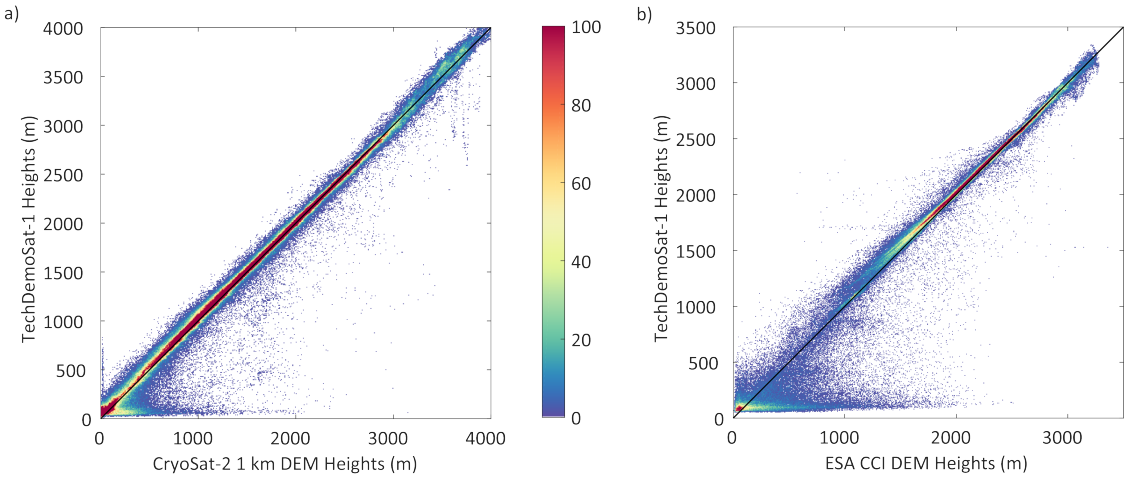

Figure 4.3: Density plot comparing height estimations from TechDemoSat-1 over a) Antarctica and b) Greenland and co-located data from the CryoSat-2 v1 1 km DEM (*Slater et al.*, 2018) and GL-CCI respectively. With 1:1 reference line (black)

applications of this technology that higher resolution seems to be limited by data availability rather than sensor footprint size.

There are a number of known issues with the TDS-1 data set including the uncertainty of the orbit and attitude of the satellite itself. These are covered in detail by *Clarizia and Ruf* (2016); *Foti et al.* (2017). Attitude information is acquired from sun sensors, however, when in eclipse this is retrieved from magnetometers with higher uncertainty (at times up to 10°, (*Foti et al.*, 2017)). Large changes in attitude are found in the data when exiting eclipse. However, the error patterns seen here show no obvious relationship to these fluctuations.

The data considered here include those collected in both Automatic Gain Control Mode (November 2014 – April 2015) and Fixed Gain Mode (April 2015 – end). A strength of the elevation algorithm used here is that it is robust to fluctuations in absolute power levels caused by such changes in mode of acquisition, due to its use of the shape of the waveform and the power relative only to its peak. This is especially valuable as the power received by TDS-1 is uncalibrated with respect to that transmitted from the GPS satellites and not normalised for antenna effects.

The different averaging employed for all DEMs produced and used as comparisons here are likely to result in errors when compared to one another. Seasonality and shorter time scale temporal changes were considered, however, they were not found to be connected to the discrepancies between the datasets (results not shown).

4.5 Discussion of the Benefits and Limitations of the technique

In addition to the novelty of measurements over the geographic poles, which were previously not possible with satellite altimetry; the primary benefits of this technique result from the low power and mass of the receiver. These mean that a low cost multi-satellite mission is feasible with the potential to increase the spatial and temporal resolution of observations far beyond those in the present study. The use of a technology demonstration mission limits the data available here and were this

technique to be exploited using dedicated platforms designed for these measurements, a significant increase in the available data could be expected. For example, the continuous operation of a single sensor would lead to a 300% increase in data as compared to the initial TDS-1 mission. If, in addition, a larger number of reflections were to be tracked at once, this would also multiply the data available, giving a many-fold increase in the spatio-temporal resolution of products. As seen in this study, the higher resolution of the product gives an increase in accuracy, indicating that the footprint of the measurements is not the limiting factor on the resolution of the data product, but the quantity of data available. This results in a compromise necessary to maximise coverage over the area of interest. A dedicated mission would require a full error budget appraisal, accounting for corrections required due to the design of the sensor and the auxiliary measurements necessary to enable these. It is likely, in addition, that a dedicated mission could also collect phase information from the reflected signals in order to greatly improve the accuracy of the height retrievals, as seen in *Hu et al.* (2017); *Li et al.* (2017).

Here we detail sources of error and limitations of this dataset. Due to the unknown physical properties of the material, the penetration of L-Band into snow and/or ice is a significant unknown (*Passalacqua et al.*, 2018). This is primarily due to the wide range of electromagnetic changes snow and ice undergo in terms of varying densities and precipitation regimes as the snow is compacted and the glacial ice formed, with both the sub-surface properties and those of the snow on top affecting the signal (*Brucker et al.*, 2014; *Leduc-Leballeur et al.*, 2017). *Cardellach et al.* (2012) measured the penetration of GNSS signals of up to 300 m over dry snow in Antarctica, whilst similar studies at L-Band over glacial ice in Greenland have yielded between 3 m and 120 m of penetration depending on the terrain, (*Li et al.*, 2017; *Mätzler*, 2001; *Rignot et al.*, 2001). These corrections are not applied to the dataset here due to the unknown characteristics of the ice and snow at the time of the retrieval. An additional factor is the atmospheric uncertainties at high latitudes resulting in ionospheric and tropospheric effects on the signal. These are thought to introduce errors of around 10 m at the equatorial maximum (*Hoque and Jakowski*, 2012) with errors being smaller at higher latitudes, and thus these are much smaller than the error magnitudes found here (assuming that the comparison

DEMs are "truth", but they too, of course, contribute to the RMS errors).

4.6 Conclusions

This study demonstrates that high resolution bi-static altimetry of ice sheets is possible with GNSS-R in both hemispheres to an accuracy of under 10 m where compared to contemporary elevation models. With increased data availability through dedicated GNSS-R missions and sensors designed for the purpose, high resolution altimetry of the polar areas, including the region surrounding the South Pole, would be possible at a higher resolution than that obtained here, where it is limited primarily by data availability. As the platform requires only a receiver, this technique is inexpensive, lightweight and low power, lending itself to a constellation configuration. Future proposals, such as G-TERN (*Cardellach et al.*, 2018), present the concept of a constellation similar to CYGNSS with a polar focus. Such a mission would allow further increases in the spatio-temporal resolution of the measurements, and through this allow measurements of even the most dynamic aspects of the cryosphere. The feasibility of such a mission would depend on the detailed error budget for the measurements (beyond the scope of this paper). Accuracies may be increased further through the use of phase delay information (*Cardellach et al.*, 2004; *Li et al.*, 2017) and interferometric techniques. In addition, constraining specular point locations and improved modelling of the signal within the ice sheet will also improve estimates.

Chapter Summary

Chapter 4 has developed the techniques demonstrated in Chapter 3, fulfilling Aim Aim 2 by improving the technique through three main tools to decrease the uncertainty in the Antarctic DEM by approximately 8 metres. This was achieved through re-tracking the waveforms to use the delay at 70% of the peak power of the delay-Doppler Map (DDM), spatial filtering to allow the inclusion of previously excluded data, and a larger dataset that includes an additional 13 months of data. These changes allow the coverage over the Antarctic ice sheet to be around 15% higher, and measurements over the South Pole itself to be made. The application of this algorithm over the Greenland Ice Sheet demonstrates its performance over a wider range of terrain, in particular showing its shortcomings over the steep rocky peripheries of Greenland.

Applying the data and filters developed in Chapters 3 and 4, Chapter 5 will focus on the sea ice component of the cryosphere to assess the use of GNSS signals for detection of sea ice for the fulfilment of Aim 3.

Chapter 5

Sea ice detection using GNSS-R data from TechDemoSat-1

Published as:

Cartwright, J., Banks, C. J., & Srokosz, M. (2019). Sea ice detection using GNSS-R data from TechDemoSat-1. Journal of Geophysical Research: Oceans, 124, 5801–5810. https://doi.org/10.1029/2019JC015327

Supporting information and typeset paper in Appendix C

Abstract

A new method for the detection of sea ice using Global Navigation Satellite Systems-Reflectometry (GNSS-R) is presented and applied to 33 months of data from the UK TechDemoSat-1 mission. This method of sea ice detection shows the potential for a future GNSS-R polar mission, attaining an agreement of over 98% and 96% in the Antarctic and Arctic, respectively, when compared to ESA's CCI (European Space Agency's Climate Change Initiative) sea ice concentration product. The algorithm uses a combination of two parameters derived from each delay-Doppler Map (DDM) to quantify the spread of power in delay and Doppler. Application of thresholds then allows sea ice to be distinguished from open water. Differences between the TechDemoSat-1 sea ice detection and comparison datasets are explored. The results provide information on the seasonal and multi-year changes in sea ice distribution of the Arctic and Antarctic. Future potential and applications of this technique are discussed.

Plain Language Summary

Monitoring of sea ice is essential in order to see the effects of a changing climate as well as understanding potential changes in the future. As a highly dynamic component of the cryosphere, sea ice plays an important role in these changes. Due to the remote nature and large area of sea ice, this must be performed through satellite observation in order to limit the spatial and temporal bias seen with in-situ data. Presented is a novel technique for the detection of sea ice using GPS signals reflected from the ocean surface. A simple, low-cost receiver picks up these signals from a spaceborne platform. In this case, data are collected from UK's TechDemoSat-1 mission, which although not designed for such measurements, gives excellent agreement with sea ice extent data from existing published sources.

5.1 Introduction

Monitoring sea ice is important to observe and understand global climate processes and their changes, due to the dynamic role that sea ice plays in the physics of the Earth's climate, not least in altering the Earth's albedo (*Stroeve et al.*, 2011). As a key element of the climate system, sea ice also affects the ocean circulation and weather (*Comiso et al.*, 2003). From a practical perspective, there is also interest in detecting and mapping sea ice for maritime operations such as exploitation of oil and gas reserves and to determine possible shipping routes, especially in the Arctic (*Bird et al.*, 2008).

Global Navigation Satellite Systems-Reflectometry (GNSS-R) uses reflected microwave navigation signals (L-Band from Global Positioning System (GPS) or similar systems) to characterize the reflective surface and was first proposed in 1988 (*Hall and Cordey*, 1988). This technique is at present largely used to study winds over the ocean (eg. *Clarizia and Ruf* (2016); *Foti et al.* (2015); *Ruf and Balasubramaniam* (2019)). However, other Earth observation applications, such as ice sheet and ocean altimetry (eg. *Cardellach et al.* (2004); *Cartwright et al.* (2018); *Clarizia et al.* (2016)), the monitoring of soil moisture (*Chew et al.*, 2016), and the cryosphere (eg. *Gleason* (2006); *Rivas et al.* (2010)) are also being investigated.

Cryospheric applications include the detection and altimetry of sea ice (eg. *Alonso-Arroyo et al.* (2017); *Hu et al.* (2017); *Li et al.* (2017); *Yan and Huang* (2016)) , the altimetry of glacial ice (eg. *Cardellach et al.* (2004); *Cartwright et al.* (2018); *Rius et al.* (2017)) and permittivity of reflective surfaces (*Fabra et al.*, 2012; *Rivas et al.*, 2010). The use of these signals of opportunity and the need only for a receiver in space mean that GNSS-R is an extremely low-cost and, being a passive system, low-power method of remote sensing. Combined with the low mass of the sensor itself, this makes the approach ideal for applications in constellation missions, as in the case of Cyclone GNSS (CYGNSS), launched 2016, for monitoring of tropical cyclone winds (*Ruf et al.*, 2013). The eight CYGNSS microsatellites achieve an average revisit time of 4 hours (*Ruf et al.*, 2013). Such a high temporal resolution, combined with the spatial coverage enabled by this quantity of measurements would allow the monitoring of the dynamic sea ice system. However, the low inclination (35°) orbit of the CYGNSS satellites means that they cannot be used to monitor sea ice. A similar system for cryosphere applications (G-TERN) has been proposed (*Cardellach et al.*, 2018). In orbit and operational until recently, TechDemoSat-1 (TDS-1) carries a GNSS-R receiver and is in a high inclination orbit (98.4°). Data from it can be used to detect sea ice and thus these data are the focus of this paper.

Previous studies (eg. *Alonso-Arroyo et al.* (2017); *Rivas et al.* (2010); *Yan and Huang* (2016); *Yan et al.* (2017); *Zhu et al.* (2017)) have been shown to correctly distinguish between sea ice and open ocean in up to 98.4% of cases in the detection of sea ice compared to co-located passive microwave data. However, these studies were limited in scope, examining small subsets of TDS-1 observations only. This study builds upon and extends these previous studies by developing and applying a new method of sea ice detection to the complete dataset collected during the initial mission of TDS-1. In what follows Section 2 discusses the satellite, the sensor and the data used and then Section 3 describes the sea ice detection methods tested. Section 4 validates the results of the algorithm against the most recent European Space Agency (ESA) Climate Change Initiative (CCI) sea ice concentration product (*Toudal Pedersen et al.*, 2017) as well as the National Snow and Ice Data Centre (NSIDC) sea ice concentration product (*Cavalieri et al.*, 1996), OSI SAF ice edge

product (*Breivik et al.*, 2012; *OSI SAF*, 2019a) and MASIE operational ice edge product (*Fetterer et al.*, 2010). The likely sources of differences are then discussed. Conclusions of the study and a discussion of the future potential of GNSS-R for sea ice monitoring are given in Section 5.

5.2 TechDemoSat-1 and GNSS-R

Data from the GNSS-R sensor on TDS-1 are provided in the form of delay-Doppler Maps (DDMs). These represent the scattered power in the delay and Doppler domains, with a smooth surface yielding a coherent reflection with the majority of the scattered power coming from the specular point, and very little from the glistening zone around it (*Zavorotny and Voronovich*, 2000). This is visible in the DDM as a limited spread in the power distribution and a strong peak. Roughness is considered at the scale of the wavelength (19 cm), with sea ice or flat leads producing a more coherent DDM as compared to one from the open ocean, as the latter results in more scattering in the delay and Doppler domains due to the presence of waves on the sea surface. This distinct difference in the distributions of scattering from these two types of surface allows information on their properties to be determined. Where reflections are coherent, such as over sea ice, the footprint of the sensor is believed to be significantly smaller than passive microwave at 6 km by 0.4 km along-and across-track respectively (*Alonso-Arroyo et al.*, 2017; *Hu et al.*, 2017). The elongation in the along-track dimension is primarily due to the onboard incoherent averaging (1Hz) and, were this not applied, the footprint would be on the order of 400m by 400m.

The asynchronism of the orbit of TDS-1 with those of the GPS satellites, in combination with the ability of the sensor to receive up to four reflections at once, allows a varying web of specular points to be built up over time. This has the potential to provide high resolution data in both time and space, and therefore capture the dynamics of sea ice, even over the geographical North Pole. TDS-1 was designed as a satellite technology demonstration platform by Surrey Satellite Technology Ltd (SSTL), and carries eight separate payloads operated in an eight-day cycle. The data for this study were obtained from the Space GNSS Receiver

- Remote Sensing Instrument (SGR-ReSI), a low-power and low-mass sensor built from commercial components (full details can be found in *Jales and Unwin* (2015)) and in operation two days in every cycle. The satellite was launched in 2014 and placed into a quasi-sun-synchronous orbit (with a Local Time Ascending Node drift of 1.42 hours per year (*Foti et al.*, 2015)) with an inclination of 98.4° at an altitude of 635 km. In 2017, it came to the end of its demonstration mission, and has since been re-commissioned with the SGR-ReSI in operation continuously. Only data acquired before the mission extension will be considered in this study as data of antenna gain less than 0 dB has not been downlinked during the 24 hour operational phase, eliminating much of the data at high latitudes. The SGR-ReSI creates 1-ms DDMs, which are averaged over 1 second intervals prior to downlinking. These are then provided along with the metadata for the same period in 6 hour collection windows and are available at merrbys.co.uk. The DDMs consist of 128 delay bins and 20 Doppler bins, with resolutions of 0.252 chips (0.246 µs) and 500 Hz respectively.

The data considered in this study have been collected over almost 3 years of the initial TDS-1 mission (September 2014 – May 2017), using observations from both polar regions (north of 50° N and south of 50° S) and applying the land mask given in the ESA CCI data (*Toudal Pedersen et al.*, 2017). The TDS-1 data were then filtered following the approach of *Cartwright et al.* (2018), which ensures the reduction of noise, as well as the removal of data where the reflection has left the tracking window. Data were also removed where flagged as containing the direct (unreflected) component of the signal. In addition, data from Collection Period 12 (September 2016) were discarded due to inconsistencies in the DDMs resulting from changes in sensor settings during that period. Contrary to previous studies, data were not filtered according to gain control mode, antenna gain nor incidence angle to retain the maximum amount of data, particularly over the North Pole. It should be noted that the antenna gain of data points in the Southern Hemisphere is naturally higher than that of the Northern Hemisphere due to the distance of the sea ice region from the South Pole. This therefore leads to lower incidence angles and concomitant higher antenna gains.

The recently released CCI sea ice concentration product (version 2.1) was used as a comparison to ensure the highest availability of high quality reprocessed data for evaluation. This product is provided on a 25 km grid and was linearly interpolated to the location of the TDS-1 specular points. Any concentration above 0% was deemed to be sea ice and below this water. This threshold was used, rather than the conventional 15% concentration for sea ice coverage due to the sensitivity of the SGR-ReSI to the presence of sea ice. This choice was found to give the best agreement with derived parameters from the TDS-1 data and the largest separation of the two populations of DDMs associated with the different surface types. Other sea ice products such as that of the National Snow and Ice Data Centre Special Sensor Microwave Imager Sounder (NSIDC Special Sensor Microwave Imager / Sounder (SSMIS)) *Cavalieri et al.* (1996) were also tested and found to agree with the CCI product in 96% of cases using the 0% ice concentration threshold. This means that the CCI and SSMIS products agree 96% of the time regarding their classification of the surface as sea ice or open ocean. As such, any degree of agreement between the GNSS-R sea ice detection method and either dataset that exceeds 96% is an excellent result, given that the best available comparable data disagree at that level.

5.3 Methods and Results

A number of parameters were derived from the DDMs and compared to the presence of sea ice at each observation point. A simple method (Figure 5.1) was applied to assess the extent to which each of the derived parameters could be used to detect sea ice through the use of a straightforward threshold. This was done using histograms to assess the point at which the threshold should be placed to maximize the probability of correct assignment (the point at which the histograms of the sea water and sea ice cross). The DDM derived parameters tested have been defined below, many of which quantify the Trailing Edge Slope. Although the DDMs from TDS-1 are not calibrated with regard to direct signal power, observables from the maximum-normalized DDMs were considered, such as the ratio of power in the signal box to that of the noise (SNR) and the percentage of total power contained in

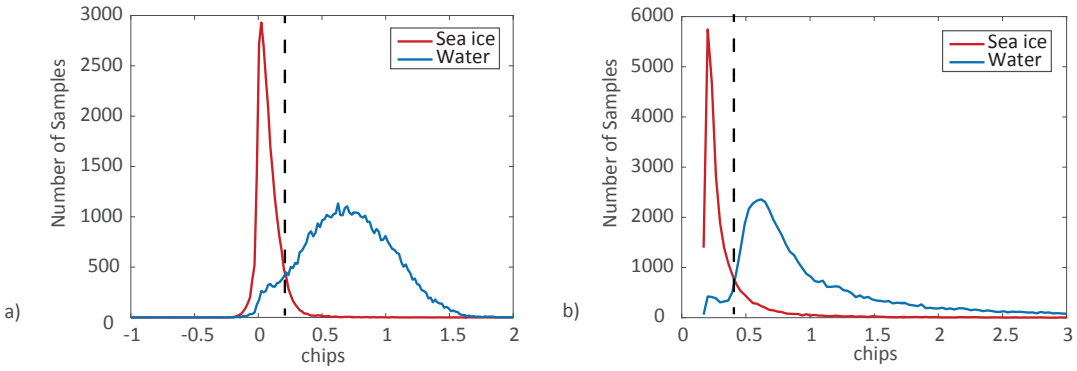

Figure 5.1: Threshold calculation example for February 2015 for both a) Offset Centre of Gravity (OCOG) and b) dy. Histograms of sea ice (blue) and open water (red) points with the threshold (black dashed) placed at the point of their closest approach between their peaks. Thresholds shown are 0.2074 and 0.4158 for OCOG and dy respectively.

signal boxes of varying sizes. Unfortunately the lack of phase information prohibits the use of some previously used GNSS-R parameters such as DDM Variance and Allan DDM Variance (*Clarizia et al.*, 2014).

1. ***OCOG*** – Similar to metrics used by *Yan and Huang* (2016) This parameter is based on that used in altimetry for the re-tracking of waveforms and identification of topographical changes (*Wingham et al.*). The waveform is selected and re-centered on the maximum power (in order to account for shifts of the maximum amplitude away from the zero-Doppler and zero-delay point). The center of mass of the waveform is then identified and the difference in delay between this and the maximum of the waveform calculated. This has been calculated for the waveform taken through the maximum amplitudes of the DDM (varying in delay space) and the Doppler- and delay-integrated waveforms.

2. ***dx and dy*** – The difference between the maximum amplitude and the location on the DDM where the scattered power has decreased to a given fraction of its maximum. The position of the maximum power of the DDM is determined in the Doppler domain and the corresponding waveform selected (i.e. a slice through the DDM corresponding to the maximum power). The distance is then calculated between the maximum power and the point at which it has fallen to a nominal level. See Figure 5.2 for a visual depiction of this

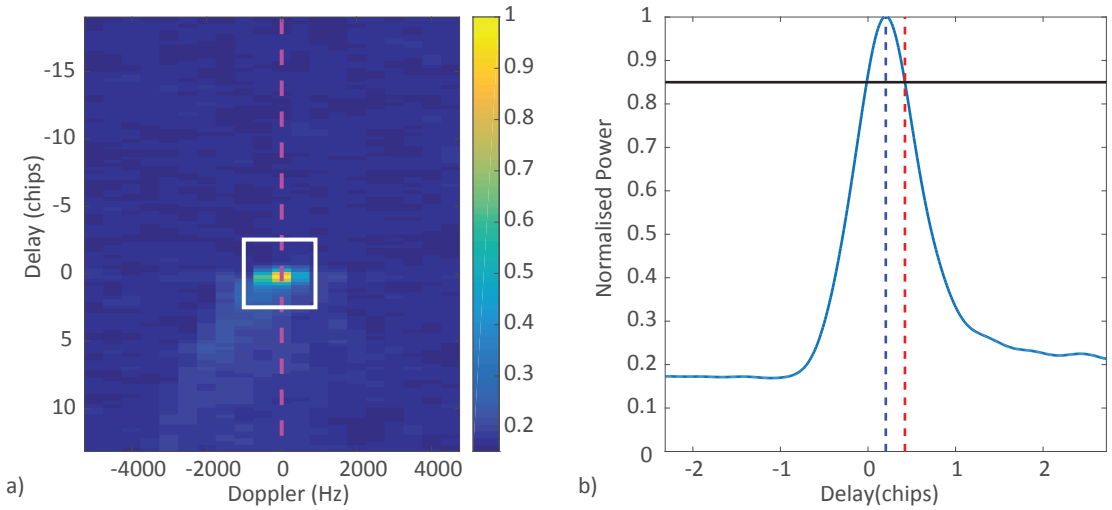

Figure 5.2: Calculation of dy observable. a) shows DDM normalized to its maximum, and the (magenta) line through which the waveform is taken. b) shows section of said waveform (white box in a)) with maximum (blue dashed line) and 85% (red dashed line) power marked. dy is the difference between the two delays.

calculation. In this case 85% of the maximum was chosen moving down the DDM. Also investigated were 65%, 75% and 95%. This was calculated in all four directions on the DDM (up and down - dy, left and right - dx). dy in the down direction can be considered another method of calculation of the Trailing Edge Slope.

3. ***DDMA (DDM Average)*** – As used by *Alonso-Arroyo et al.* (2017). The average value in a box around the maximum amplitude for the box sizes below. This average was computed both as a mean and a median for the maximum-normalized DDM as well as a median of the DDMs of proportional power (percentage of total DDM power contained in each of the Doppler and delay bins).

   (a) 3 (Doppler) x 3 (delay) bins

   (b) 5 (Doppler) x 3 (delay) bins

   (c) 7 (Doppler) x 3 (delay) bins

   (d) 20 (Doppler) x 3 (delay) bins

4. κ ***(Kurtosis)*** - The kurtosis has been calculated for the DDM of scattered power, for the waveform in the delay domain through the maximum amplitude

and for both the Doppler- and delay-integrated waveforms.

5. ***DDMS (DDM Sum)***- Sum of values in a box around the maximum amplitude for the same box sizes considered above (DDMA). This is calculated from the normalized DDM.

6. ***TES (Trailing Edge Slope)*** - The gradient calculated from the maximum amplitude of the waveform (taken in the delay domain through the maximum amplitude) to the point on the waveform 3, 6 or 9 bins later in delay.

7. ***Maximum Power*** - This is the maximum amplitude of the DDM in scattered power. This measurement is taken directly from the supplied DDMs and is uncalibrated.

8. ***Noise Floor*** - Average (median) value of a box in the signal-free region (first 5 delay bins, and all Doppler bins) of the normalized DDM (scattered power).

9. ***Signal-to-Noise Ratio (SNR)*** - Ratio of the signal ($\text{DDMA}_{\text{median}}$ 5 x 3 – as above) to the Noise Floor calculated in scattered power.

The parameters of OCOG (using the waveform through the maximum of the DDM) and dy (down the DDM to 85% of the maximum power) performed best in terms of agreement with the passive microwave comparison data set and data retention, in both the Arctic and Antarctic and are thus applied in this study. Full results of all parameters' combined performances can be found in the Appendix C. Essentially, these parameters (OCOG and dy) quantify the peakiness of the waveform (sea ice waveforms are much peakier than those for open ocean) and will be used to distinguish whether the DDM is due to a reflection from sea ice or open ocean. A training data set was extracted from the observations – in this case the first whole year of data in the Antarctic (2015), which is approximately 20% of the entire dataset. The training dataset was taken from the Antarctic rather than the Arctic, as the data are of a higher quality. This is due to the geographical difference in sea ice location, with a lower latitude dataset yielding lower incidence angles and higher antenna gains. The process was also performed with Arctic training data,

but with lower agreement, so this approach was not pursued. Thresholds were calculated on a month-by-month basis using the Antarctic training data in order to account for any seasonal changes in the ice surface. The median of these monthly thresholds was then calculated to give one threshold for each observable (OCOG = 0.2537 chips, dy = 0.4772 chips). Thresholds were then combined from the different derived parameters, with both criteria having to be met to determine the correct classification. This requirement results in the loss of some data (a further 7% after the filtering process) but improves the agreement with the comparison dataset overall (94% or 84% when the respective OCOG or dy threshold is applied alone, rising to 98% where combined).

5.4 Validation against ESA CCI Sea Ice Concentration

Where the combined thresholds are used, a high level of agreement is seen between the TDS-1 sea ice detection approach and that of the CCI data, at 98.4% in the Antarctic and 96.6% in the Arctic over the entire dataset (98.2% in the Antarctic where the training dataset is excluded). Assignment of points can be seen in Figure 5.3 for months as close as possible to the ice extent maximums and minimums for 2016 in the Arctic and Antarctic. Due to inconsistent DDMs, it is not possible to show the true minimum and maximum in September 2016 (this is Collection Period 12 and was subject to changes to the sensor settings) whilst 2015, as the training year would not have independently confirmed the success of the technique. Gaps in Figure 5.3 result from the varying amounts of data received in different months, due to the shared and experimental nature of TDS-1. Although the algorithm was trained using CCI data, similarly promising results are obtained when the results are compared to NSIDC detection (at >0% concentration) (*Cavalieri et al.*, 1996), OSISAF ice edge product (derived from both active and passive sources) (*Breivik et al.*, 2012) and the operational product MASIE for Arctic data (*Fetterer et al.*, 2010). Mapped comparisons of the ESA CCI, OSI SAF and MASIE datasets can be found in Appendix C.

Figures 5.4 and 5.5 display the results of the validation as compared to data

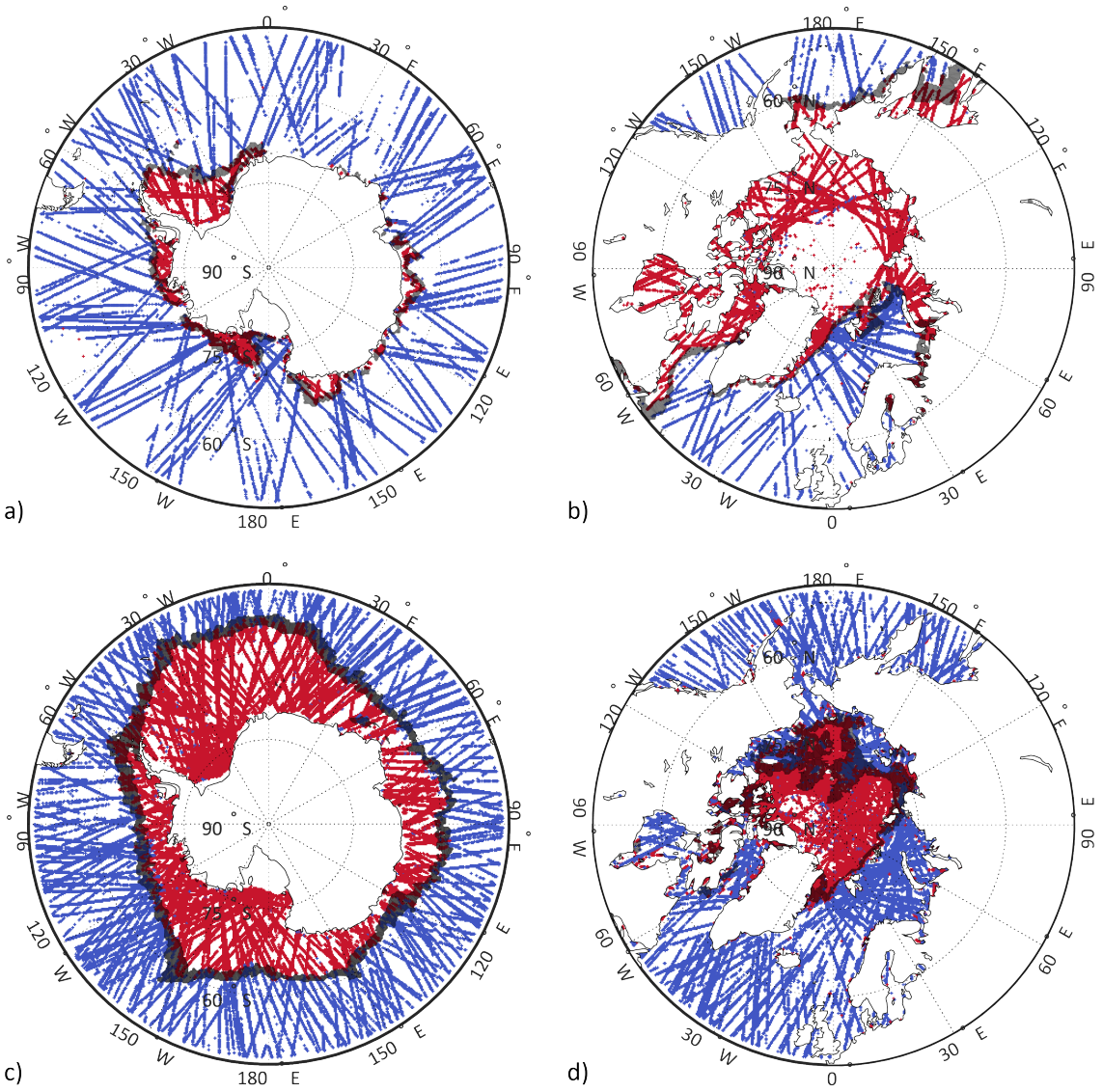

Figure 5.3: Surface characterization from GNSS-R data for Antarctic (a and c) and Arctic (b and d) for as close as possible to the minimum (a) February and d) August) and maximum (b) February and c) August) extent of 2016. September cannot be shown as the majority of the data is filtered out due to inconsistent DDMs (Collection Period 12). Red displays a sea ice assignment and blue an open water assignment. Black shaded area represents the data in the ESA CCI product that transitioned between sea ice and water during the month, and thus may contain correct ice or water assignments. Poleward of this shaded ring is ice, and equator-ward, water.

Table 5.1: Algorithm performance assessment categories and performance breakdown in the Antarctic and Arctic.

	TDS-1 Assignment	ESA CCI Assignment	Antarctic	Arctic
True (Correct) Positive	Sea Ice	Sea Ice	48.8%	64.1%
True (Correct) Negative	Water	Water	49.6%	32.5%
False Positive	Sea Ice	Water	0.8%	2.5%
False Negative	Water	Sea Ice	0.8%	0.9%

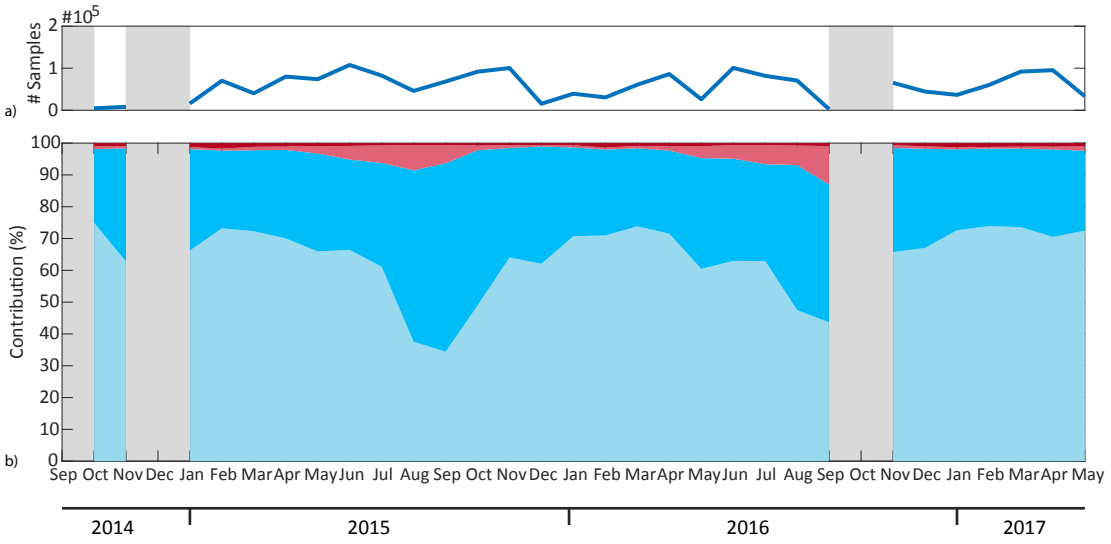

Figure 5.4: Result for sea ice detection in the Arctic: a) number of points after filtering in each month and b) Allocation of ice points using OCOG and dy using thresholds calculated over the Antarctic and applied to the Arctic. Light blue represents correctly identified sea ice, dark blue correctly identified open ocean, light red incorrectly identified sea ice (false positive) and dark red incorrectly identified open ocean (false negative). Grey shading represents no available data for that period.

from the ESA CCI product. The results are broken down into categories as seen in Table 5.1. The seasonal cycles are well captured, with the sea ice maxima (largest proportion of correct positives) visible in the expected months, February and September for the Arctic and Antarctic respectively. This 6-month offset is also seen in the sea ice minima, with the largest proportion of correct negatives seen in September in the Arctic and in February in the Antarctic. The double peak and increased false negative seen in September 2016 (Collection Period 12) of Figure 5.5 can be attributed to the low sample numbers for this month, with only 3000 useful data points in each hemisphere. It must be noted that the false negatives, although

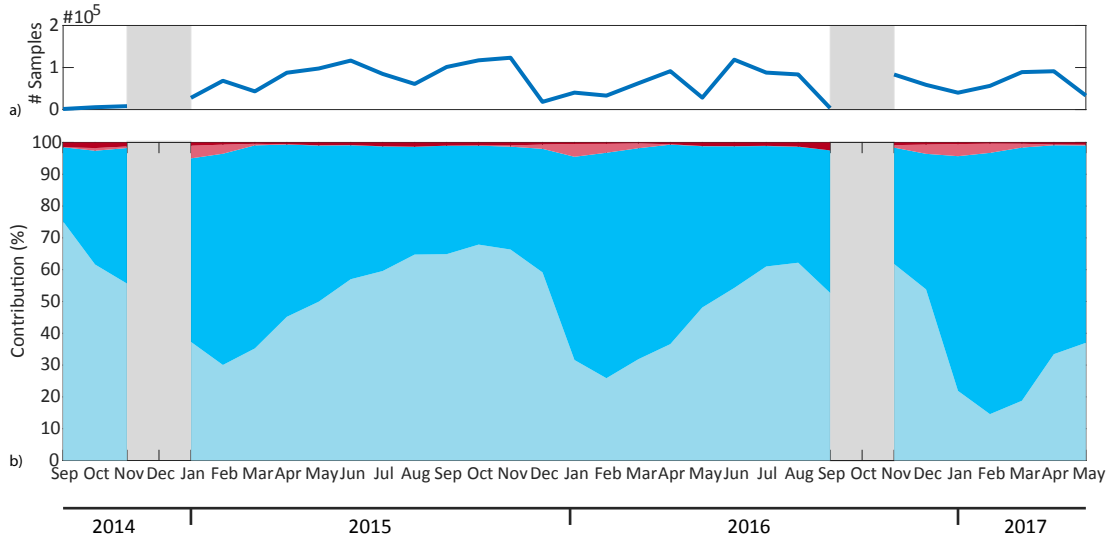

Figure 5.5: Results for sea ice detection in the Antarctic: a) number of points after filtering in each month and b) Allocation of ice points using OCOG and dy using thresholds calculated over the Antarctic and applied to the Antarctic. Light blue represents correctly identified sea ice, dark blue correctly identified open ocean, light red incorrectly identified sea ice (false positive) and dark red incorrectly identified open ocean (false negative). Grey shading represents no available data for that period.

present in both hemispheres are such a small proportion of the total that their presence is not clearly visible in the figures. Other points to note are the poorer performance of the algorithm in the summer months in both hemispheres, with a large increase in the false positives in these months, at times to over 10% of the data. A possible cause of these differences in detection is the various sensitivities of the different sensors to the sea ice and the differing behavior of microwave emissions from the surface captured by passive microwave radiometers and used in the CCI product as compared to the L-Band reflections used by GNSS-R. It is believed that the GNSS-R sensors may be more sensitive to the presence of sea ice, (*Alonso-Arroyo et al.*, 2017) and it is for this reason that the 0% concentration threshold for sea ice assignment was used in training the algorithm. The use of the more widely used 15% concentration threshold with these parameters yielded agreement of 97.7% and 95.4% with the CCI product in the Antarctic and Arctic respectively This effect along with that of snow on passive radiometer measurements *Rostosky et al.* (2018) may explain the lower agreement in the marginal ice zone and the increase in false positives (water categorized as sea ice) in the summer months, when higher melt and thin ice may lead to categorization of these points as water by

microwave radiometers (operating at higher microwave frequencies than L-band), as used in the CCI algorithm. The highly coherent reflections resulting from leads or meltwater ponds in the melt season may also cause the increase in false positives in the summer time.

In addition to the above discussion, there are some known issues with the TDS-1 dataset (covered in detail in *Foti et al.* (2015) and *Clarizia and Ruf* (2016)), including attitude and orbit uncertainties as well as experimental changes in settings due to its use as a technology demonstration platform. These uncertainties related to the location of the specular point are believed to be less than 3 km (*SSTL*, 2017) although this is thought to be an upper limit with likely errors less than a few hundred meters. As this is significantly less than the ESA CCI data resolution, this makes little difference to the comparison. As can be seen in Figure 5.3, many of the 'wrongly' categorized points (ice outside the shaded ring, or water inside) follow the ground tracks of TDS-1, which may suggest that the errors are related to the track as a whole, which may reflect a miscalculation of specular point. These are often in areas which could be easily screened out (for example in the Baltic Sea), as performed with the ESA CCI comparison data and other similar products. It has been found that where the algorithm was trained using Antarctic data, higher agreement is obtained for both hemispheres. This is believed to be due to the geographic differences in the regions of interest, with the Antarctic sea ice zone being further from the pole, and therefore having, on average, data of a lower incidence angle and higher antenna gain. This results in higher quality DDMs, with lower noise, aiding both metrics in the discrimination between sea ice and open ocean. It must also be noted that the higher presence of land masses in the sea ice margin in the Arctic has an effect on agreement here, with 52% of false positives in the Arctic lying within 50 km of a land mass. This is within the footprint of the sensor where a rough surface (such as land) is concerned. Regardless, the application of the same threshold in both hemispheres and the resulting good discrimination between sea ice and open ocean displays the robustness of this technique. As can be seen in Figures 5.4 and 5.5, there is at times a lack of data within the month. This is partly due to the shared nature of the platform and partly due to the combined threshold approach. The use of the filters described in Section 2 reduces the data to

approximately 46% of the original observations, and the use of a single observable would allow the use of the entirety of this dataset. Therefore, a compromise must be reached between agreement and quantity of data. Where OCOG alone is used to detect sea ice, this agreement falls to from 98.4% to 94.4% in the Antarctic, but retains 7% more of the original data. It should be noted, that whilst previous studies (*Alonso-Arroyo et al.*, 2017; *Yan and Huang*, 2016; *Yan et al.*, 2017; *Zhu et al.*, 2017) have attained similar or higher accuracies than those seen here, the detection techniques described in those studies are often used across only one season or a single track, and have not been applied across the dataset as a whole. The method developed and applied here is trained on 20% of the filtered data and shown to produce excellent agreement with CCI across the whole of the remaining data.

5.5 Conclusions and Future Work

This study has shown that sea ice detection using GNSS-R is possible with an agreement of 98.4% in the Antarctic and 96.6% in the Arctic through the use of two combined parameters and appropriate thresholds (where compared with state-of-the-art passive microwave data). This is the first time that sea ice detection has been performed using GNSS-R across such a large dataset, spanning 33 months of the TDS-1 mission. Maps of sea ice have been created on a monthly basis, including the area over the North Pole that is unavailable for most active remote sensing methods. This technique shows great potential for future missions, with the extremely low-power, low-cost and lightweight nature of the sensor lending itself to a polar constellation mission, in a format similar to that of CYGNSS. Such harnessing of these signals of opportunity by a platform and sensor optimized for such measurements would allow high spatial and temporal resolution monitoring of the dynamic sea ice system (average of 4 hour revisit time for CYGNSS). Improved modelling of the interaction of L-Band with the sea ice itself will allow further increases in accuracy and applications of GNSS-R to sea ice classification and snow cover (not considered here). Comparisons of GNSS-R data with results from passive radiometers will facilitate this understanding, especially data from L-band missions

such as SMOS (e.g. *Kaleschke et al.* (2012)), which operate at similar frequencies to GNSS-R.

Chapter Summary

This chapter fulfils Aim 3 through the demonstration of the capabilities of GNSS-R for sea ice detection, showing not only good agreement with independent comparison datasets from passive and active remote sensing, but also with the seasonal cycles in both hemispheres. Interannual variations can also be seen in the data too; for example, in the Antarctic Figure 5.5 shows September 2014 echoing the known high sea ice extent of that year - despite a reduction in useable measurements. In contrast, September 2016 displays a large reduction in sea ice extent, a recovery after the autumn, and then a final low ice extent in 2017, also visible at the end of the time series. These patterns are consistent with ice extent records for this period.

Chapter 6

Conclusions and Future Work

This work applied the novel technique of Global Navigation Satellite Systems-Reflectometry (GNSS-R) to characterise the cryosphere in order to assess the potential of this technique for increasing knowledge of physical ice processes and state, and so provide a basis for future monitoring of the cryosphere in this way. GNSS-R is uniquely suited for these measurements, using reflected navigation signals to understand more about the Earth's surface, including height measurements over the great ice sheets and sea ice detection. This has been proved through the fulfilment of four aims specified in Section 1.6.1.

This thesis demonstrated the application of height algorithms to the data collected from Low-Earth-Orbiter TechDemoSat-1 (TDS-1) in order to estimate the height of glacial ice in both Antarctica and Greenland. Chapters 3 and 4 demonstrated both initial applications and improvements of this technique respectively, resulting in the first published satellite altimetry measurements over the South Pole itself. These data display the high accuracy of the technique when compared to a number of traditional altimeter datasets (laser, radar, airborne and satellite) in addition to photogrammetry techniques. Data achieved agreement to within 33 metres of Root Mean Squared (RMS) error over the South Pole itself when compared to airborne laser measurements, and a median difference of 40 cm across the entire Antarctic Ice Sheet according to comparisons with a recent Digital Elevation Model (DEM) from CryoSat-2 (*Slater et al.*, 2018). This median difference is lower than the discrepancies between the DEM products themselves (Table 2.1) and the RMS error over the Antarctic continent (52 - 57 metres, Table 4.2) is comparable to

that of the external datasets (49 - 76 metres). Standard deviation of the measurements over the extent of the ice sheets can be seen in Figure B.2, with an average of 2 metres of standard deviation over the Antarctic ice sheet, and 4 metres over the Greenland Ice Sheet, much lower in magnitude than any considered error sources discussed in Chapter 4. Chapters 3 and 4 therefore fulfil Aim 1 and Aim 2.

Chapter 5 of this thesis demonstrated the application of GNSS-R to the detection of sea ice. Comparison to 4 existing datasets shows high agreement of >98% in the Antarctic and >96% in the Arctic. The differences seen between the hemispheres (with lower agreement seen in the Arctic across all comparison datasets) reveal the factors affecting these measurements, with proximity to the geographic pole as well as the higher occurrence of land adjacent to the sea ice zone in the Arctic leading to higher disagreement with existing datasets. Many of these erroneous points would be easily excluded with the application of a climatology mask, such as those used in the products compared to in Chapter 5. The time series of ice detection allows seasonality to be clearly seen in both hemispheres as well as agreement with large scale extent patterns over the years in question. This can be seen in Figure 5.4 and Figure 5.5, where the longer term seasonal patterns have been particularly well captured in the Antarctic, with the high extent in 2014 through to lower than usual extent in 2017. The detected increase in ice (or open water) throughout the winter (or summer) displays the efficacy of this technique, not just for identifying ice but also detecting the ice-edge boundary. This is being explored in further work relating to the detection of polynyas and large leads using these same GNSS-R data. Chapter 5 therefore fulfils Aim 3 of this thesis.

6.1 Potential role of GNSS-R in cryosphere remote sensing

The primary objective in the investigation of novel techniques and technologies is always to identify what this technique could add to those currently available and so how might they complement existing techniques. It is this that we explore in this section through the discussion of Aim 4.

"Connect derived parameters from TDS-1 data to external datasets to provide a comprehensive overview of the advantages and disadvantages of the use of GNSS-R over the cryosphere in relation to existing methods and products."

Chapters 3, 4, and 5 have all provided comprehensive comparisons of the derived parameters to existing datasets from a wide array of sensor types. This section will seek to discuss these and areas for future work to address unknown error sources and constrain possibilities for use of GNSS-R as part of a wider multi-sensor contribution to monitoring of the cryosphere.

The advantages of a GNSS-R sensor correspond for the most part to its use of signals of opportunity. This allows the sensor to be extremely low-power, -mass and -cost, especially when compared to existing techniques (Table 1.1). It also results in a varying web of points, attaining a higher spatial resolution with time in orbit for less dynamic systems, such as glacial ice. This is amplified by the low-cost nature lending itself to flying constellation missions. Examples include Cyclone GNSS (CYGNSS), launched by NASA in 2016; the polar-orbiting GNSS-R constellation planned for launch this year by commercial company Spire Global; and the proposed G-TERN cryosphere mission (*Cardellach et al.*, 2018). Although widely applied to measurements of significant wave height and wind speed, the application of GNSS-R to the cryosphere is a natural step given the high coherence of reflections over ice surfaces, especially those over sea ice.

6.1.1 Glacial Ice Altimetry

In the altimetry of glacial ice, complementary techniques are often used to best measure all areas of the ice sheet, creating mosaic Digital Elevation Models. Although this is partly due to the large scale of the ice sheets, it is in many cases an attempt to utilise components of different techniques that best measure the different environments encountered; eg. large scale radar altimetry in addition to more detailed studies of the more accessible, highly varied ice sheet peripheries with higher resolution techniques such as Synthetic Aperture Radar (SAR), photogrammetry, and laser altimetry (where cloud cover permits the use of the latter two). There can be no doubt that the remote centre of the Antarctic Ice Sheet, near

the South Pole is often neglected in these studies, with no satellite altimeter technique capable of capturing the conditions so far South due to orbital constraints. The remaining satellite option for the region is the computationally expensive narrow swath (250 km for Sentinel-1 in Interferometric Wide Swath mode) of SAR data. A simple implementation of GNSS-R as presented here offers an alternative; very low computation costs in addition to a fraction of the platform and sensor costs associated with SAR measurements. Indeed, a GNSS-R mission for another purpose (soil moisture, sea ice detection, wind speed) could easily provide these measurements as well. The South Pole and the area surrounding it has always been assumed to be a relatively stable environment, therefore not necessarily requiring frequent measurements, however with changes in the physical system of the planet, GNSS-R could offer a reassuring check on this most remote of regions, and could be combined with higher coverage or accuracy techniques to give a more complete DEM.

In terms of the disadvantages of this technique, these currently stem from the number of unknowns in the measurements - the penetration depth into snow and ice, atmospheric corrections - and the coarse resolution of the product in addition to the incomplete coverage. The majority of these are discussed below (Section 6.2) and would be solved were GNSS-R to be used for such a purpose, with increased measurements (from a dedicated platform/s and receipt of more than four signals at one time) improving the accuracy and resolution of the end product and full error budgets accounting for atmospheric and penetration effects on the signal. It must be noted that the primary DEM used here for comparison over the Antarctic Ice Sheet uses over 250 million observations, in contrast with 2 and 5 million respectively for TDS-1's initial and extended missions contributing to our studies here. Main components of the error budget thought to have contributed to the error seen here are the penetration depth and the atmospheric effects. The latter of these is thought to be a maximum of 10 metres in error and the former is largely unknown at L-Band. In the dry snow zone of Antarctica, penetration depth has been measured at around 300 metres (*Cardellach et al.*, 2018), however lack of information regarding the state of the surface at the time of the TDS-1 measurements makes it difficult to assess the penetration expected in each measurement.

These errors and unknowns are not thought to invalidate the findings here, as over the Antarctic Ice Sheet, RMS error was 52, 57 and 52 m for comparisons with CryoSat-2; combined ERS-1 and ICESat; and Bedmap-2 DEMs respectively (from Table 4.2). Section 2.5 suggests that the three DEMs differ significantly amongst themselves, as seen in Table 2.1, at between 76 and 49 metres of RMS error. Over the Greenland Ice Sheet, however, error varied more at 124, 129 and 166 metres of root-mean-squared error for comparisons of TDS-1 with the ESA CCI product; ERS-1 combined with GeoSat; and Greenland Ice-Sheet Mapping Project (GIMP) DEMs respectively (Table 4.2). For comparison, Table 2.2 also shows a greater disagreement between the Greenland products than the Antarctic ones, although all have closer agreement with each other than with TDS-1 over Greenland. It is necessary therefore to study further the interaction of the GNSS-R signals through the glacial ice and on the rocky peripheries before reliance on this technique over the Greenland Ice Sheet itself.

6.1.2 Sea Ice Detection

In terms of the contribution of GNSS-R to sea ice detection, Chapter 5 shows that the reflected L-Band signals have a high sensitivity to the presence of sea ice in addition to a footprint over 200 times smaller than routinely used passive microwave sea ice extent metrics. This gives potential for higher resolution sea ice monitoring in both space and time (if employed in a constellation configuration). It must also be noted that in contrast with higher frequency passive microwave techniques, L-Band radiation is not affected by atmospheric conditions and as such can be relied upon in a wider array of conditions. The main disadvantages of using GNSS-R for sea ice detection stem from its production of point measurements, rather than swath imagery - although if sensors were to be able to collect all reflections in view, this would minimise this issue.

6.2 Future work to realize potential

As a technology demonstration mission, TDS-1 had a limited scope in both time and hardware. In order for a dedicated cryosphere GNSS-R mission to be feasible it might reasonably be expected to be necessary to make the following adjustments in order to maximise data collection and usability: increased knowledge of attitude and orbit; extended period in orbit; receipt of more signals at one time ("all in view" if possible); constellation configuration; continuous sensor operation; and collection of phase data. These features would be natural to implement on a dedicated platform, providing many times more data and as such improvements offered by these changes are not discussed further below.

6.2.1 Glacial Ice Altimetry

In order to improve the accuracy of glacial ice altimetry measurements, a full breakdown of errors relating to atmospheric effects and propagation of signal into snow and ice under different conditions would be necessary. The increased availability of GNSS-R data would allow this to be studied across different seasons and regions of the ice sheets, but basic comparisons could be done with the time-limited TDS-1 dataset. These factors were briefly investigated as causes of differences between datasets here, but a detailed investigation into these was not possible within the time span of this project. In order to undertake this work, seasonal components of the signal can be identified, increasing understanding of the signal and the conditions. Such studies would allow these influences to be taken into account in future measurements according to regions and seasons. In addition, a study of the population of overestimates seen in Chapter 3 and removed using the incidence angle filter may provide a correction for these data, which would enable an increase in the overall accuracy without the need for the spatial averaging applied in Chapter 4, thus increasing independence of measurements.

6.2.2 Sea Ice

Beyond the scope of this thesis, a further study is underway into the use of GNSS-R for the detection of polynyas and large leads, following on from Chapter 5. This involves comparing the areas in which the TDS-1 assignment differs from that of the comparison dataset and processing these along-track in order to ascertain statistics on the areas in which TDS-1 detects open water in the ice pack and the comparison dataset does not, and vice versa. The identification of these regions then allows SAR images to be acquired in the area and visual verification of the nature of the surface. In addition, comparisons are being carried out into the sizes of openings sensed through TDS-1 and the comparison dataset as well as the nature of the area, for example sea ice concentration.

Application of these techniques to operational datasets - collaboration with Spire Global

In addition to the studies detailed here, a paid placement with Spire Global was completed within the timescale of this doctorate. These studies were completed outside of the period of candidature and are therefore not fully detailed in this thesis, but focussed on the feasibility of the detection and classification of sea ice using grazing angle GNSS-R measurements from in-orbit Radio Occultation (RO) satellites. RO satellites measure the structure of the atmosphere by the propogation of GNSS waves through it. The refraction of the signal allows measurement of the atmosphere along that path, and the movement of the GNSS satellite as it goes down below the horizon in relation to the RO satellite provides a scanning mechanism. This technique uses the direct component of the GNSS signal, however if modified these satellites can instead receive the reflected component, providing grazing angle GNSS-R measurements of the Earth's surface. The studies carried out at Spire Global, with the phase data from the grazing angle GNSS-R signal, successfully applied the techniques used in Chapter 5 to develop a sea ice extent dataset and from there, reapplied these techniques to delineate between First-Year and Multi-Year ice, using the *OSI SAF* (2019b) datasets. Figure 6.1 summarises this work, that has now been further developed and made operational within Spire's

data processing.

This commercial application of the techniques developed in the course of this doctorate displays the clear potential contribution of GNSS-R to sea ice detection. Increased availability of GNSS-R data would allow an application of this on a larger scale and more rigorous studies of the factors that control the signal coherence. This would benefit all cryosphere applications, including those over land (for example, snow and permafrost - not considered here).

6.3 Summary

This thesis shows that GNSS-R can provide data on both glacial ice height and sea ice extent and that future missions will provide an opportunity to develop and build on these results. GNSS-R is unique in its ability to provide data with such a small footprint at such low cost. Thus, data from such platforms could provide valuable high resolution information on the state of the cryosphere. Sensors of this nature (eg. CYGNSS) are already providing information on sea state and soil moisture, the launch into polar orbit of similar constellations would enable an array of cryosphere measurements to be acquired in addition. This would add another dimension to remote sensing of the cryosphere and complement existing techniques to further increase our understanding of these critical to climate, dynamic and remote regions.

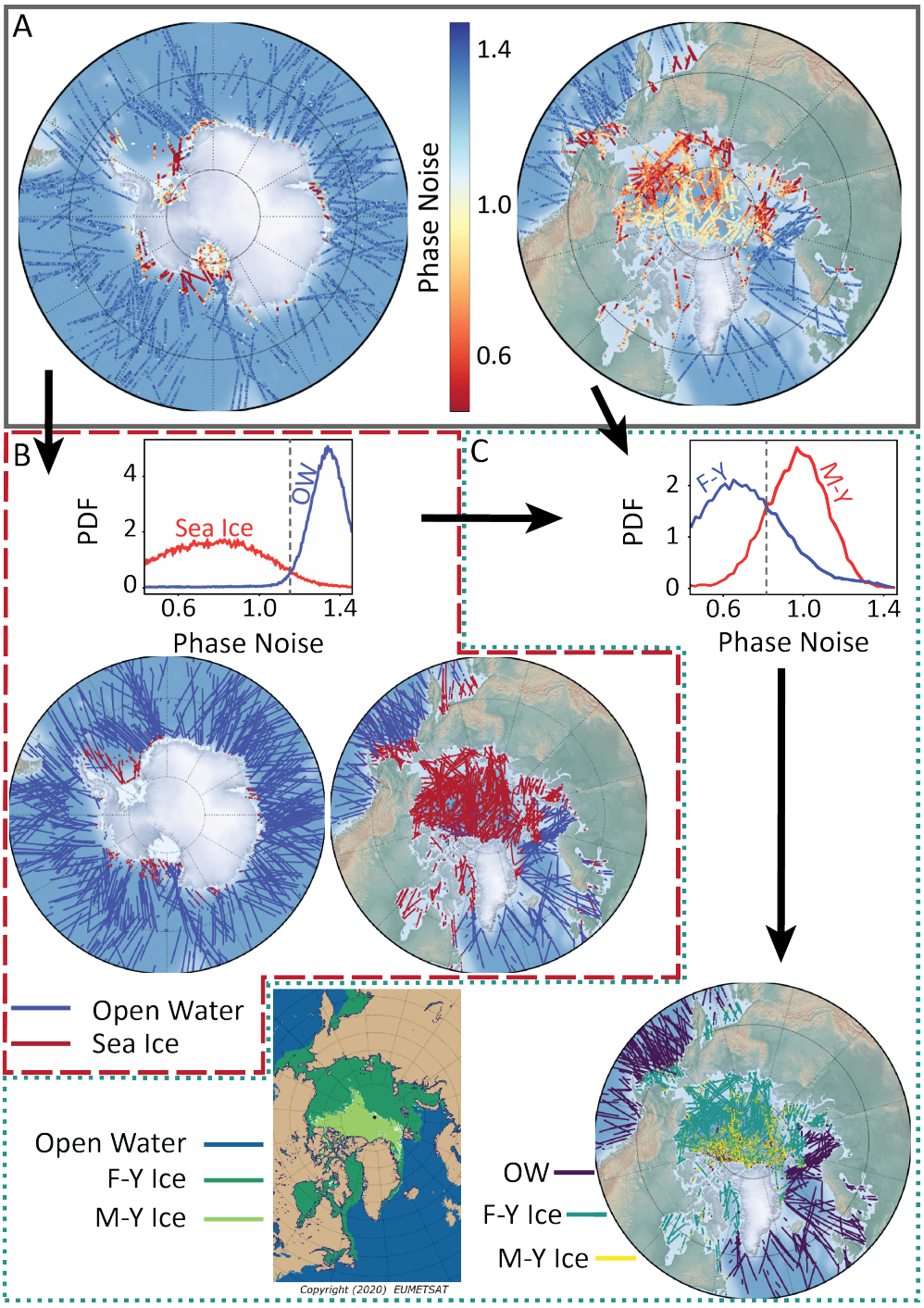

Figure 6.1: Summary figure of collaborative work with Spire Global. Box A (solid outline) shows input data of the phase noise in radians over two weeks (5th March - 19th March 2020) in both the Antarctic (left) and Arctic (right). Box B (dashed outline) shows the application of techniques from Chapter 5 to identify sea ice and open water (OW) using a training dataset from *OSI SAF* (2019a). This includes the probability density functions of the parameter and the application of the threshold to the data in the Antarctic (left) and Arctic (right). Box C (dotted outline) shows the progression of this ice detection to ice type classification in the same manner using an ice type training dataset from *OSI SAF* (2019b) (shown bottom left for comparison). OW = Open Water; F-Y = First-Year Sea Ice; M-Y = Multi-Year Sea Ice.

Appendix A

Appendix - Independent DEM of Antarctica using GNSS-R data from TechDemoSat-1

Contents

Text A.1 - Height estimations without incidence angle filter

Figures A.1 and A.2 show the height estimates processed in the same manner as those in the main body of the text, but including specular points with incidence angles greater than 55°. These data are filtered only by maximum amplitude Doppler and DDM kurtosis before being input into the existing height algorithm (*Clarizia et al.*, 2016) and removing all negative points. Results are then gridded by median values in a 50 km x 50 km grid.

Figure A.1 shows the potential of this technique to cover the pole region, which currently is not possible with satellite altimetry.

Figure A.2 compares the DEM presented in Figure A.1 with co-located data from the CryoSat-2 DEM 1 km v1.0 (*Slater et al.*, 2018). The CryoSat DEM has been interpolated to the location of the TechDemoSat-1 specular points for comparison of data. The double line seen at high elevation shows the tendency of the technique to over-estimate. These overestimates are linked to high incidence angles and, as we are currently unable to correct for these effects, the affected points were removed from the dataset presented in the paper.

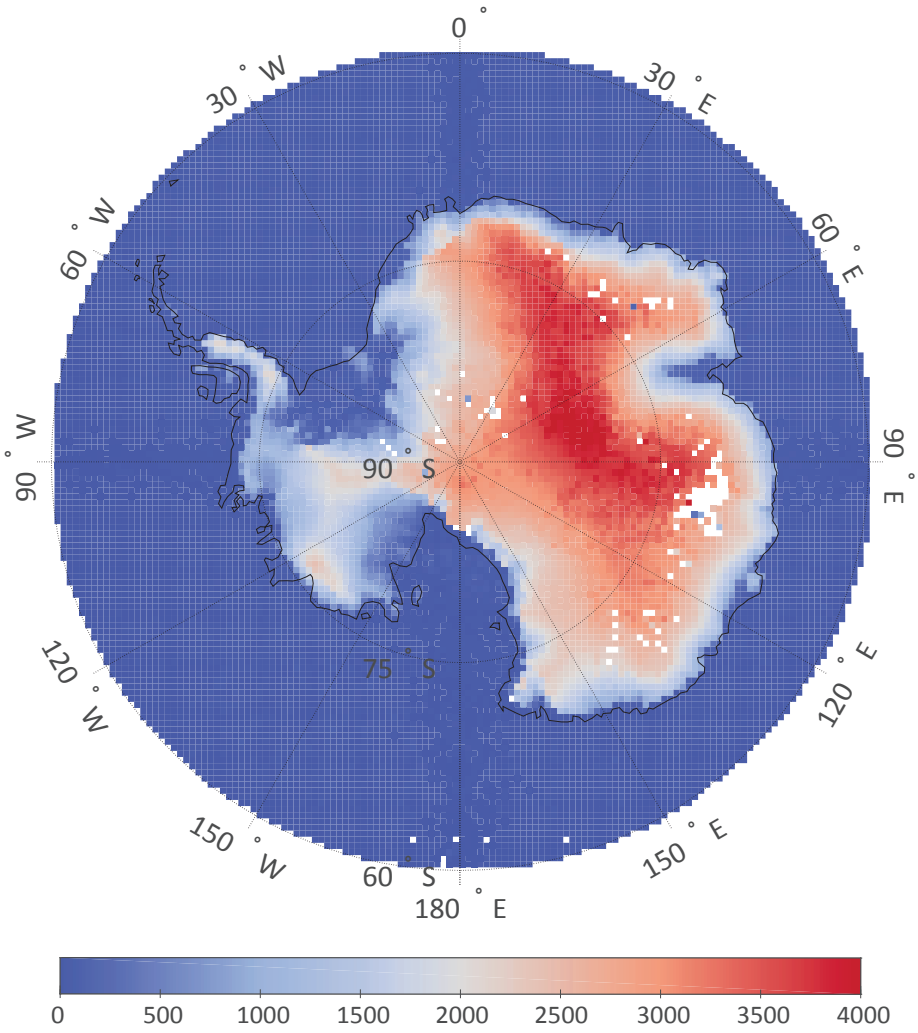

Figure A.1: Digital Elevation Model TechDemoSat-1 data without filtering for angle of incidence. Elevations are shown in metres above the ellipsoid with white denoting no available data. Data have been gridded by median at 50km resolution

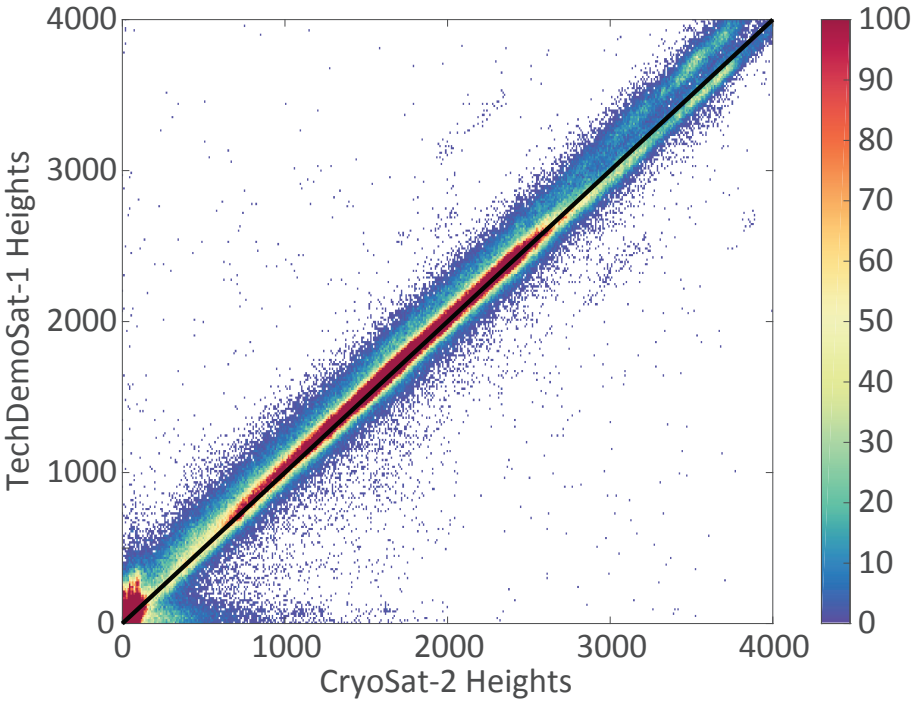

Figure A.2: Comparison of co-located data from CryoSat-2 DEM and TechDemoSat-1 without filtering for incidence angle with 1:1 reference line (black).

Text A.3 - Measurement Geometry

Figure A.3 shows the measurement geometry involved in GNSS-R height estimations.

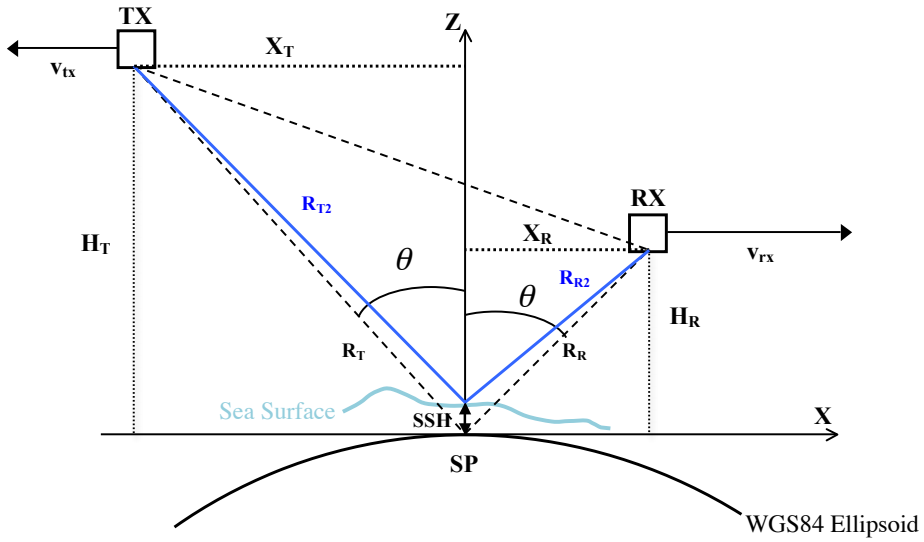

Figure A.3: Measurement Geometry of GNSS-R height estimations. Paths between the receiver (RX) and transmitter (TX) and their incidence angles (θ) can be seen as well as the heights of the transmitter and receiver(H_T and H_R). Reflections from the surface are shown (blue), heights (black, dotted) and modelled path of GNSS waves reflected off the ellipsoid (black, dashed). Figure from *Clarizia et al.* (2016).

Text A.4 - Delay estimate method

Figure A.4 displays the methodology used to find the delay estimate used in the height calculations.

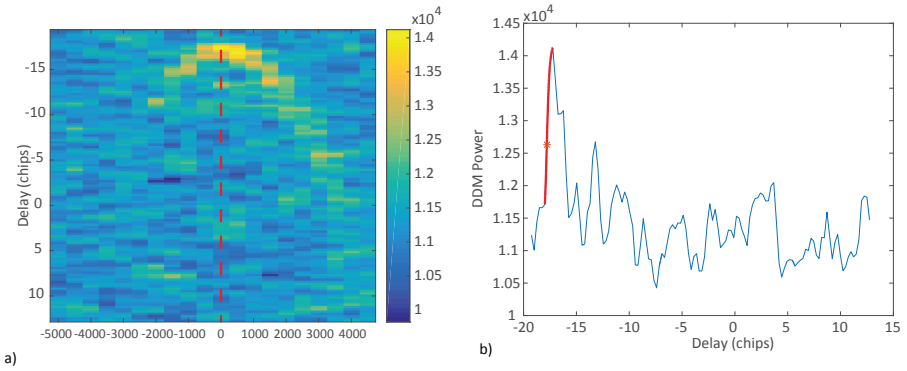

Figure A.4: Method used to find delay estimate. The waveform in the delay domain is found at the maximum power (red dashed line, a)). b) The leading edge is then found (red) and the delay selected at its maximum first-order derivative(star).

Tables A.1-A.3 - Error associated with different delay estimates

Tables A.1-A.3 displays the error seen when the maximum derivative of the leading edge is used to estimate the delay input, compared to the maximum power across three different comparison DEMs. Glacial ice yields a less specular return than sea ice, as can be seen by the wider spread of power in the Doppler domain in the DDMs. Therefore tracking the leading edge (as performed in this study) should lead to more accurate height estimates in this case, whereas the maximum power is more appropriate for sea ice reflections.

Table A.1: Error from CryoSat-2 DEM 1 km v1.0 shown in metres where TDS-1 data is filtered by incidence angle and heights calculated through two different algorithms. Errors are computed through interpolation of the CryoSat-2 DEM to the location of the TechDemoSat-1 measurement.

	Delay at maximum first-order derivative of leading edge	Delay at peak of waveform
Median difference (m)	17.9445	-50.5078
Mean difference (m)	14.9538	-56.8809
RMS difference (m)	90.6924	100.7172

Table A.2: Error from *Bamber et al.* (2009) DEM shown in metres where TDS-1 data is filtered by incidence angle and heights calculated through two different algorithms. Errors are computed through interpolation of the *Bamber et al.* (2009) DEM to the location of the TechDemoSat-1 measurement.

	Delay at maximum first-order derivative of leading edge	Delay at peak of waveform
Median difference (m)	18.7009	-49.6423
Mean difference (m)	19.3708	-53.5562
RMS difference (m)	79.8821	92.4091

Table A.3: Error from Bedmap2 DEM (*Fretwell et al.*, 2013) shown in metres where TDS-1 data is filtered by incidence angle and heights calculated through two different algorithms. Errors are computed through interpolation of the Bedmap2 DEM to the location of the TechDemoSat-1 measurement.

	Delay at maximum first-order derivative of leading edge	Delay at peak of waveform
Median difference (m)	19.2476	48.7361
Mean difference (m)	19.5072	-52.9541
RMS difference (m)	83.0065	93.7287

Tables A.4-A.6 - Gridded Error at different resolutions

Tables A.4-A.6 displays the gridded error seen when the DEM is created at different resolutions across three different comparison DEMs. This is computed on a pixel-by-pixel difference where both datasets are gridded to the same resolution and spatial extent. Error is also shown where TechDemoSat-1 estimates are compared to co-located values through interpolation.

Table A.4: Error from CryoSat-2 DEM v1.2 shown in metres where data is filtered by incidence angle and gridded at different resolutions.

	Gridded Error			
	20 km	50 km	100 km	Interpolated Error
Median difference (m)	7.9736	-3.2691	-20.2423	17.9445
Mean difference (m)	-21.4784	-53.3776	-91.1988	14.9538
RMS difference (m)	167.2248	227.3274	303.7098	90.6924

Table A.5: Error from *Bamber et al.* (2009) DEM shown in metres where data is filtered by incidence angle and gridded at different resolutions.

	Gridded Error			
	20 km	50 km	100 km	Interpolated Error
Median difference (m)	8.7228	-2.0536	-18.1112	18.7009
Mean difference (m)	-9.353	-38.1401	-72.4544	19.3708
RMS difference (m)	139.4277	197.1591	271.009	79.8821

Table A.6: Error from Bedmap2 DEM (*Fretwell et al.*, 2013) shown in metres where data is filtered by incidence angle and gridded at different resolutions.

	Gridded Error			
	20 km	50 km	100 km	Interpolated Error
Median difference (m)	-10.4105	0.057084	-14.5118	19.2476
Mean difference (m)	-9.3974	-39.0858	-72.7809	19.5072
RMS difference (m)	146.3334	204.05	275.5965	83.0065

Tables A.7-A.9 - Error associated with different surface gradients

Tables A.7-A.9 displays the error grouped by angle of slope across three different comparison DEMs. It can be seen that the error increases where slopes are steeper, with the majority of the estimates considered under 0.25°. These are computed through the interpolation of the comparison DEM to the location of the TechDemoSat-1 measurement.

Table A.7: Error from CryoSat-2 DEM v1.2 shown in metres where TDS-1 data is filtered by incidence angle and taken at different slope ranges.

Slope Range (degrees)	Median difference (m)	Mean difference (m)	RMS difference (m)	% of total samples
0.00-0.25	13.8755	15.0555	68.0548	55.50
0.25-0.50	20.7279	21.1063	73.0058	23.47
0.50-0.75	29.4786	29.1335	82.7601	9.27
0.75 - 1.00	37.5997	34.2113	96.7641	4.11
¿ 1.00	15.5318	-28.0366	207.277	7.65

Table A.8: Error from *Bamber et al.* (2009) DEM shown in metres where TDS-1 data is filtered by incidence angle and taken at different slope ranges.

Slope Range (degrees)	Median difference (m)	Mean difference (m)	RMS difference (m)	% of total samples
0.00-0.25	17.2719	18.0163	78.041	72.25
0.25-0.50	14.2266	16.5644	72.8216	13.61
0.50-0.75	15.3553	17.8014	73.8624	5.60
0.75 - 1.00	18.2334	20.0217	80.1025	2.62
¿ 1.00	20.9096	21.4762	76.7066	5.92

Table A.9: Error from Bedmap2 DEM (*Fretwell et al.*, 2013) shown in metres where TDS-1 data is filtered by incidence angle and taken at different slope ranges.

Slope Range (degrees)	Median difference (m)	Mean difference (m)	RMS difference (m)	% of total samples
0.00-0.25	17.6309	18.2602	78.673	74.54
0.25-0.50	15.8432	18.0902	77.3896	12.66
0.50-0.75	17.1584	19.7322	76.432	5.44
0.75 - 1.00	19.7569	20.9792	70.9706	2.48
¿ 1.00	19.8378	20.8193	74.1651	4.88

Appendix B

Appendix - "Improved GNSS-R bi-static altimetry and independent DEMs of Greenland and Antarctica from TechDemoSat-1"

Contents

Table B.1: Difference from *Slater et al.* (2018) DEM (top, Antarctic) and ESA CCI DEM (below, Greenland) shown in metres at different slope ranges. TechDemoSat-1 data produced according to methods in paper.

Antarctic				
Slope Range (degrees)	Median difference (m)	Mean difference (m)	RMS Errors (m)	% of total samples
0.00-0.25	8.35	8.12	36.90	55.52
0.25-0.50	10.26	9.17	43.42	23.02
0.50-0.75	16.64	18.22	58.71	9.30
0.75-1.00	19.19	24.95	76.00	4.24
>1.00	-27.96	14.38	176.34	7.92
Greenland				
Slope Range (degrees)	Median difference (m)	Mean difference (m)	RMS Errors (m)	% of total samples
0.00-0.25	9.26	9.22	30.07	66.83
0.25-0.50	30.93	34.91	66.45	11.43
0.50-0.75	39.32	41.15	102.35	3.20
0.75-1.00	38.87	28.77	131.29	2.00
>1.00	-92.98	-190.10	391.28	16.54

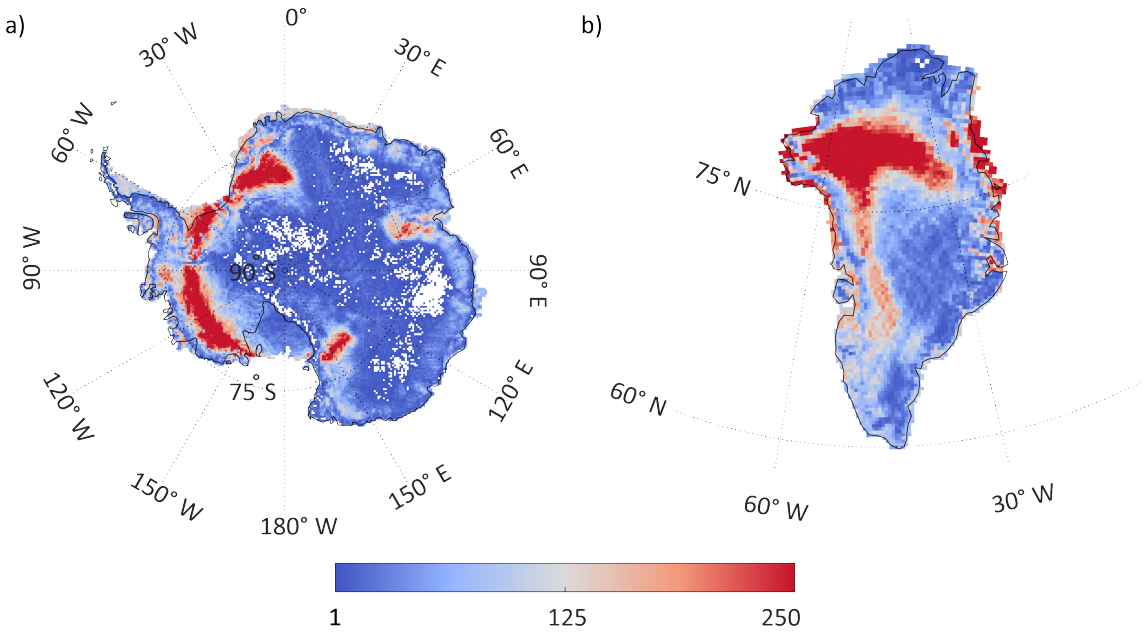

Figure B.1: Counts of measurements per 25 km grid cell over Antarctica (left) and Greenland (right).

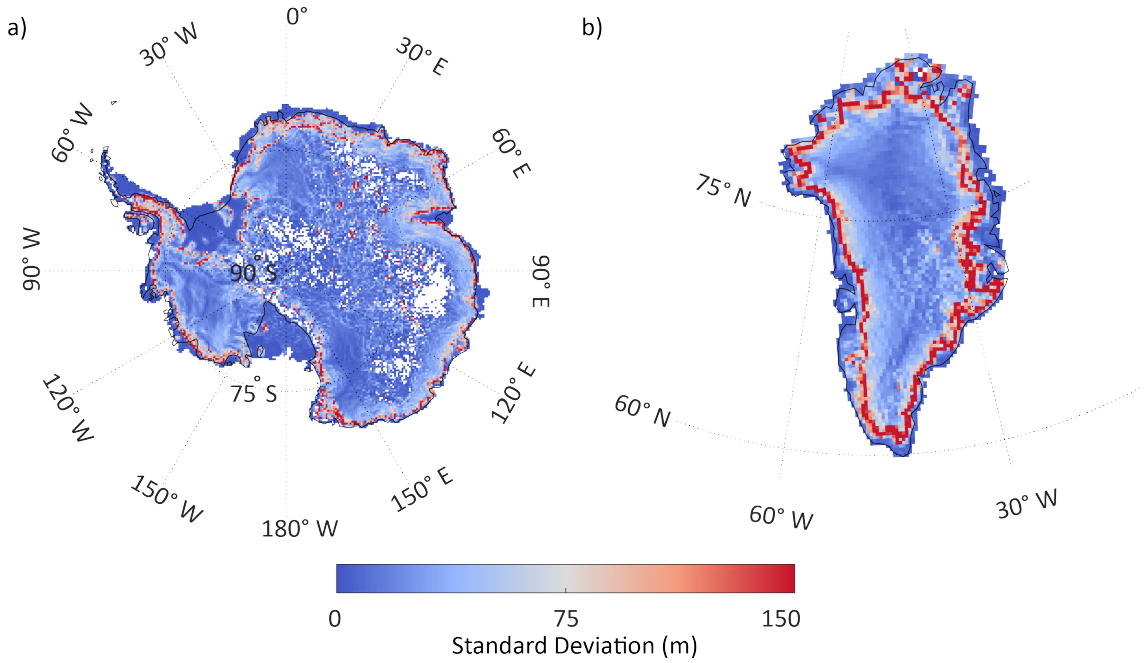

Figure B.2: Standard deviation of measurements in metres per 25 km grid cell over Antarctica (left) and Greenland (right).

Appendix C

Appendix - Sea ice detection using GNSS-R data from TechDemoSat-1

Contents

Text 1 - Summary of appendix

Figure C.1 displays the results when any two were used in combination, and Table C.1 the key to Figure C.1. Videos below are also available for separate download from the Journal of Geophysical Research: Oceans paper supplementary information. These show mapped comparisons of the datasets with the TechDemoSat-1 ice detection retrieval method described in Chapter 5.

C 1 ESA CCI

(a) Download Arctic video

(b) Download Antarctic video

C 2 OSI SAF

(a) Download Arctic video

(b) Download Antarctic video

C 3 MASIE Download Arctic video

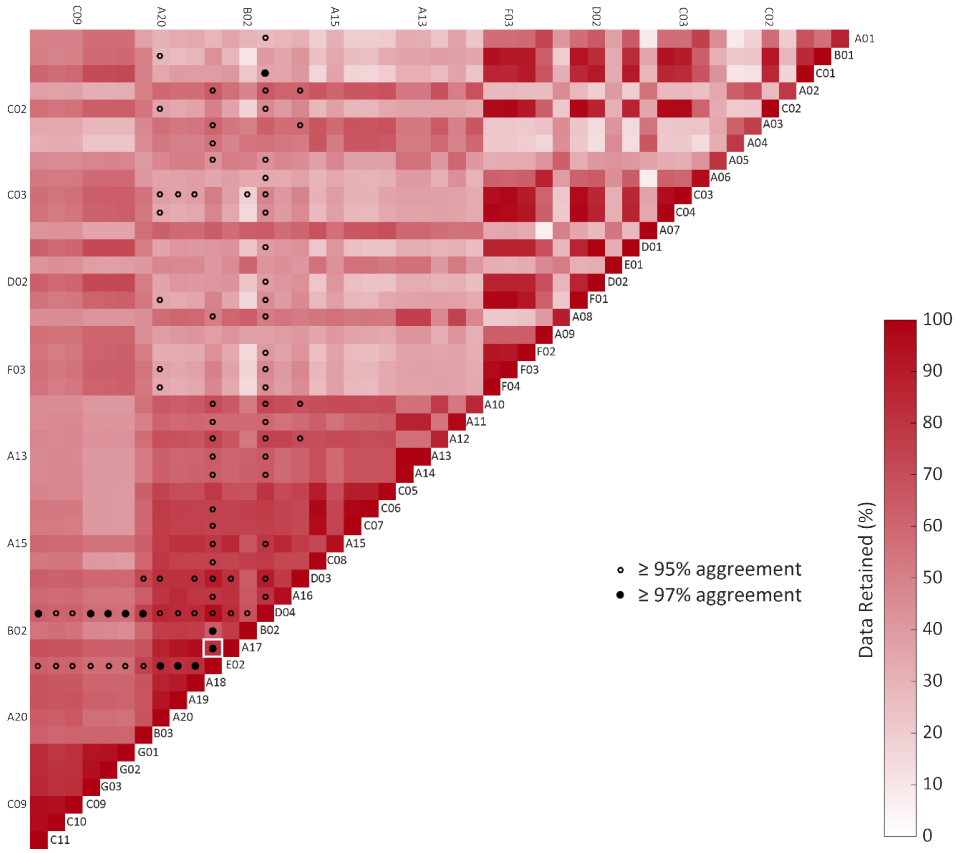

Figure C.1: Derived parameters used to detect sea ice. The shading scale shows percentage of valid data left when this combination is used from 0% (white) to 100% (solid red). After data filters, valid data for such applications is reduced to 46% of the entire dataset. As such this is represented by 100% here The diagonal shows the result where that parameter is used on its own, and may be less than 100% due to the inapplicability of some methods to individual DDMs – for example, where the power of the waveform does not decrease to the chosen percentage of the maximum. Labels represent the variables used as seen in Table SC.1. Hollow and filled dots respectively denote agreement of 95% and 97% or greater with the ESA CCI ice concentration product (where 'ice' is anything higher than 0% concentration) (*Toudal Pedersen et al.*, 2017). These statistics represent an average for both hemispheres. The white box denotes the best performing combination (OCOG and dy_{down} – to 85% of maximum amplitude) as used in this study.

Table C.1: Variables in Figure SC.1 grouped as in the methodology below. Percentages in brackets denote the percentage to which the maximum amplitude was reduced at this change in x or y. Size of signal box brackets denote the number of Doppler and delay bins respectively. For example, 20 x 3 shows all 20 Doppler bins used and the 3 delay bins surrounding the maximum amplitude.

A01	dx_{left} (65%)	A13	dy_{up} (85%)
B01	Maximum Power	A14	dy_{up} (95%)
C01	$DDMA_{mean}$ (20 x 3)	C05	$DDMA_{percentage}$ (20x3)
A02	dx_{right} (55%)	C06	$DDMA_{mean}$ (5x3)
C02	$DDMA_{percentage}$ (5x3)	C07	$DDMA_{mean}$ (7x3)
A03	dy_{down} (55%)	A15	dy_{down} (75%)
A04	dx_{left} (55%)	C08	$DDMA_{mean}$ (3x3)
A05	dy_{up} (55%)	D03	κ_{DelIW}
A06	dx_{left} (75%)	A16	dx_{right} (75%)
C03	$DDMA_{percentage}$ (7x3)	D04	κ_{DopIW}
C04	$DDMA_{percentage}$ (3x3)	B02	SNR
A07	dx_{left} (95%)	A17	dy_{down} (85%)
D01	κ_{DDM}	E02	$OCOG$
E01	$OCOG_{DopIW}$	A18	dy_{down} (95%)
D02	$\kappa_{waveform}$	A19	dx_{right} (85%)
F01	$DDMS$ (5x3)	A20	dx_{right} (95%)
A08	dy_{up} (65%)	B03	Noise Floor
A09	dx_{left} (85%)	G01	TES_{3-bin}
F02	$DDMS$ (20x3)	G02	TES_{6-bin}
F03	$DDMS$ (7x3)	G03	TES_{9-bin}
F04	$DDMS$ (3x3)	C09	$DDMA_{median}$ (3x3)
A10	dy_{down} (65%)	C10	$DDMA_{median}$ (7x3)
A11	dy_{up} (75%)	C11	$DDMA_{median}$ (5x3)
A12	dx_{right} (65%)		

Table C.2: Percentage agreements of the TechDemoSat-1 assignments against different 'truth' datasets. Methods and parameters used for assignment from the GNSS-R data are those reported in the main paper, trained on the CCI sea ice concentration data. Results have been validated across the whole dataset as well as exclusively within 200 km of the ice edge.

	Entire dataset		Within 200 km of the ice edge	
	Antarctic	Arctic	Antarctic	Arctic
CCI sea ice concentration (*Toudal Pedersen et al.*, 2017)	98.4%	96.6%	94.7%	94.5%
NSIDC sea ice concentration (*Cavalieri et al.*, 1996)	98%	95.9%	93.6%	92.2%
OSI SAF ice edge (*Breivik et al.*, 2012)	97.1%	94.0%	89.5%	85.9%
MASIE operational product (*Fetterer et al.*, 2010)	-	95.5%	-	90.3%

Acronyms

AMSR2 Advanced Microwave Scanning Radiometer-2.

ASCAT Advanced Scatterometer.

ATM Airborne Topographic Mapper.

AVHRR Advanced Very High Resolution Radiometer.

CCI Climate Change Initiative.

CYGNSS Cyclone GNSS.

DDM delay-Doppler Map.

DEM Digital Elevation Model.

DMSP Defence Meteorological Satellite Program.

ESA European Space Agency.

GIMP Greenland Ice-Sheet Mapping Project.

GNSS Global Navigation Satellite Systems.

GNSS-R Global Navigation Satellite Systems-Reflectometry.

GPS Global Positioning System.

InSAR Interferometric Synthetic Aperture Radar.

IPCC Intergovernmental Panel on Climate Change.

MASIE-NH Multi-Sensor Analyzed Sea Ice Extent - Northern Hemisphere.

MODIS Moderate Resolution Imaging Spectroradiometer.

NASA National Aeronautics and Space Administration.

NSIDC National Snow and Ice Data Centre.

OCOG Offset Centre of Gravity.

OSI SAF Ocean Sea Ice Satellite Application Facility.

PRN Pseudo-Random Noise.

RMS Root Mean Squared.

RO Radio Occultation.

SAR Synthetic Aperture Radar.

SGR-ReSI Space GNSS Receiver - Remote Sensing Instrument.

SIRAL Synthetic Interferometric Radar Altimeter.

SMMR Scanning Multichannel Microwave Radiometer.

SMOS Soil Moisture and Ocean Salinity.

SSMIS Special Sensor Microwave Imager / Sounder.

SSTL Surrey Satellite Technology Ltd.

TDS-1 TechDemoSat-1.

Bibliography

Adusumilli, S., H. A. Fricker, M. R. Siegfried, L. Padman, F. S. Paolo, and S. R. M. Ligtenberg, Variable Basal Melt Rates of Antarctic Peninsula Ice Shelves, 1994-2016, *Geophysical Research Letters*, *45*(9), 4086–4095, doi: 10.1002/2017gl076652, 2018.

Alonso-Arroyo, A., V. U. Zavorotny, and A. Camps, Sea Ice Detection Using U.K. TDS-1 GNSS-R Data, *IEEE Transactions on Geoscience and Remote Sensing*, *55*(9), 4989–5001, doi: 10.1109/tgrs.2017.2699122, 2017.

Bamber, J. L., Greenland 5 km DEM, Ice Thickness and Bedrock Elevation Grids, NASA National Snow and Ice Data Center Distributed Active Archive Center, Boulder, Colorado USA, doi: 10.5067/01A10Z9BM7KP, 2001.

Bamber, J. L., J. L. Gomez-Dans, and J. A. Griggs, A new 1 km digital elevation model of the Antarctic derived from combined satellite radar and laser data – Part 1: Data and methods, *The Cryosphere*, *3*(1), 101–111, doi: 10.5194/tc-3-101-2009, 2009.

Bi, H., X. Yang, Z. Li, and X. Zhou, Sea ice small-scale surface roughness estimation based on AMSR-E observations, *International Journal of Remote Sensing*, *34*(12), 4425–4448, 2013.

Bird, K. J., et al., Circum-arctic resource appraisal: Estimates of undiscovered oil and gas north of the Arctic Circle, doi: 10.3133/fs20083049, 2008.

Breivik, L.-A., S. Eastwood, and T. Lavergne, Use of C-Band Scatterometer for Sea Ice Edge Identification, *IEEE Transactions on Geoscience and Remote Sensing*, *50*(7), 2669–2677, doi: 10.1109/tgrs.2012.2188898, 2012.

Brooks, R. L., W. J. Campbell, R. O. Ramseier, H. R. Stanley, and H. J. Zwally, Ice sheet topography by satellite altimetry, *Nature*, *274*(5671), 539–543, doi: 10.1038/274539a0, 1978.

Brucker, L., E. P. Dinnat, G. Picard, and N. Champollion, Effect of Snow Surface Metamorphism on Aquarius L-Band Radiometer Observations at Dome C, Antarctica, *IEEE Transactions on Geoscience and Remote Sensing*, *52*(11), 7408–7417, doi: 10.1109/tgrs.2014.2312102, 2014.

Budd, W. F., Antarctica and global change, *Climatic Change*, *18*(2-3), 271–299, 1991.

Budikova, D., Role of Arctic sea ice in global atmospheric circulation: A review, *Global and Planetary Change*, *68*(3), 149–163, 2009.

Cardellach, E., C. O. Ao, M. de la Torre Juárez, and G. A. Hajj, Carrier phase delay altimetry with GPS-reflection/occultation interferometry from low Earth orbiters, *Geophysical Research Letters*, *31*(10), n/a–n/a, doi: 10.1029/2004gl019775, 2004.

Cardellach, E., F. Fabra, A. Rius, S. Pettinato, and S. D'Addio, Characterization of dry-snow sub-structure using GNSS reflected signals, *Remote Sensing of Environment*, *124*, 122–134, doi: 10.1016/j.rse.2012.05.012, 2012.

Cardellach, E., A. Rius, M. Martin-Neira, F. Fabra, O. Nogues-Correig, S. Ribo, J. Kainulainen, A. Camps, and S. D'Addio, Consolidating the Precision of Interferometric GNSS-R Ocean Altimetry Using Airborne Experimental Data, *IEEE Transactions on Geoscience and Remote Sensing*, *52*(8), 4992–5004, doi: 10.1109/tgrs.2013.2286257, 2014.

Cardellach, E., et al., GNSS Transpolar Earth Reflectometry exploriNg System (G-TERN): Mission Concept, *IEEE Access*, *6*, 13,980–14,018, doi: 10.1109/ACCESS.2018.2814072, 2018.

Carnat, G., T. Papakyriakou, N. X. Geilfus, F. Brabant, B. Delille, M. Vancoppenolle, G. Gilson, J. Zhou, and J.-L. Tison, Investigations on physical and textural properties of Arctic first-year sea ice in the Amundsen Gulf, Canada, November 2007–June 2008 (IPY-CFL system study), *Journal of Glaciology*, *59*(217), 819–837, 2013.

Cartwright, J., Independent Digital Elevation Model of Antarctica from GNSS-R data from TechDemoSat-1 - VERSION 2.0 , UK Polar Data Centre, doi: 10.5285/C7A6D602-AB52-4F3C-90A4-42D0CD9F62D3, 2020a.

Cartwright, J., Independent Digital Elevation Model of Greenland from GNSS-R data from TechDemoSat-1, UK Polar Data Centre, doi: 10.5285/783515B1-AC01-4615-A24C-629FE37A63A2, 2020b.

Cartwright, J., M. P. Clarizia, P. Cipollini, C. Banks, and M. Srokosz, Independent DEM of Antarctica using GNSS-R data from TechDemoSat-1, *Geophysical Research Letters*, *45*(12), 6117–6123, doi: 10.1029/2018gl077429, 2018.

Cartwright, J., C. J. Banks, and M. Srokosz, Sea Ice Detection Using GNSS-R Data From TechDemoSat-1, *Journal of Geophysical Research: Oceans*, *124*(8), 5801–5810, doi: 10.1029/2019jc015327, 2019.

Cartwright, J., C. J. Banks, and M. Srokosz, Improved GNSS-R bi-static altimetry and independent digital elevation models of Greenland and Antarctica from TechDemoSat-1, *The Cryosphere*, *14*(6), 1909–1917, doi: 10.5194/tc-14-1909-2020, 2020.

Cavalieri, D., C. Parkinson, P. Gloersen, and H. Zwally, Sea Ice Concentrations from Nimbus-7 SMMR and DMSP SSM/I-SSMIS Passive Microwave Data, Version 1.1, NASA National Snow and Ice Data Center Distributed Active Archive Center, Boulder, Colorado USA, doi: 10.5067/8GQ8LZQVL0VL, 1996.

Chew, C., R. Shah, C. Zuffada, G. Hajj, D. Masters, and A. J. Mannucci, Demonstrating soil moisture remote sensing with observations from the UK TechDemoSat-1 satellite mission, *Geophysical Research Letters*, *43*(7), 3317–3324, 2016.

Clarizia, M. P., and C. S. Ruf, Wind Speed Retrieval Algorithm for the Cyclone Global Navigation Satellite System (CYGNSS) Mission, *IEEE Transactions on Geoscience and Remote Sensing*, *54*(8), 4419–4432, doi: 10.1109/tgrs.2016.2541343, 2016.

Clarizia, M. P., C. S. Ruf, P. Jales, and C. Gommenginger, Spaceborne GNSS-R Minimum Variance Wind Speed Estimator, *IEEE Transactions on Geoscience and Remote Sensing*, *52*(11), 6829–6843, doi: 10.1109/tgrs.2014.2303831, 2014.

Clarizia, M. P., C. S. Ruf, P. Cipollini, and C. Zuffada, First spaceborne observation of sea surface height using GPS Reflectometry, *Geophysical Research Letters*, *43*(2), 767–774, doi: 10.1002/2015GL066624., 2016.

Comiso, J. C., D. J. Cavalieri, and T. Markus, Sea ice concentration, ice temperature, and snow depth using AMSR-E data, *IEEE Transactions on Geoscience and Remote Sensing*, *41*(2), 243–252, 2003.

DeConto, R. M., and D. Pollard, Contribution of Antarctica to past and future sea-level rise, *Nature*, *531*(7596), 591–7, doi: 10.1038/nature17145, 2016.

Dow, C. F., W. S. Lee, J. S. Greenbaum, C. A. Greene, D. D. Blankenship, K. Poinar, A. L. Forrest, D. A. Young, and C. J. Zappa, Basal channels drive active surface hydrology and transverse ice shelf fracture, *Sci Adv*, *4*(6), eaao7212, doi: 10.1126/sciadv.aao7212, 2018.

Drinkwater, M. R., R. Hosseinmostafa, and P. Gogineni, C-band backscatter measurements of winter sea-ice in the Weddell Sea, Antarctica, *International Journal of Remote Sensing*, *16*(17), 3365–3389, doi: 10.1080/01431169508954635, 1995.

Eicken, H., Salinity profiles of Antarctic Sea ice- Field data and model results, *Journal of Geophysical Research*, *97*(C10), 15,545–15,557, 1992.

Fabra, F., E. Cardellach, A. Rius, S. Ribo, S. Oliveras, O. Nogues-Correig, M. Belmonte Rivas, M. Semmling, and S. D'Addio, Phase Altimetry With Dual Polarization GNSS-R Over Sea Ice, *IEEE Transactions on Geoscience and Remote Sensing*, *50*(6), 2112–2121, doi: 10.1109/tgrs.2011.2172797, 2012.

Fetterer, F., M. Savoie, S. Helfrich, and P. Clemente-Colón, Multisensor Analyzed Sea Ice Extent - Northern Hemisphere (MASIE-NH), 1 ed., NSIDC, doi: 10.7265/N5GT5K3K, 2010.

Fleury, Polar Altimetry Gap Letter of Concern [open letter], 2020.

Foti, G., C. Gommenginger, P. Jales, M. Unwin, A. Shaw, C. Robertson, and J. Roselló, Spaceborne GNSS reflectometry for ocean winds: First results from the UK TechDemoSat-1 mission, *Geophysical Research Letters*, *42*(13), 5435–5441, doi: 10.1002/2015gl064204, 2015.

Foti, G., C. Gommenginger, M. Unwin, P. Jales, J. Tye, and J. Rosello, An Assessment of Non-geophysical Effects in Spaceborne GNSS Reflectometry Data From the UK TechDemoSat-1 Mission, *IEEE Journal of Selected Topics in Applied Earth Observations and Remote Sensing*, *10*(7), 3418–3429, doi: 10.1109/jstars.2017.2674305, 2017.

Fraser, A. D., N. W. Young, and N. Adams, Comparison of Microwave Backscatter Anisotropy Parameterizations of the Antarctic Ice Sheet Using ASCAT, *IEEE Transactions on Geoscience and Remote Sensing*, *52*(3), 1583–1595, doi: 10.1109/tgrs.2013.2252621, 2014.

Fraser, A. D., et al., Drivers of ASCAT C band backscatter variability in the dry snow zone of Antarctica, *Journal of Glaciology*, *62*(231), 170–184, doi: 10.1017/jog.2016.29, 2016.

Fretwell, P., et al., Bedmap2: improved ice bed, surface and thickness datasets for Antarctica, 2013.

Giles, K. A., S. W. Laxon, D. J. Wingham, D. W. Wallis, W. B. Krabill, C. J. Leuschen, D. McAdoo, S. S. Manizade, and R. K. Raney, Combined airborne laser and radar altimeter measurements over the Fram Strait in May 2002, *Remote Sensing of Environment*, *111*(2-3), 182–194, doi: 10.1016/j.rse.2007.02.037, 2007.

Gleason, S., Remote Sensing of Ocean, Ice and Land Surfaces Using Bistatically Scattered GNSS Signals From Low Earth Orbit, Thesis, 2006.

Gleason, S., C. S. Ruf, M. P. Clarizia, and A. J. O'Brien, Calibration and Unwrapping of the Normalized Scattering Cross Section for the Cyclone Global Navigation Satellite System, *IEEE Transactions on Geoscience and Remote Sensing*, *54*(5), 2495–2509, doi: 10.1109/tgrs.2015.2502245, 2016.

Griggs, J. A., and J. L. Bamber, A new 1 km digital elevation model of Antarctica derived from combined radar and laser data-Part 2: Validation and error estimates, *The Cryosphere*, *3*(1), 113, 2009.

Hajj, G. A., and C. Zuffada, Theoretical description of a bistatic system for ocean altimetry using the GPS signal, *Radio Science*, *38*(5), n/a–n/a, doi: 10.1029/2002rs002787, 2003.

Hall, C. D., and R. A. Cordey, Multistatic Scatterometry, pp. 561–562, 1988.

Hong, S., Detection of small-scale roughness and refractive index of sea ice in passive satellite microwave remote sensing, *Remote Sensing of Environment*, *114*(5), 1136–1140, 2010.

Hoque, M. M., and N. Jakowski, Ionospheric propagation effects on GNSS signals and new correction approaches, *Global Navigation Satellite Systems: Signal, Theory and Applications*, pp. 381–405, 2012.

Howat, I. M., A. Negrete, and B. E. Smith, The Greenland Ice Mapping Project (GIMP) land classification and surface elevation data sets, *The Cryosphere*, *8*(4), 1509–1518, doi: 10.5194/tc-8-1509-2014, 2014.

Hu, C., C. Benson, C. Rizos, and L. Qiao, Single-Pass Sub-Meter Space-Based GNSS-R Ice Altimetry: Results From TDS-1, *IEEE Journal of Selected Topics in Applied Earth Observations and Remote Sensing*, *10*(8), 3782–3788, doi: 10.1109/jstars.2017.2690917, 2017.

Ivanova, N., O. M. Johannessen, L. T. Pedersen, and R. T. Tonboe, Retrieval of Arctic Sea Ice Parameters by Satellite Passive Microwave Sensors: A Comparison of Eleven Sea Ice Concentration Algorithms, *IEEE Transactions on Geoscience and Remote Sensing*, *52*(11), 7233–7246, 2014.

Jales, P., and M. Unwin, Mission description-GNSS reflectometry on TDS-1 with the SGR-ReSI, *Surrey Satellite Technol. Ltd., Guildford, UK, Tech. Rep. SSTL Rep*, *248367*, 2015.

Kaleschke, L., X. Tian-Kunze, N. Maaß, M. Mäkynen, and M. Drusch, Sea ice thickness retrieval from SMOS brightness temperatures during the Arctic freeze-up period, *Geophysical Research Letters*, *39*(5), 2012.

Khazendar, A., E. Rignot, D. M. Schroeder, H. Seroussi, M. P. Schodlok, B. Scheuchl, J. Mouginot, T. C. Sutterley, and I. Velicogna, Rapid submarine ice melting in the grounding zones of ice shelves in West Antarctica, *Nat Commun*, *7*, 13,243, doi: 10.1038/ncomms13243, 2016.

Komjathy, A., J. Maslanik, V. U. Zavorotny, P. Axelrad, and S. J. Katzberg, Sea ice remote sensing using surface reflected GPS signals, in *Geoscience and Remote Sensing Symposium, 2000. Proceedings. IGARSS 2000. IEEE 2000 International*, vol. 7, pp. 2855–2857 vol.7–2857 vol.7, 2000.

Kwok, R., Declassified high-resolution visible imagery for Arctic sea ice investigations: An overview, *Remote Sensing of Environment*, *142*, 44–56, 2014.

Lange, M. A., S. F. Ackley, P. Wadhams, G. S. Dieckmann, and H. Eicken, Development of sea ice in the Weddell Sea, *Ann. Glaciol*, *12*, 92–96, 1989.

Leduc-Leballeur, M., G. Picard, G. Macelloni, L. Arnaud, M. Brogioni, A. Mialon, and Y. H. Kerr, Influence of snow surface properties on L-band brightness temperature at Dome C, Antarctica, *Remote Sensing of Environment*, *199*, 427–436, doi: 10.1016/j.rse.2017.07.035, 2017.

Lee, M., C. Hong, and H. Hsu, Compounding effects of warm sea surface temperature and reduced sea ice on the extreme circulation over the extratropical North Pacific and North America during the 2013–2014 boreal winter, *Geophysical Research Letters*, *42*(5), 1612–1618, doi: 10.1002/2014gl062956, 2015.

Lenaerts, J. T. M., B. Medley, M. R. van den Broeke, and B. Wouters, Observing and Modeling Ice Sheet Surface Mass Balance, *Rev Geophys*, *57*(2), 376–420, doi: 10.1029/2018RG000622, 2019.

Li, W., E. Cardellach, F. Fabra, A. Rius, S. Ribó, and M. Martín-Neira, First spaceborne phase altimetry over sea ice using TechDemoSat-1 GNSS-R signals, *Geophysical Research Letters*, *44*(16), 8369–8376, doi: 10.1002/2017gl074513, 2017.

Lomax, A. S., D. Lubin, and R. H. Whritner, The potential for interpreting total and multiyear ice concentrations in SSM/I 85.5 GHz imagery, *Remote Sensing of Environment*, *54*(1), 13–26, 1995.

Lowe, S. T., J. L. LaBrecque, C. Zuffada, L. J. Romans, L. E. Young, and G. A. Hajj, First spaceborne observation of an Earth-reflected GPS signal, *Radio Science*, *37*(1), 7–1–7–28, doi: 10.1029/2000rs002539, 2002.

Lythe, M. B., and D. G. Vaughan, BEDMAP: A new ice thickness and subglacial topographic model of Antarctica, *Journal of Geophysical Research: Solid Earth*, *106*(B6), 11,335–11,351, doi: 10.1029/2000jb900449, 2001.

Macelloni, G., M. Leduc-Leballeur, M. Brogioni, C. Ritz, and G. Picard, Analyzing and modeling the SMOS spatial variations in the East Antarctic Plateau, *Remote Sensing of Environment*, *180*, 193–204, doi: 10.1016/j.rse.2016.02.037, 2016.

MacGregor, J. A., D. P. Winebrenner, H. Conway, K. Matsuoka, P. A. Mayewski, and G. D. Clow, Modeling englacial radar attenuation at Siple Dome, West Antarctica, using ice chemistry and temperature data, *Journal of Geophysical Research*, *112*(F3), 2007.

Manninen, A. T., Surface roughness of Baltic sea ice, *Journal of Geophysical Research: Oceans*, *102*(C1), 1119–1139, 1997.

Marchan-Hernandez, J. F., E. Valencia, N. Rodriguez-Alvarez, I. Ramos-Perez, X. Bosch-Lluis, A. Camps, F. Eugenio, and J. Marcello, Sea-State Determination Using GNSS-R Data, *IEEE Geoscience and Remote Sensing Letters*, *7*(4), 621–625, doi: 10.1109/lgrs.2010.2043213, 2010.

Markus, T., and D. J. Cavalieri, An enhancement of the NASA Team sea ice algorithm, *IEEE Transactions on Geoscience and Remote Sensing*, *38*(3), 1387–1398, 2000.

Marshak, S., and J. Repcheck, *Essentials of geology*, WW Norton, 2016.

Martin-Neira, M., S. D'Addio, C. Buck, N. Floury, and R. Prieto-Cerdeira, The PARIS Ocean Altimeter In-Orbit Demonstrator, *IEEE Transactions on Geoscience and Remote Sensing*, *49*(6), 2209–2237, doi: 10.1109/tgrs.2010.2092431, 2011.

Martín-Neira, M., A passive reflectometry and interferometry system (PARIS): Application to ocean altimetry, *ESA journal*, *17*(4), 331–355, 1993.

Mashburn, J., P. Axelrad, S. T. Lowe, and K. M. Larson, An Assessment of the Precision and Accuracy of Altimetry Retrievals for a Monterey Bay GNSS-R Experiment, *IEEE Journal of Selected Topics in Applied Earth Observations and Remote Sensing*, *9*(10), 4660–4668, doi: 10.1109/jstars.2016.2537698, 2016.

Massom, R. A., et al., Snow on Antarctic sea ice, *Reviews of Geophysics*, *39*, 413–445, 2001.

Masters, D., V. Zavorotny, S. Katzberg, and W. Emery, GPS signal scattering from land for moisture content determination, in *Geoscience and Remote Sensing Symposium, 2000. Proceedings. IGARSS 2000. IEEE 2000 International*, vol. 7, pp. 3090–3092 vol.7–3092 vol.7, 2000.

Maykut, G. A., *The ice environment*, Department of Atmospheric Sciences/Geophysics Program, University of Washington, 1985.

Maykut, G. A., and N. Untersteiner, Some results from a time-dependent thermodynamic model of sea ice, *Journal of Geophysical Research*, *76*(6), 1550–1575, doi: 10.1029/JC076i006p01550, 1971.

McCartney, M. S., and L. D. Talley, Warm-to-Cold Water Conversion in the Northern North Atlantic Ocean, *Journal of Physical Oceanography*, *14*(5), 922–935, doi: 10.1175/1520-0485(1984)014⟨0922:Wtcwci⟩2.0.Co;2, 1984.

Mecklenburg, S., et al., ESA's Soil Moisture and Ocean Salinity mission: From science to operational applications, *Remote Sensing of Environment*, *180*, 3–18, 2016.

Meier, M. F., Hydraulics and hydrology of glaciers, *IAHS Publ*, *107*, 353–370, 1973.

Mätzler, C., Applications of SMOS over terrestrial ice and snow, pp. 10–12, 2001.

O'Leary, M., and P. Christoffersen, Calving on tidewater glaciers amplified by submarine frontal melting, *The Cryosphere*, *7*(1), 119–128, doi: 10.5194/tc-7-119-2013, 2013.

OSI SAF, Sea ice edge product of the EUMETSAT Ocean and Sea Ice Satellite Application Facility, 2019a.

OSI SAF, Sea ice type product of the EUMETSAT Ocean and Sea Ice Satellite Application Facility, 2019b.

Passalacqua, O., G. Picard, C. Ritz, M. Leduc-Leballeur, A. Quiquet, F. Larue, and G. Macelloni, Retrieval of the Absorption Coefficient of L-Band Radiation in Antarctica From SMOS Observations, *Remote Sensing*, *10*(12), doi: 10.3390/rs10121954, 2018.

Phalippou, L., L. Rey, and P. de Chateau-Thierry, Overview of the performances and tracking design of the SIRAL altimeter for the CryoSat mission, *Geoscience and Remote Sensing Symposium, 2001. IGARSS 01. IEEE 2001 International*, *5*, 2025–2027, 2001.

Pörtner, H., et al., IPCC Special Report on the Ocean and Cryosphere in a Changing Climate, *IPCC Intergovernmental Panel on Climate Change: Geneva, Switzerland*, 2019.

Rignot, E., K. Echelmeyer, and W. Krabill, Penetration depth of interferometric synthetic-aperture radar signals in snow and ice, *Geophysical Research Letters*, *28*(18), 3501–3504, doi: 10.1029/2000gl012484, 2001.

Rius, A., E. Cardellach, F. Fabra, W. Li, S. Ribó, and M. Hernández-Pajares, Feasibility of GNSS-R Ice Sheet Altimetry in Greenland Using TDS-1, *Remote Sensing*, *9*(7), 742, doi: 10.3390/rs9070742, 2017.

Rivas, M. B., J. A. Maslanik, and P. Axelrad, Bistatic Scattering of GPS Signals Off Arctic Sea Ice, *IEEE Transactions on Geoscience and Remote Sensing*, *48*(3), 1548–1553, doi: 10.1109/tgrs.2009.2029342, 2010.

Rodriguez-Alvarez, N., B. Holt, S. Jaruwatanadilok, E. Podest, and K. C. Cavanaugh, An Arctic sea ice multi-step classification based on GNSS-R data from the TDS-1 mission, *Remote Sensing of Environment*, *230*, 111,202, doi: 10.1016/j.rse.2019.05.021, 2019.

Rostosky, P., G. Spreen, S. L. Farrell, T. Frost, G. Heygster, and C. Melsheimer, Snow Depth Retrieval on Arctic Sea Ice From Passive Microwave Radiometers—Improvements and Extensions to Multiyear Ice Using Lower Frequencies, *Journal of Geophysical Research: Oceans*, *123*(10), 7120–7138, doi: 10.1029/2018jc014028, 2018.

Rösel, A., P. Itkin, J. King, D. Divine, C. Wang, M. A. Granskog, T. Krumpen, and S. Gerland, Thin Sea Ice, Thick Snow, and Widespread Negative Freeboard Observed During N-ICE2015 North of Svalbard, *Journal of Geophysical Research: Oceans*, *123*(2), 1156–1176, doi: 10.1002/2017jc012865, 2018.

Ruf, C., M. Unwin, J. Dickinson, R. Rose, D. Rose, M. Vincent, and A. Lyons, CYGNSS: Enabling the Future of Hurricane Prediction [Remote Sensing Satellites], *IEEE Geoscience and Remote Sensing Magazine*, *1*(2), 52–67, doi: 10.1109/mgrs.2013.2260911, 2013.

Ruf, C. S., and R. Balasubramaniam, Development of the CYGNSS Geophysical Model Function for Wind Speed, *IEEE Journal of Selected Topics in Applied Earth Observations and Remote Sensing*, *12*(1), 66–77, doi: 10.1109/jstars.2018.2833075, 2019.

Ruffini, G., F. Soulat, M. Caparrini, O. Germain, and M. Martín-Neira, The Eddy Experiment: Accurate GNSS-R ocean altimetry from low altitude aircraft, *Geophysical Research Letters*, *31*(12), n/a–n/a, doi: 10.1029/2004gl019994, 2004.

Sansiviero, M., M. . Morales Maqueda, G. Fusco, G. Aulicino, D. Flocco, and G. Budillon, Modelling sea ice formation in the Terra Nova Bay polynya, *Journal of Marine Systems*, *166*, 4–25, doi: 10.1016/j.jmarsys.2016.06.013, 2017.

Schwerdtfeger, P., The thermal properties of sea ice, *Journal of Glaciology*, *4*(36), 789–807, 1963.

Semmling, A. M., J. Wickert, S. Schön, R. Stosius, M. Markgraf, T. Gerber, M. Ge, and G. Beyerle, A zeppelin experiment to study airborne altimetry using specular Global Navigation Satellite System reflections, *Radio Science*, *48*(4), 427–440, doi: 10.1002/rds.20049, 2013.

Sgubin, G., D. Swingedouw, S. Drijfhout, Y. Mary, and A. Bennabi, Abrupt cooling over the North Atlantic in modern climate models, *Nat Commun*, *8*, doi: 10.1038/ncomms14375, 2017.

Shepherd, A., et al., Trends in Antarctic Ice Sheet Elevation and Mass, *Geophysical Research Letters*, *46*(14), 8174–8183, doi: 10.1029/2019gl082182, 2019.

Simonsen, S. B., and L. S. Sørensen, Implications of changing scattering properties on Greenland ice sheet volume change from Cryosat-2 altimetry, *Remote Sensing of Environment*, *190*, 207–216, doi: 10.1016/j.rse.2016.12.012, 2017.

Slater, T., A. Shepherd, M. McMillan, A. Muir, L. Gilbert, A. E. Hogg, H. Konrad, and T. Parrinello, A new digital elevation model of Antarctica derived from CryoSat-2 altimetry, *The Cryosphere*, *12*(4), 1551–1562, doi: 10.5194/tc-12-1551-2018, 2018.

Smeed, D. A., et al., The North Atlantic Ocean Is in a State of Reduced Overturning, *Geophysical Research Letters*, *45*(3), 1527–1533, doi: 10.1002/2017gl076350, 2018.

Soh, L. K., C. Tsatsoulis, D. Gineris, and C. Bertoia, ARKTOS: An Intelligent System for SAR Sea Ice Image Classification, *IEEE Transactions on Geoscience and Remote Sensing*, *42*(1), 229–248, 2004.

SSTL, MERRByS Product Manual - GNSS Reflectometry on TDS-1 with the SGR-ReSI v3, 2017.

Stroeve, J., et al., Surface-based Ku- and Ka-band polarimetric radar for sea ice studies, *The Cryosphere*, *14*(12), 4405–4426, doi: 10.5194/tc-14-4405-2020, 2020.

Stroeve, J. C., M. C. Serreze, M. M. Holland, J. E. Kay, J. Malanik, and A. P. Barrett, The Arctic's rapidly shrinking sea ice cover: a research synthesis, *Climatic Change*, *110*(3-4), 1005–1027, doi: 10.1007/s10584-011-0101-1, 2011.

Studinger, M., IceBridge ATM L1B Elevation and Return Strength, 2 ed., NASA National Snow and Ice Data Center Distributed Active Archive Center, Boulder, Colorado USA, doi: 10.5067/19SIM5TXKPGT, 2013.

Timco, G. W., and R. M. W. Frederking, A review of sea ice density, *Cold Regions Science and Technology*, *24*(1), 1–6, 1996.

Toudal Pedersen, L., et al., ESA Sea Ice Climate Change Initiative (Sea_Ice_CCI): Sea Ice Concentration Climate Data Record from the AMSR-E and AMSR-2 instruments at 25km grid spacing, version 2.1 , serial 05 October 2017, Centre for Environmental Data Analysis, doi: 10.5285/f17f146a31b14dfd960cde0874236ee5, 2017.

Voronovich, A. G., and V. U. Zavorotny, Bistatic Radar Equation for Signals of Opportunity Revisited, *IEEE Transactions on Geoscience and Remote Sensing*, *56*(4), 1959–1968, doi: 10.1109/tgrs.2017.2771253, 2018.

Wingham, D. J., C. G. Rapley, and H. Griffiths, New techniques in satellite altimeter tracking systems, in *IGARSS*, vol. 86, pp. 1339–1344, doi: 10.1007/978-3-642-74585-0_18.

WMO, WMO Sea Ice Nomenclature, 1970.

Yan, Q., and W. Huang, Spaceborne GNSS-R Sea Ice Detection Using Delay-Doppler Maps: First Results From the U.K. TechDemoSat-1 Mission, *IEEE Journal of Selected Topics in Applied Earth Observations and Remote Sensing*, *9*(10), 4795–4801, doi: 10.1109/jstars.2016.2582690, 2016.

Yan, Q., W. Huang, and C. Moloney, Neural Networks Based Sea Ice Detection and Concentration Retrieval From GNSS-R Delay-Doppler Maps, *IEEE Journal of Selected Topics in Applied Earth Observations and Remote Sensing*, *10*(8), 3789–3798, doi: 10.1109/jstars.2017.2689009, 2017.

Zavorotny, V. U., and A. G. Voronovich, Scattering of GPS signals from the ocean with wind remote sensing application, *IEEE Transactions on Geoscience and Remote Sensing*, *38*(2), 951–964, doi: 10.1109/36.841977, 2000.

Zhu, Y., K. Yu, J. Zou, and J. Wickert, Sea Ice Detection Based on Differential Delay-Doppler Maps from UK TechDemoSat-1, *Sensors (Basel)*, *17*(7), doi: 10.3390/s17071614, 2017.

Zirizzotti, A., L. Cafarella, S. Urbini, J. A. Baskaradas, and A. Settimi, Assessment of Electromagnetic Absorption of Ice From Ice Core Measurements, *IEEE Transactions on Geoscience and Remote Sensing*, *54*(8), 4758–4763, 2016.